Università degli Studi di Napoli Federico II
Facoltà di Ingegneria

Juan Carlos Rojas Vidovic

LOADING RATE EFFECT ON THE MECHANICAL BEHAVIOUR OF A PYROCLASTIC SOIL

Tesi di Dottorato
XXI ciclo

Il Coordinatore
Prof. Ing. Federico M. MAZZOLANI

Dottorato di Ricerca in Ingegneria delle Costruzioni

CONTENT

Chapter 1
INTRODUCTION

1.1 GENERAL OVERVIEW AND PROBLEM STATEMENT

The number of publications in the leading journals qualifies the unsaturated soil mechanics as one of the most prolific areas in the geotechnical engineering. In spite of the success reached in the scientific field, the unsaturated soil mechanics have not found an equal success in the engineering application. This fact might be attributed to several difficulties; one of them is the very time-consuming characteristic of unsaturated soil laboratory tests. The long time required to obtain geomechanic parameters rends the unsaturated soil mechanics impractical and uneconomical in engineering practice.

The length of the drainage path strongly influences the testing time. Suction controlled triaxial tests is the most wide spread method used in stress-strain characterization. One of the techniques used to apply such a method is the axis translation, where pore-air pressure (u_a) and pore-water pressure (u_w) are applied and controlled by the sample ends. Generally, the pore-water and pore-air pressures are applied by the bottom and top of the soil specimen, respectively. Under this configuration, the drainage path is equal to the height of specimen. As in saturated soil mechanics, the shorter is the drainage path the shorter is the time required to equalize externally applied net stresses and suction to the values acting on the soil skeleton. Recently, suction controlled triaxial apparatuses with simultaneous application of pore-water and pore-air pressures at both ends of the specimen have been developed. Operating by such a new suction control scheme, a double drainage

system is generated, reducing the drainage path by means air and water drainage from both top and bottom ends.

The rate of loading is another factor that quite significantly influences the testing time. On unsaturated soil testing, the continuous loading procedures are the most common loading methods used to generate stress-strain paths. The constant rate of loading (CRL) and constant rate of strain (CRS) are continuous loading systems at constant velocities. The first one is mainly used on compression tests and the second one on shearing phase.

In the CRL consolidation tests, the soil sample is loaded continuously at whatever rate required to produce the desired constant rate of stress. On such a test, is expected that the loading rate of applied net mean stress has a pronounced effect on the void ratio and degree of saturation on unsaturated soils subjected to constant matric suction, however, no experimental evidence has been published. To prevent any effect of the loading rate, generally, low enough loading rates are selected in order to avoid pore-water increments that could cause suction reduction and consequently loss of specimen rigidity. Conversely, reduced loading rates causes that loading phase continues for a long time. As the creep phenomenon arises not only after the dissipation of pore-water pressure but also during the loading stage, additional strain could be observed in the stage of loading phase due to creep, making the estimation of compression parameters difficult. Then, the loading rate should be small enough to prevent any excess pore-water pressure from developing, but fast enough to prevent excessive creep form occurring at any single stress level. It is surprising, however, that such basic assumptions as above have rarely been examined by a systematic experimental study on unsaturated soils.

More information is available, but not enough, regarding CRS shearing tests on unsaturated soils. The few publications that cover this topic, state that inappropriate strain rates has a pronounced effect on matric suction and may cause loss of suction effects on the soil structure and deviation of the observed behaviour for that expected in constant suction conditions.

In recent years, some published research deals with monitor pore-water pressure during unsaturated soil testing. As monitoring of pore-water changes has been helpful for classical soil mechanics to establish proper loading rates, also can be used for unsaturated soils. A limitation in suction controlled tests is the presence of the air phase, restraining the measurement of pore-water pressure to airtight probes. The high capacity tensiometers are airtight-probes capable of measure pore-water pressure in the positive and negative range; unfortunately, these devices are not commercially available. Then, a research program aimed to monitor pore-water pressure should include also the design and construction of a high capacity tensiometer. As mentioned before, during suction controlled tests where axis

translation technique is used, the pore-air and pore-water pressures are applied by the specimen ends, consequently the tensiometers just can be positioned inside or onto side of soil specimens; under this configuration the pore-water pressure monitoring could be consider as an invasive technique.

Summarizing, in unsaturated soils theory the issue of loading velocity is not taken into consideration. Then, no reliable and practical recommendations are encountered with regard to the selection of loading velocity. The optimum method of determination of proper loading velocity remained an open question due to missing experimental data. Is clear the necessity of systematic experimental studies to increase the knowledge on the effect of loading rate on the mechanical behaviour of unsaturated soils.

To fulfil this requirement, a research program was undertaken at University of Napoli Federico II, Italy, aimed at the experimental analysis of loading rate effect on the mechanical behaviour of a pyroclastic soil.

1.2 RESEARCH OBJETIVES

The objectives of the present research work are twofold:

- to investigate the effect of rate of loading on the behaviour of an unsaturated pyroclastic soil.
- to develop new equipment in order to reduce testing time and conduct suction controlled tests with pore-water pressure measurement.

Specific objectives of this research are as follows:

- modify a triaxial testing apparatus to provide new capabilities of controlling pore-water and pore-air pressure by both the ends.
- develop a suction probe to be used with the modified triaxial apparatus.
- perform isotropic compression and deviator stage at different stress-rate and strain-rate, respectively, using the triaxial apparatus with new capabilities.
- perform suction controlled compression tests with pore-water pressure measurement using the modified triaxial apparatus in combination with the developed suction prove and applying different rate of loading.

1.3 ORGANIZATION OF THE DISSERTATION

A brief description of the chapters included in this dissertation follows.

Chapter 2 presents the review of the published literature regarding the fundamental aspects of unsaturated soil mechanics. This includes a comprehensive framework for the understanding of the behaviour of unsaturated soils in general and pyroclastic soils in particular. In addition, a brief description of the elasto-plastic critical state-based constitutive model for unsaturated soils proposed by Alonso et al. (1990) is presented.

Chapter 3 illustrates the time and rate dependent phenomena and techniques addressed to evaluate its effect on soil behaviour. It focuses on the constant rate of loading (CRL) method; considering loading at constant strain and stress during isotropic compression and deviatoric compression, respectively. This chapter also reviews the state of the art on pore-water measurement on suction controlled triaxial tests. In addition, experimental techniques to determine the rate of loading are reviewed in this chapter.

Chapter 4 is devoted to describing the main features of the suction controlled triaxial testing device USPv2, developed in this study with the objective of testing time reduction. Description of the computer control of the equipment, computer controlled data acquisition, triaxial cells, system to measure the water and volume changes, and system to apply pore-water and pore-air pressure is presented. The calibration of each measuring device is also included in this chapter. In addition, the results of deviatoric compression tests addressed to evaluate the performance of the USPv2 apparatuses are presented.

Chapter 5 introduces two high capacity tensiometers developed to be used for the experimental programme of this thesis. The designs addressed to suit the requirements of the investigation are explained. A device designed to initial saturation of the tensiometers is presented as well as the saturation procedure. This chapter also gives the results and discussion of tests conducted in order to evaluate the performance of the suction probes.

Chapter 6 presents the material used, the compaction method and the experimental program. The characterization of the material was carried out by particle size distribution and index tests. The selection of the compaction method, with the aim of producing uniform and reproducible samples, is explained. Furthermore, this chapter includes the experimental program, which is comprised of the following tests: suction controlled isotropic and deviatoric compression test conducted on full height samples (76 mm), and suction controlled isotropic compression tests with pore-water pressure monitoring on half height samples (38 mm).

Chapter 7 shows the results of the testing program, as well as the interpretation and discussion of the observed behaviour in the context of rate of loading effect.

Chapter 8 presents the conclusions of the research and recommendations for future research.

Chapter 2

FUNDAMENTALS OF UNSATURATED SOIL MECHANICS

2.1 INTRODUCTION

Classical soil mechanics studies the behaviour of soil in a saturated or dry state; that means, the interparticle space totally filled with water or air, respectively. Then, this branch of geotechnical engineering considers only two phases: solid particles and water (saturated soils) or solid particles and air (dry soils). Nevertheless, in some cases, natural deposits and manmade soil structures are not totally saturated or totally dry. To analyze the mechanical behaviour of three-phase soils, where soil particles, and both water and air are present, an extension of the classical soil mechanics to this more complex system was required. The unsaturated soils mechanics are addressed to identify and describe the principles and concepts of three-phase soils.

The understanding of unsaturated soils is of importance in geotechnical and environmental engineering projects. In structures like embankments, earth dams, waste containment in landfill sites, etc., the soil used as construction material are in unsaturated condition during construction and might remain in that condition during his working life. On the other hand, natural phenomena as landslides triggered by critical rainfall events also involve unsaturated soils.

In comparison with saturated soils, unsaturated soils are more difficult to characterize. And the determination of soil parameters under unsaturated state is also costly and very time consuming.

2.2 SOIL SUCTION

The soil suction has been defined by Edlefsen & Anderson (1943) as the free energy of the water in the soil that can be measured in terms of the partial vapor pressure. The soil suction and partial pressure of the pore water vapor can be written as follow:

$$\psi = -\frac{RT}{\upsilon_{wo}\omega_{\upsilon}}\ln\left(\frac{\overline{u}_{\upsilon}}{\overline{u}_{\upsilon o}}\right) \tag{2.1}$$

where: ψ = soil suction [kPa]; R = universal gas constant (i.e. 8.31432 [J/(mol K)]); T = absolute temperature (i.e. T = (273.16 + t^o) [K]); t^o = temperature [ºC]; υ_{wo} = specific volume of water on the inverse of the density of water (i.e. $1/\rho_w$ [m^3 / kg]); ρ_w = density of water (i.e. 998 [kg/m^3] at 20 ºC); ω_{υ} = molecular mass of water vapor (i.e. 18.016 [kg/kmol]); $\overline{u}_{\upsilon}$ = partial pressure of pore-water vapor pressure [kPa]; and $\overline{u}_{\upsilon o}$ = saturation pressure of water vapor over a flat surface of pure water [kPa)].

Considering that the term $\overline{u}_{\upsilon}/\overline{u}_{\upsilon o}$ corresponds to the relative humidity *RH*, and for a temperature of 20 °C the Equation 2.1 can be written as:

$$\psi = -135022\ln RH \tag{2.2}$$

From Equation 2.2, the soil suction at a relative humidity of 100 % is 0 kPa, for a relative humidity value less than it the presence of suction in a soil sample is considered.

The total soil suction ψ can be divided into two components: the matric suction, s, and the osmotic component, π:

$$\psi = s + \pi \tag{2.3}$$

Matric suction is the negative pore water pressure or capillary stress across the air-water interface and is associated with the capillary phenomenon from the surface tension of water. It varies with changes in the moisture content of the soil. The matric suction is by definition equal to the difference in pressure in the air and the water phases and is obtained from the following equation:

$$s = u_a - u_w \tag{2.4}$$

If the air pressure is equal to the atmospheric pressure Equation 2.4 can be reduced to:

$$s = -u_w \tag{2.5}$$

The osmotic component is related to the dissolved salt content in pore water (pore-water salinity) and increases with pore-water salinity. Osmotic suction of the pore fluid is evaluated as the difference between dissolved salts concentration of the pore water and reservoir water salinity.

2.3 SOIL-WATER RETENTION CURVE

A soil-water retention curve (SWRC) expresses the amount of water retained in a soil. The SWRC describes the relationship between gravimetric water content, w, or volumetric, θ, or degree of saturation, S_r, and soil suction. The SWRC plays a central role in understanding the behaviour of an unsaturated soil acting as a valuable conceptual and interpretative tool by which the engineering behavior of unsaturated soils such as flow, strength, and volume change behaviour can be understood and predicted (Puppala et al. 2006).

The key characteristics of SWRC are the air-entry value (or bubbling pressure) AEV, and the residual water content, w_r, respectively defined as:

- the pressure when air starts to enter the largest pores in the soil.
- the water content where a large suction values change is required to remove additional water from the soil.

According to Vanapalli et al. (1994), in the SWRCs of soils three identifiable stages of de-saturation can be defined:

- boundary effect stage, when almost all the soil pores are filled with water;
- transition stage, when the soil dries reaching suction values higher than the air-entry value;
- residual state, when the liquid phase inside the soil becomes discontinuous.

Numerous empirical models or equations have been proposed to describe the highly nonlinear SWCC (e.g., Gardner 1956, Brooks & Corey 1964, van Genuchten 1980; Fredlund and Xing 1994). Leong and Rahardjo (1997) found the van Genuchten (1980) and the Fredlund and Xing (1994) equations are the most suitable to model the behaviour of a variety of soils.

Opposite to what was believed in the past, independent of the method adopted to represent the water retention capacity of a soil a unique SWRC does not exist. As a matter of fact, the variables controlling the water retention capacity of the soils

generate a family of curves instead of a single characteristic one, depending on the previous suction history, the volumetric state or stress level and history.

The water content at a given suction for a wetting path is less than that for a drying path (i.e. SWRC hysteresis). Alternate stages of drying and wetting form an infinite number of scanning curves inside a main hysteresis loop. The names of the various branches of the SWRCs are well known and are indicated in Figure 2.1. As mentioned, the air-entry value, and the residual water content are parameters characterising the SWCR. The AEV varies for every SWRC, while the θ_r seems to be not influenced by the hydraulic hysteresis (Figure 2.1).

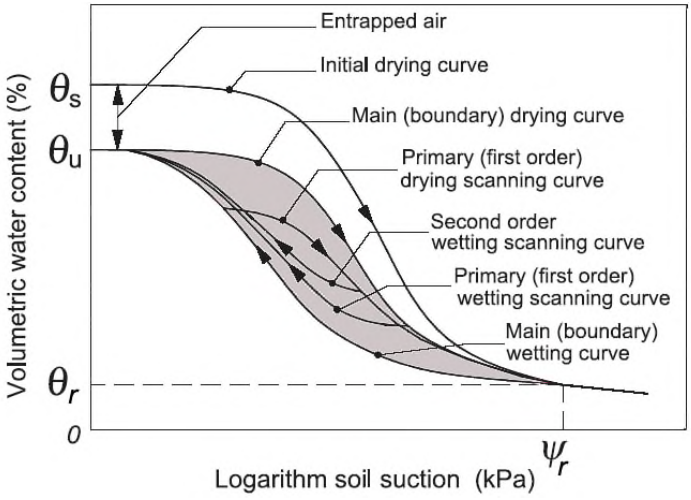

Figure 2.1. Commonly used definitions for hysteretic SWRCs (after Pham et al.2005).

Furthermore, the SWRC is often defined considering only suction as stress state variable and neglecting the effects of volume changes on wetting and drying cycles. Experimental studies, however, have demonstrated that the soil state is also important and needs to be considered in defining its water retention capacity (Ho et al. 2006). Other data (Vanapalli et al. 1999; Romero and Vaunat 2000) also demonstrate that given a single soil type, compaction method may influence its fabric and void ratio, causing significant changes in its water retention properties.

2.4 EFFECTIVE STRESS

The principle of effective stress proposed by Terzaghi and Peck 1958 is intended to describe the mechanical behaviour of saturated soil. The equilibrium equation between total stress, σ, effective stress, σ', and pore-water pressure, u, is:

$$\sigma' = \sigma - u \tag{2.6}$$

For unsaturated soils, the effective stress equation (Bishop 1959) is:

$$\sigma' = \sigma - u_a + \chi(u_a - u_w) \tag{2.7}$$

where χ is a factor depending on the degree of saturation. For dry soil, $\chi = 0$; for saturated soil, $\chi = 1$. The relationship between χ and the degree of saturation is not unique and is influenced by the soil type and the stress paths.

However, is important to note that the terminology of effective stress is quite misleading, provided that a second stress variable is always necessary to fully describe the soil behaviour (Nut and Laloui 2008).

2.5 STRESS INVARIANTS AND MASS-VOLUME PARAMETERS

Matric suction is a scalar quantity but net stress is a tensor quantity, and a total of four stress parameters are therefore required to define fully stress state for a three-dimensional problem: the matric suction and the three principal values of net stress: (σ_1 - u_a), (σ_2 - u_a) and (σ_3 - u_a). For axisymmetric conditions[1] this reduces to three independent stress parameters, which are most conveniently chosen as:

- mean net stress *p*,

$$p = \frac{\sigma_1 + 2\sigma_3}{3} - u_a \tag{2.8}$$

- deviator stress *q*,

$$q = \sigma_1 - \sigma_3 \tag{2.9}$$

- matric suction (Eq. 2.4).

For isotropic conditions the mean net stress is equal to the net confining stress σ_n:

$$\sigma_n = p_{iso} = \frac{\sigma_3 + 2\sigma_3}{3} - u_a = \sigma_3 - u_a \tag{2.10}$$

To define the relative proportions of solids, water and air within an unsaturated element two volumetric state variables are required. Volume change associated with

[1] Under the axisymmetric condition two stresses are equal ($\sigma_2 = \sigma_3$), the triaxial tests are conducted under this condition.

the soil structure and the water phase is denoted using the variables, ε_v and ε_w, respectively.

$$\varepsilon_v = -\frac{\Delta V}{V_0} \tag{2.11}$$

$$\varepsilon_w = -\frac{\Delta V_w}{V_0} \tag{2.12}$$

where ΔV, ΔV_w, and V_0 are the total volume change, water volume change, and initial volume of the specimen, respectively. The variables ε_v and ε_w have been selected to define volume changes for the following reasons (Chen et al. 1999):

- ε_v and ε_w are the direct measures of the volume changes of the overall soil specimen and the water phase, respectively.
- it is convenient to use ε_v and ε_w in continuity equations for coupled problems involving water and air flow as well as the overall change of the soil structure. When the soil is saturated, ε_v is equal to ε_w
- ε_v and ε_w are related to the specific volume v, gravimetric water content w, volumetric water content θ_w, and degree of saturation, S.

Other mass-volume variables are defined based on the volumetric strain, ε_v, and water volumetric strain, ε_w:

- specific volume:

$$v = v_0(1 - \varepsilon_v) \tag{2.13}$$

- gravimetric water content:

$$\theta_w = \theta_{w0} - \varepsilon_w \tag{2.14}$$

- volumetric water content:

$$w = w_0 - \frac{1 + e_0}{G_s}\varepsilon_w \tag{2.15}$$

- degree of saturation:

$$S = \frac{G_s w}{e} = \frac{G_s w_0 - (1 + e_0)\varepsilon_w}{e_0 - (1 + e_0)\varepsilon_v} \tag{2.16}$$

2.6 SHEAR STRENGTH

The shear strength of an unsaturated soil can be formulated in terms of independent stress state variables (Fredlund et al. 1978). The equation is given below:

$$\tau = c' + (\sigma - u_a)\tan\phi' + (u_a - u_w)\tan\phi^b \tag{2.17}$$

where τ = shear strength; c' = effective cohesion; ϕ' = angle of internal friction; and ϕ^b = angle indicating the rate of increase in shear strength relative to the matric suction.

It has been found from earlier studies that ϕ^b appears to be equal to ϕ' at low matric suction, which is less than air-entry value of soil, but decreases to a lower value at high matric suction (Figure 2.2). Experimental results show this nonlinear shear strength behaviour when tests are performed over a wide range of suctions (Escario and Saez 1986; Fredlund et al. 1987; Vanapalli et al. 1996).

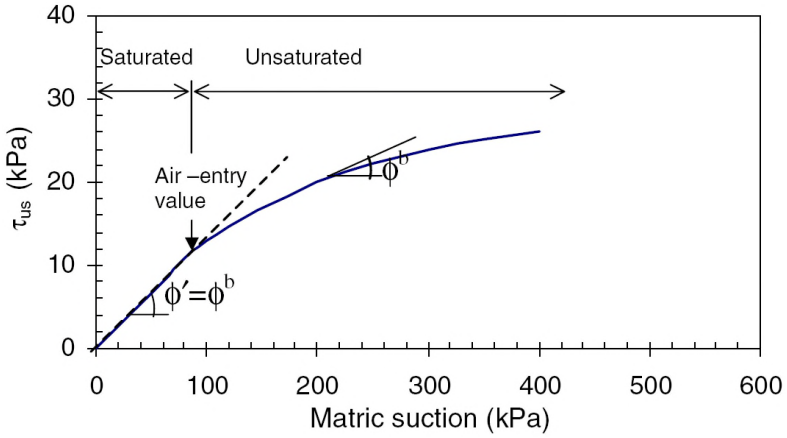

Figure 2.2. Variation of shear strength with respect to matric suction (Tekinsoy et al. 2004).

On the other hand, the apparent cohesion c' shows nonlinearity as a function of matric suction. However, different assumptions for mathematical adjustments exist:

- a constant friction angle ϕ' and the effective cohesion c' varies with suction (Fredlund et al. 1978; Alonso et al. 1990; Machado and Vilar 1998);
- the variation of the two parameters with suction (Wheeler and Sivakumar 1995).

2.7 BARCELONA BASIC MODEL (BBM)

The Barcelona Basic Model (BBM), proposed by Alonso et al. 1990, is one of the most widely used elasto-plastic models for unsaturated soils.

The BBM is a critical state framework involving four state variables: mean net stress, p, deviator stress, q, suction, s and specific volume, *v*. Included in the proposed critical state framework are two formulations: (a) for isotropic stress states and (b) for triaxial stress states.

2.7.2 *Isotropic stress states*

The isotropic state is described in the space "mean net stress - suction". Based on the behaviour of saturated soils, the specific volume is given by:

$$v = N(s) - \lambda(s)\ln\frac{p}{p^c} \tag{2.18}$$

where: $\lambda(s)$ is the stiffness parameter for changes in p for virgin states of the soil; p^c is a reference stress state for which $v = N(s)$.

During an unloading and reloading path, where suction is kept constant, the soil is supposed to behave elastically:

$$dv = -\kappa\frac{dp}{p} \tag{2.19}$$

To ensure the conservativeness of the model in the elastic part, the dependence of κ on s is neglected considering κ as a constant value. A representation of Equations 2.18 and 2.19 is given in Figure 2.3.

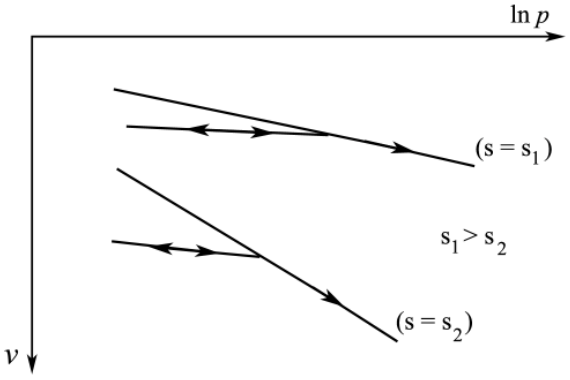

Figure 2.3. Proposed variation of specific volume with net mean stress and suction along virgin and unloading-reloading paths (Alonso et al. 1990).

According to the model, in Figure 2.4 is represented the response to isotropic loading of two samples subjected to different constant suctions (s = 0, s > 0). To saturated soil corresponds the preconsolidation pressure p_0^* (point 3), and for the unsaturated sample the preconsolidation pressure is represented by p_0 (point 1). The relationship between p_0^* and p_0 has been obtained by relating the specific volumes at point 1 and 3, and following the path 1-2-3. The following expression is obtained:

$$v_1 + \Delta v_p + \Delta v_s = v_3 \tag{2.20}$$

The wetting path in the elastic domain, from point 2 to 3 in Figure 2.4, produces a reversible swelling which is given by the following expression:

$$dv = -\kappa_s \frac{ds}{(s + p_{at})} \tag{2.21}$$

where: κ_s is the elastic stiffness parameter for changes in suction; and p_{at} is the atmospheric pressure. The p_{at} has been added to suction to avoid infinite values as suction approaches zero.

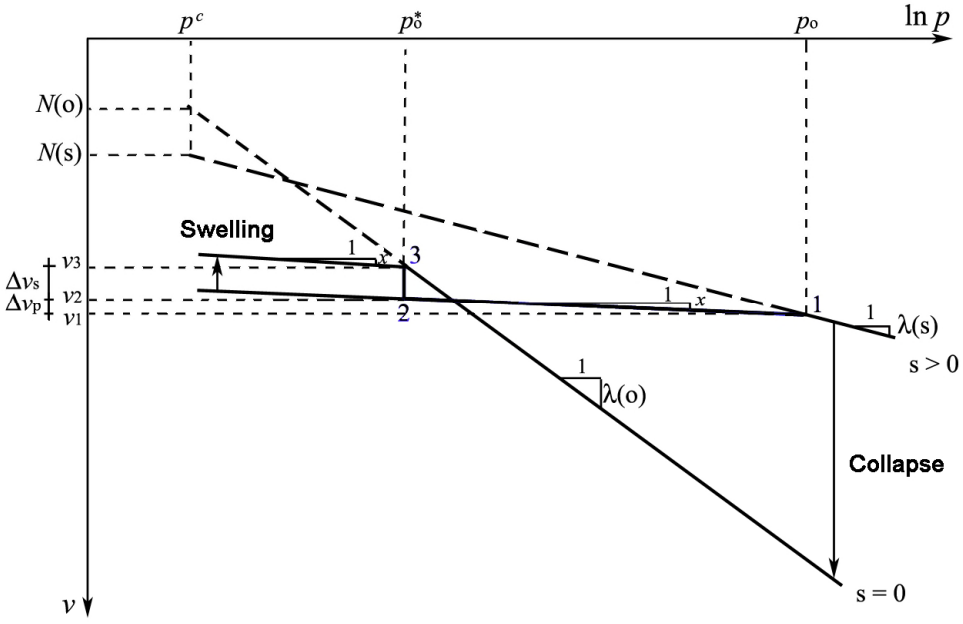

Figure 2.4. Relationship between preconsolidation stresses p_0 and p_0^*; compression curves for saturated and unsaturated soil (Alonso et al. 1990).

From Equations 2.17 to 2.20 has been obtained a relationship between p_0 and suction as a function of the reference stress values: p_0^* and p_{at} and the soil parameters: N(s), λ(s), κ, κ_s :

$$N(s)-\lambda(s)\ln\frac{p_o}{p^c}+\kappa\ln\frac{p_o}{p_o^*}+\kappa_s\ln\frac{s+p_{at}}{p_{at}}=N(0)-\lambda(0)\ln\frac{p_o^*}{p^c} \tag{2.22}$$

N(0) y λ(0) are the values N(s) y λ(s) for a saturated condition. Considering that p^c is the net mean stress at which the saturated virgin state is reached, starting from a partially saturated condition and following elastic swelling, is possible to represent Equation 2.21 as follows:

$$\Delta v\left(p^c\right)\Big|_s^0=N(0)-N(s)=\kappa_s\ln\frac{s+p_{at}}{p_{at}} \tag{2.23}$$

Introducing Equation 2.22 into Equation 2.21, the following relationship has been obtained:

$$\left(\frac{p_0}{p}\right)=\left(\frac{p_0^*}{p^c}\right)^{[\lambda(0)-\kappa]/[\lambda(s)-\kappa]} \tag{2.24}$$

Equation 2.23 represents in a (p, s) space a yielding surface (Figure 2.5) constituted of a family of yield curves, which position is determined by the preconsolidation net mean stress for saturated conditions, p_0^*. The parameter p_0^* acts as a hardening term in Equation 2.23. The yield curves that represent this equation is named the loading-collapse (LC) yield curve, because explains the apparent increase in preconsolidation stress associated with increasing suction, and also the collapse phenomena observed during wetting paths. Figure 2.5 sketched a LC yield curve through points 1 and 3.

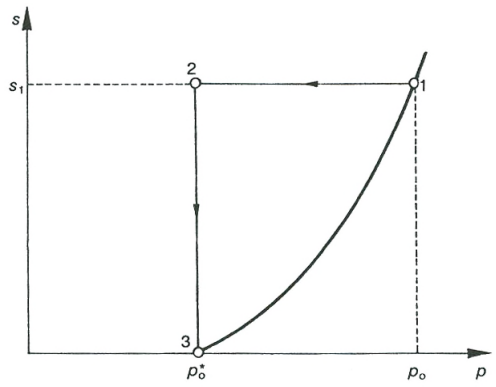

Figure 2.5. Stress path and yield curve in (p, s) stress plane (Alonso et al. 1990).

Equation 2.24 predicts the increase in soil stiffness with suction:

$$\lambda(s) = \lambda(0)\left[(1-r)\exp(-\beta s) + r\right] \tag{2.25}$$

where: r is a constant related to the maximum stiffness of the soil (for an infinite suction); and β is a parameter which controls the rate of increase of soil stiffness with suction.

The authors adopted a value s_0 as the maximum past suction ever experienced by the soil. This value bounds the transition from the elastic to the virgin range when suction is increased (Figure 2.6). This yield locus, represented in the (p, s) plane (Figure 2.7), is named SI (after suction increase). Alonso et al. (1990) propose that LC and Si yield loci enclose the elastic region.

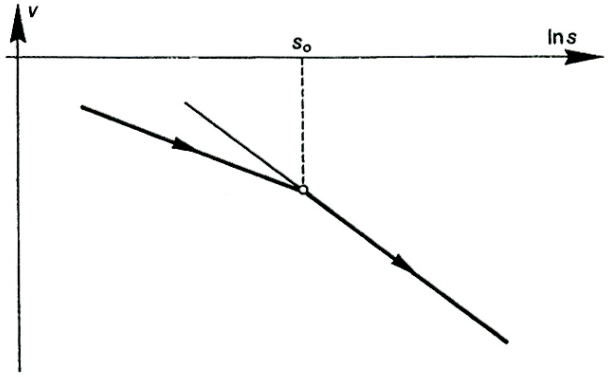

Figure 2.6. Definition of yield suction s_0 (Alonso et al. 1990).

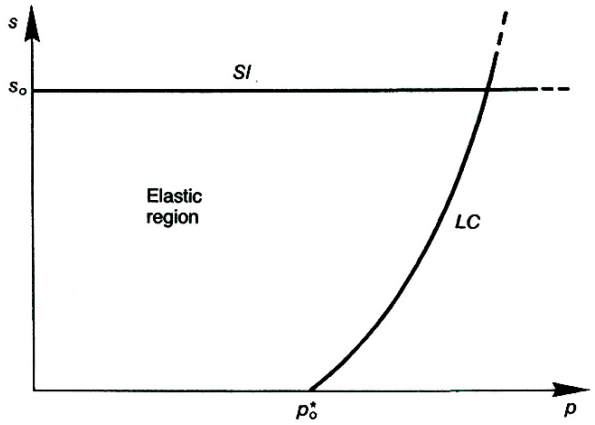

Figure 2.7. Loading-collapse (LC) and suction increase (SI) yield curves (Alonso et al. 1990).

A linear dependence has been adopted between v and ln(s+pat), then, for virgin states results the following equation:

$$dv = -\lambda_s \frac{ds}{(s + p_{at})} \tag{2.26}$$

and for drying and wetting reversals the Equation 2.20 should be considered.

2.7.1.1 Hardening laws

An increase of p in the elastic region will induce a compressive volumetric deformation given by:

$$d\varepsilon_{vp}^{e} = -\frac{dv}{v} = \frac{\kappa}{v}\frac{dp}{p} \tag{2.27}$$

After p reaches the yield value p_0 the volumetric deformation may be determined by:

$$d\varepsilon_{vp} = \frac{\lambda(s)}{v}\frac{dp_0}{p} \tag{2.28}$$

The plastic component of volumetric strain is given by:

$$d\varepsilon_{vp} = \frac{\lambda(s) - \kappa}{v}\frac{dp_0}{p} \tag{2.29}$$

On the other hand, an increase in suction within the elastic may be computed from:

$$d\varepsilon_{vs}^{e} = \frac{\kappa_s}{v}\frac{ds}{(s + p_{at})} \tag{2.30}$$

Once the yield locus s = s_0 is reached, the total and plastic deformations will be given by:

$$d\varepsilon_{vs} = \frac{\lambda_s}{v}\frac{ds_0}{(s_0 + p_{at})} \tag{2.31}$$

$$d\varepsilon_{vs}^{p} = \frac{\lambda_s - \kappa_s}{v}\frac{ds_0}{(s_0 + p_{at})} \tag{2.32}$$

A simple way to couple both yield curves is also proposed by the Authors, this occurs if their position is controlled by the total plastic volumetric deformation, $d\varepsilon_v^p = d\varepsilon_{vs}^p + d\varepsilon_p^p$. Then, the hardening laws are as follows:

$$\frac{dp_0^*}{p_0^*} = \frac{v}{\lambda(0) - \kappa} d\varepsilon_v^p \tag{2.33}$$

$$\frac{ds_0}{s_0 + p_{at}} = \frac{v}{\lambda_s - \kappa_s} d\varepsilon_v^p \tag{2.34}$$

2.7.2 *Triaxial stress states*

A third parameter has been included (i.e. deviatoric stress q) to include the effect of shear stresses. In the model, the volumetric strain is defined by:

$$\varepsilon_v = \varepsilon_1 + 2\varepsilon_3 \tag{2.35}$$

And the shear strain is given by:

$$\varepsilon_s = \frac{2}{3}(\varepsilon_1 - \varepsilon_3) \tag{2.36}$$

The proposed yield curve for a sample at constant suction is described by an ellipse which exhibits an isotropic preconsolidation stress given by p_0 value which lies on the LC yield curve (Figure 2.8).

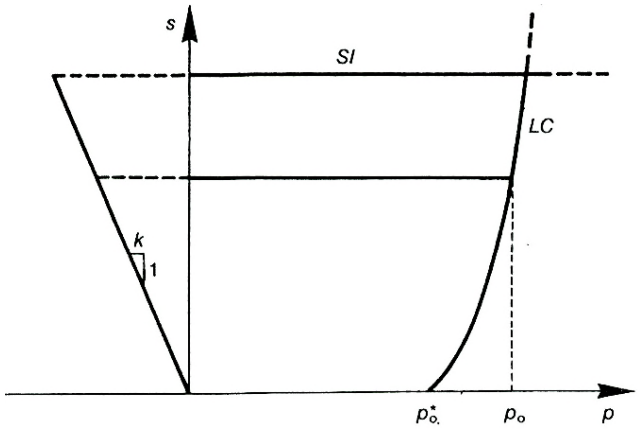

Figure 2.8. Yield surfaces in (p,s) plane (Alonso et al. 1990).

The model considers a critical state line (CSL) for non-zero suction to represent the increased strength induced by suction (Figure 2.9). This line is parallel to the saturated condition. The effect of suction is represented by an increase in cohesion, maintaining the slope M of the CSL for saturated line. However the Authors note that

this may be a suitable approach for a limited range of stress changes, and that other choices are possible.

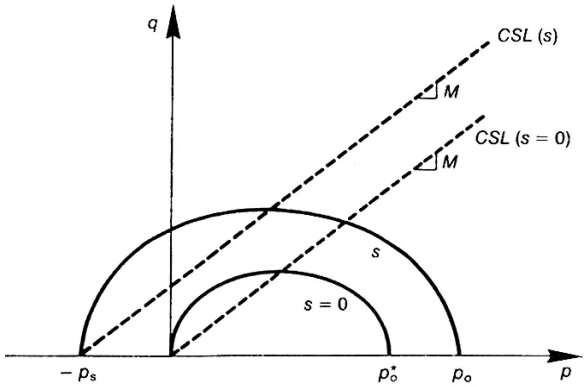

Figure 2.9. Yield surfaces in (p,q) plane (Alonso et al. 1990).

Considering that the cohesion follows a linear relationship with suction, the ellipse intersects the p axis at a point for which:

$$p = -p_s = -ks \tag{2.37}$$

where: k is a constant. The major axis of the ellipse span the segment $-p_s(s)$ to $p_0(s)$ and this equation is given by:

$$q^2 - M^2(p + p_s)(p_0 - p) = 0 \tag{2.38}$$

Figure 2.10 shows a three-dimensional view of the yield surfaces in the (p,q,s) space.

The expression for the associated flow rule is the following equation:

$$\frac{d\varepsilon_s^p}{d\varepsilon_{vp}^p} = \frac{2q\alpha}{M^2(2p + p_s - p_0)} \tag{2.39}$$

where: α is chosen in such a way that the flow rule predicts zero lateral strain for stress states corresponding to K_0 values.

The vector of plastic strain increment induced by suction increase is $(d\varepsilon_{vs}^p, 0)$, $d\varepsilon_{vs}^p$ is given by Equation 2.31. The elastic strains, induced by changes in q is determined through a shear modulus G:

$$d\varepsilon_s^e = \left(\frac{1}{3}G\right)dq \tag{2.40}$$

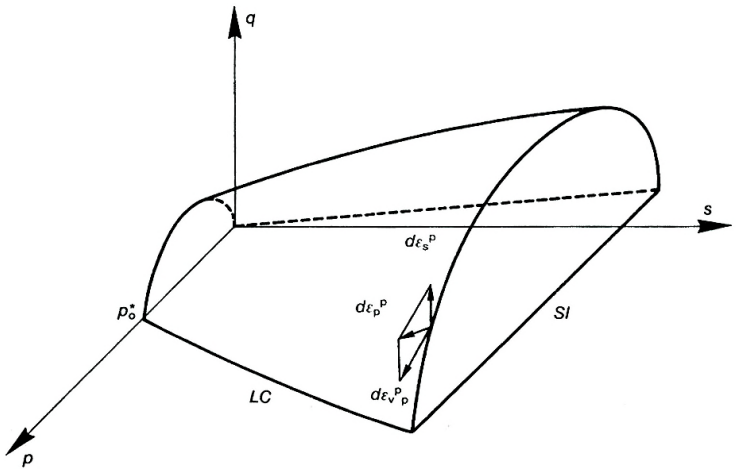

Figure 2.10. Three-dimensional view of the yield surfaces in (p, q, s) stress space. (Alonso et al. 1990).

Chapter 3

LOADING RATE EFFECT: LITERARURE REVIEW

3.1 CONTINUOS LOADING CONSOLIDATION TESTS

Generally, tests of consolidation under constant load are determined as the incremental loading (IL) system. This kind of tests, used for the past 70 years to estimate soil settlement characteristics, is also called standard-incremental-loading (STD) consolidation tests. In the IL consolidation test, vertical loading is applied by steps, and this is constant in every applied step and it does not offer the possibility of keeping recorded the pore water pressures.

As an alternative to the IL consolidation tests several other test methods have been developed, among them the continuous loading (CL) consolidation test. Three are the subcategories of CL consolidation tests:

1) tests at constant velocities: constant rate of loading CRL (Aboshi et al. 1971) and constant rate of strain CRS (Smith et al. 1971).
2) tests at constant gradient of pore water pressure in the undrained base of the specimen: controlled gradient (CG) (Lowe et al. 1969).
3) tests at constant rate of loading/pore-water pressure ratio in the undrained base of the specimen (Janbu et al. 1979).

The characteristic paths of CL test are illustrated in Figure 3.1. The common element in all these tests is that the vertical loading applied on the samples is a continuous one and variable with the time, in addition of the possibility to keep recording the pore water pressure generated in the undrained base of the specimen during all the testing time (Muñoz 2004).

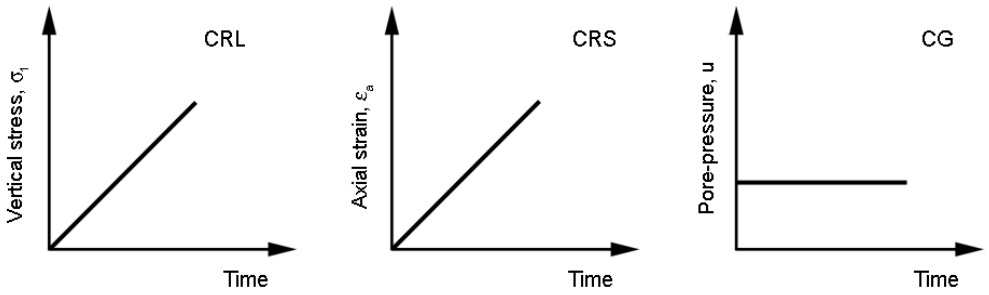

Figure 3.1. Paths of continuous loading consolidation test.

Von Fay and Cotton (1986) compared results obtained with the CRL method with results from the IL method. The results show that test completion times for the CRL test are much shorter than for the IL test, that agreement between the results of the CRL and IL tests are within reasonable limits, and that the CRL method offer an alternative to the IL test.

3.1.1 *Loading velocity*

Several different criteria have been proposed to determine the rate of loading in CL consolidation tests. All this methods are addressed to found a loading velocity slower enough to not exceed recommended values of the following ratio:

$$u_m/\sigma \tag{3.1}$$

where: u_m = pore-water pressure measured at the impermeable specimen base; and σ = total stress applied to specimen at a given moment.

Table 3.1 present a summary of the recommended values for the ratio u_m/σ. It shows significant variations between suggested values. For values of the ratio u_m/σ less than 0.1 effects related to rheological processes of secondary consolidation are visible (Almeida et al. 1995).

Table 3.1. Recommended u_m/σ values for exampled soil in CL tests (Dobak 2003).

Recommended u_m/σ values	Soil type	Reference
0.5	kaolinites, Ca-monmorillonites, Massena clay	Smith and Wahls (1969)
0.05	boston blue clay (artificially sedimented)	Wissa et al. (1971)
0.1 – 0.15	Bakebol clay	Sällfors (1975)
0.3 – 0.5	silts and clays from the Coalfield of Mississippi Plains (Kentucky)	Gorman et al. (1978)

3.1.2 *Dobak's theoretical model for loading velocity in CL consolidation*

Dobak (1999) introduces an adaptation of the classical solution of consolidation to conditions of constantly increasing load allowed for development of a model of pore pressure dissipation in CL tests.

Dobak's model introduces the following parameters:

$$t_{(T=1)} = \frac{H^2}{c_v} = \frac{H^2 \times \gamma_w}{k \times M} \tag{3.2}$$

where: $t_{(T=1)}$ = specific consolidation time; H = current thickness of specimen equal to length of drainage in uniaxial consolidation; c_v = coefficient of consolidation; γ_w = unit weight of water; k = coefficient of permeability; M = modulus of one-dimensional compressibility;

$$t \Big/ t_{(T=1)} \tag{3.3}$$

where: $t/t_{(T=1)}$ = relative consolidation time; t = current time determined from initiation of loading;

$$C_K = \frac{u}{\sigma} \tag{3.4}$$

where: C_K is the parameter of pore-water pressure for conditions of CL test in consolidometer.

Loading programs, applied in IL and CL test, were limited for the needs of theoretical analysis to equation 3.5, and characterized in Table 3.2.

$$\sigma = a \times t^{n} \tag{3.5}$$

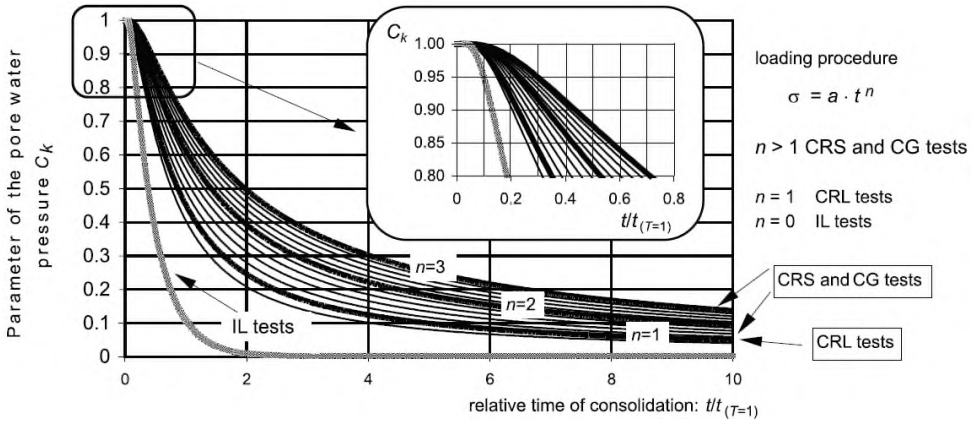

Figure 3.2. Theoretical distribution of water pressure in one-dimensional consolidation tests (Dobak 2003).

The obtained results of theoretical analysis, illustrated by Figure 3.2, indicate the following relationships:

4) dissipation of pore water pressure during CL test depends exclusively upon the character of load increase, expressed by the exponent "n", and not upon a value of loading velocity.

5) a single graph in the coordinate: C_K versus $t/t_{(T=1)}$ corresponds with different constant rate of loading.

Table 3.2. Conditions of one-dimensional consolidation tests (Dobak 2003).

Types of tests		Soil type	Exponential model of stress changes $\sigma = a \times t^n$	Governing physical processes
IL		σ = const	n = 0	- creep of soil skeleton - seepage
CL	CRL	$\Delta\sigma/\Delta t$ = const	n = 1	- character and changes in stress increase - seepage - creep of soil skeleton
	CRS CG	$\Delta\sigma/\Delta t$ increasing	n > 1	

3.1.3 *Rate of loading effect on unsaturated soils*

Cui and Delage et al. (1996) performed isotropic compression tests on unsaturated soils applying both step loading (IL) and continuous loading (CRL). The tests, which results are presented in Figure 3.3, were conducted on statically compacted samples of aeolian silt. In IL tests (Figure 3.3a), each pressure was maintained for approximately 48 h to ensure stabilization of both water changes and volume changes. In CRL tests (Figure 3.3a) the applied rate was 24 kPa/h. In the IL method the loading is large and sudden inducing drastic instantaneous (undrained) decrease of the volume. The authors consider that the undrained loading produces excess pore-water pressure within the sample, so that the suction of the soil is no longer regulated by the suction control system. A better regulation is ensured when CRL method is used, and the generated data corresponds better to the imposed suction.

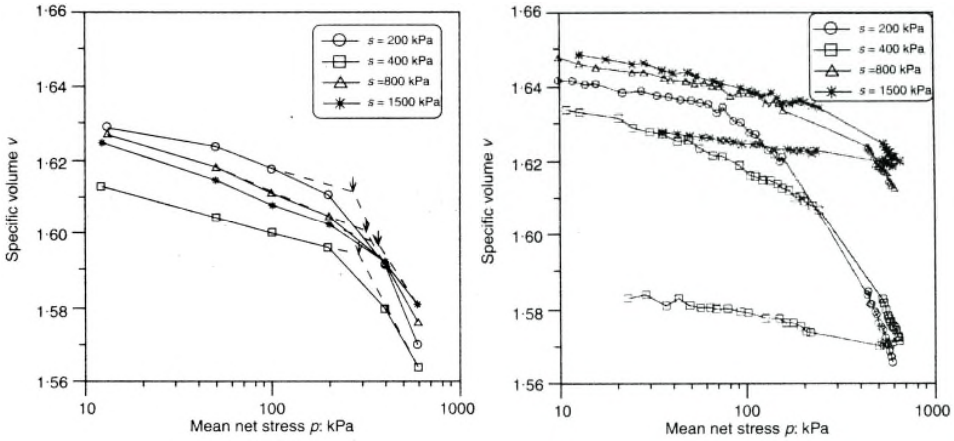

Figure 3.3. Volume changes under (a) isotropic step loading and (b) continuous isotropic loading (Cui and Delage 1996).

Figure 3.4 shows the loading collapse (LC) curve for both IL and CRL tests. A great difference is observed between the shapes of the two curves (i.e. difference between the isotropic yield stresses ($p_{0(s)}$)).

The work presented by Cui and Delage (1996) can be summarized as follows:

1) The IL procedure is not suitable for unsaturated soils, and should not be used for investigating compressibility properties under suction controlled conditions.
2) The IL method overestimates the compressibility and underestimates the yield stress when applied in unsaturated soils.

3) The effect of sudden loading (IL) is smaller when saturation is approached (i.e. low suction values).

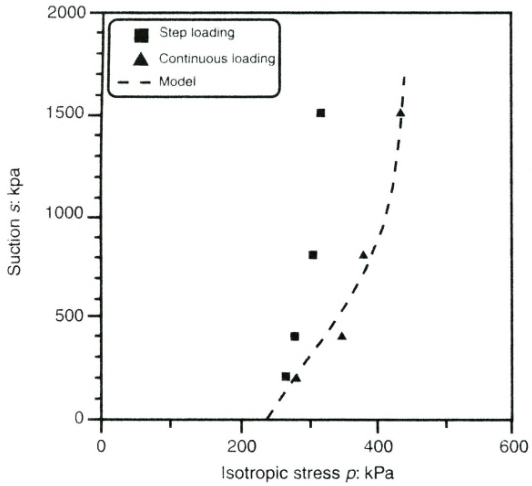

Figure 3.4. Experimental determination of the LC yield curve for IL and CRL tests (Cui and Delage 1996).

Sivakumar (1993) conducted IL consolidation tests aimed to investigate the movement of the yield curves for the top and bottom of a triaxial sample. The tests were carried out under controlled suction using the principle of axis translation. Pore-water pressure was applied and measured at the base of the sample and pore-air pressure was applied at the top of the sample; under this configuration the water just can drained by the bottom. He observed quickly pore-water pressure dissipation at the bottom of the sample; on the contrary, excess pore-water pressure occurs at the top which dissipates slowly during following consolidation stage. At the bottom the soil reaches the final equilibrium on the related yield curve, but at the top of the sample the state of the soil will be in the elastic region. The author suggests increase load at a rate such that the excess pore-water pressure at the top of the sample is kept within acceptable limits.

Recently, Huat et al. (2006) conducted a study addressed to analyze the effect of loading rate of applied net mean stress on the volumes change behaviour of an unsaturated granitic residual soil. Three loading rates were adopted, namely fast, slow and extra slow loading rate:

1) fast loading is the normal loading rate in the standard IL, where the increase is almost immediate (1 – 2 s),

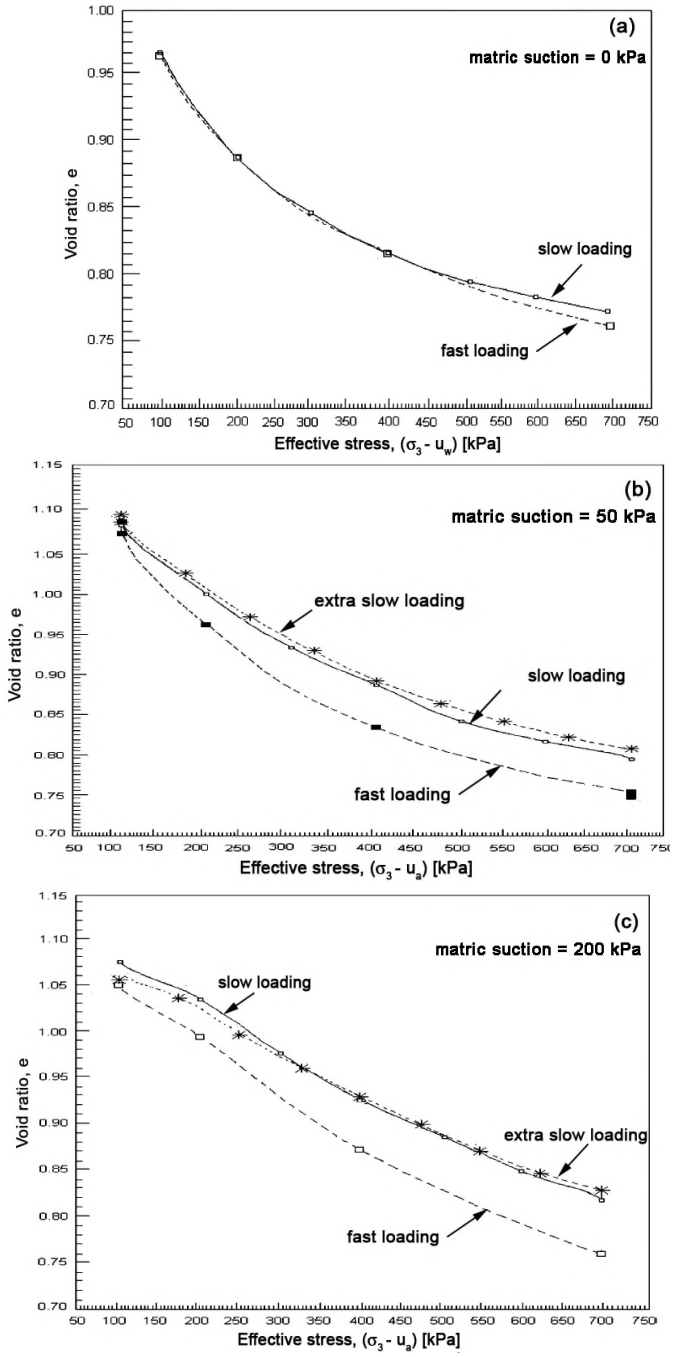

Figure 3.5. Void ratio of samples at various stress points (modified from Huat et al. 2006).

2) slow loading rate, the increment was performed in 10 sub-increments for each stress path (≈ 10 kPa in each sub-increment with an interval time of 30 min),

3) extra slow loading rate, the increments were also performed in 10 sub-increments (≈7.5 kPa in each sub-increment at an interval time of 30 min).

The results obtained by Huat et al. (2006) are shown in Figure 3.5. Based on the observed behaviour, the authors conclude that the loading rate of applied stress has a pronounced effect on the void ratio and degree of saturation but has an insignificant effect on the water content of the soil subjected to constant applied suction. For the saturated case (Figure 3.5a), the loading rate of applied stress appears to have an insignificant effect on the void ratio, water content and degree of saturation.

3.2 TRIAXIAL COMPRESSION TESTS

Loading rate effects during saturated drained triaxial compression tests do not appear to be as significant as in undrained tests (Yamamuro and Lade 1993). Most of the observations in literature have focused on the determination of the time-dependent behavior of clayey soils, whereas the reported experimental studies of granular materials are few (Augustesen et al. 2004). On saturated soils, the time-dependent phenomena are more pronounced in clay than sand.

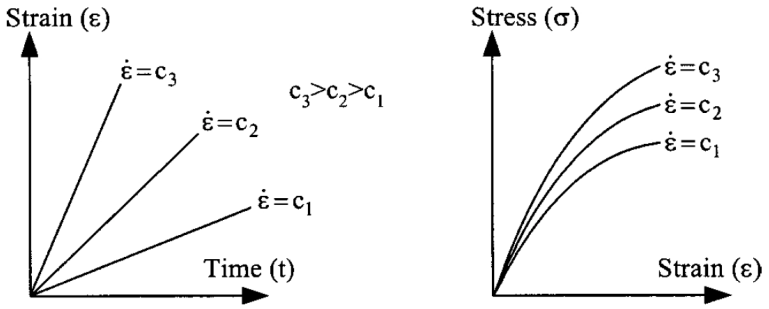

Figure 3.6. Constant rate of strain tests: (a) strain history during a CRS test, the total strain rate $\dot{\varepsilon}$ is kept constant and (b) stress–strain response. c1, c2 and c3 are constants.

In the constant rate of strain test (CRS), a total strain rate $\dot{\varepsilon} = d\varepsilon/dt$ is imposed and kept constant during the test. The stress response is then measured in order to obtain a stress–strain relationship. In Figure 3.6, the results of three CRS tests are shown. It appears that the larger the strain rate, the stiffer the soil. In connection with rate-independent elastoplasticity, the three curves will coincide.

Matsushita et al. (1999) studied the rate dependency on the stress and strain behavior by performing drained plane strain compression tests and triaxial compression tests on sands. The rate dependency was investigated in two loading situations: Tests where the strain rate for each test was kept constant (Figure 3.7), and tests where the strain rate was changed stepwise (Figure 3.8).

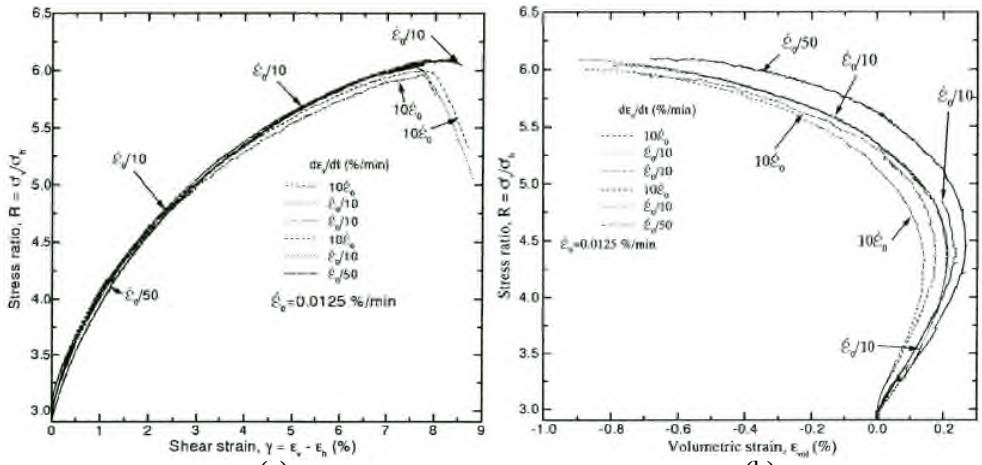

(a) (b)

Figure 3.7. Drained plane strain compression tests at different constant axial strain rates on saturated Houston sand: (a) stress ratio versus shear strain; and (b) stress ratio versus volumetric strain (modified after Matsushita et al. 1999).

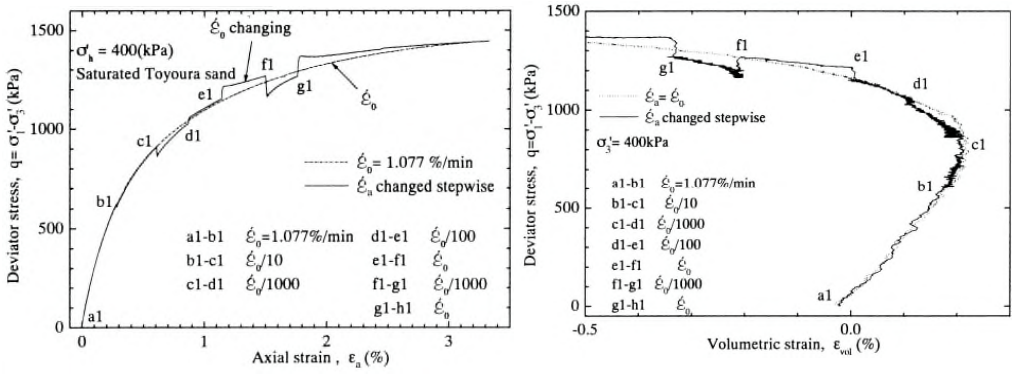

(a) (b)

Figure 3.8. Two drained triaxial compression tests constant axial strain rates with step changes in the constant axial strain rate on saturated Toyoura sand: (a) deviator stress versus axial strain; and (b) deviator stress versus volumetric strain (modified after Matsushita et al. 1999).

In tests where the axial strain rate was kept constant, the stress–strain relationships were essentially independent of the constant strain rates (Figure 3.7), which differed by a factor up to 500. In contrast, when the constant shear strain rate was changed stepwise, the shear stress increased and decreased temporarily (Figure 3.8). The stress–strain relationship temporarily overshoots the unique relationship for the constant rate of strain curve when the strain rate is increased stepwise. After having exhibited clear yielding, the stress–strain relationship gradually rejoins the unique relationship for the constant rate of strain curve. On the other hand, when the strain rate is decreased stepwise, the stress–strain relation undershoots temporarily and eventually rejoins the unique relationship for the constant rate of strain curve.

Figure 3.9 presents the results of three drained triaxial compression tests conducted by Yamamuro and Lade (1993). The soil used was a uniform Cambria Sand. Shearing was performed at three different strain rates varying between a lower value of 0.0517%/min and an upper value of 0.74 %/min. The deviator stresses show small increases with increasing strain rate.

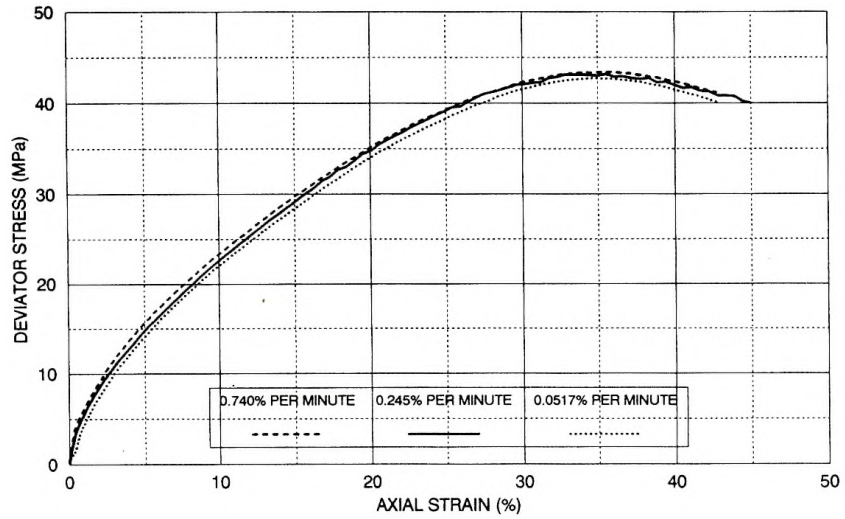

Figure 3.9. Deviator stresses for drained tests sheared at different strain rates on dense Cambria sand (Yamamuro and Lade 1993).

On the other hand, Figure 3.10 shows the measured axial load versus axial strain for the silty clay Sackville soil (Rowe and Hinchberger 1998). The measured undrained shear strength of the Sackville soil was found to be rate dependent during consolidated anisotropic undrained (CAU) triaxial tests.

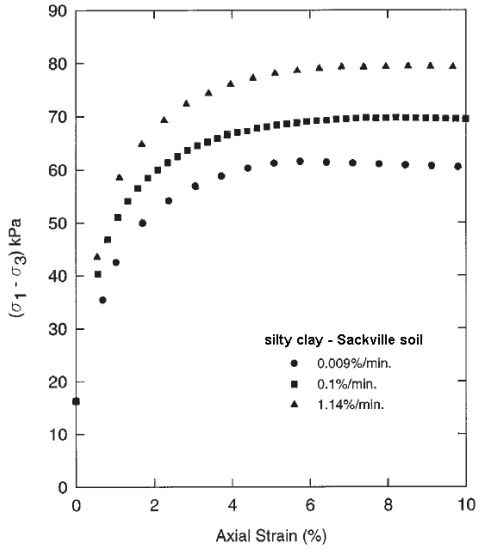

Figure 3.10. Deviator stress versus axial strain response during consolidate anisotropic undrained triaxial shear (Rowe and Hinchberger 1998).

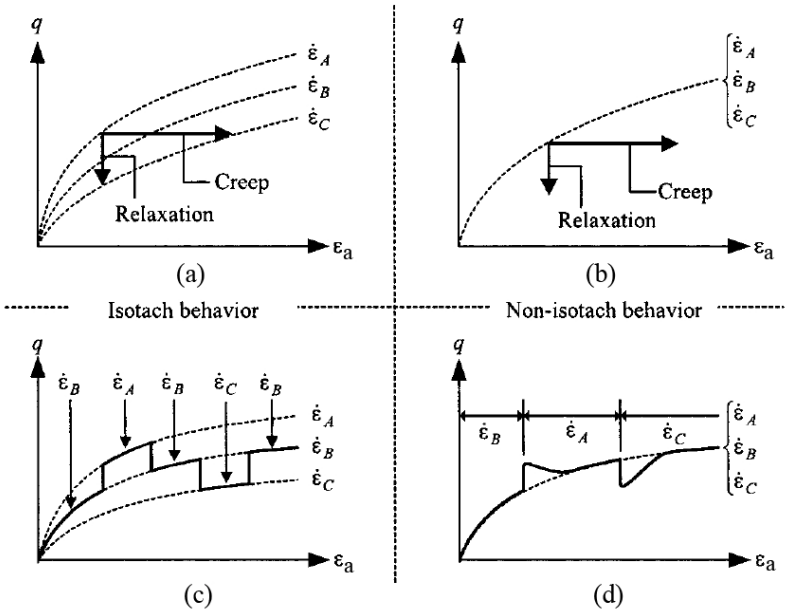

Figure 3.11. Isotach behavior is observed in clay for (a) creep and relaxation and (b) stepwise change in rate. Nonisotach behavior is observed in sand for (c) creep and relaxation and (d) stepwise change in rate (Augustesen et al. 2004).

Augustesen et al. (2004) summarize the loading rate effect on sands and clays in Figure 3.11. The fact that the phenomena of creep, relaxation, and strain-rate effects are governed by the same basic time mechanism is denoted isotach behaviour, (i.e., there is a unique stress–strain–strain rate relation for a given soil). The isotach behaviour corresponds to some extent to the observed behaviour of clay. The sand tested by Matsushita et al. (1999) exhibited noticeable amounts of creep and relaxation but no strain-rate effects. For sand, this behaviour is labelled as nonisotach.

3.2.1 *Unsaturated conditions*

To select the loading rate that would avoid menisci disruption (i.e. suction variation) for a silty soil, Porras (2004) conducted five triaxial compression tests, each at different load rate. The tests were run at conditions favourable for menisci disturbance, that is, a low confinement and a relatively high suction. An effective confinement of 25 kPa and the highest suction value used in this study (50 kPa) were selected. Each specimen was loaded incrementally up to 75 kPa of deviatoric stress. The results of these tests are presented in Figure 3.12, where it is observed that slower loading rates cause smaller strains. Loading rates of 3 and 6 kPa/h produce similar strains. Therefore a loading rate of 6 kPa/h was selected to complete the testing.

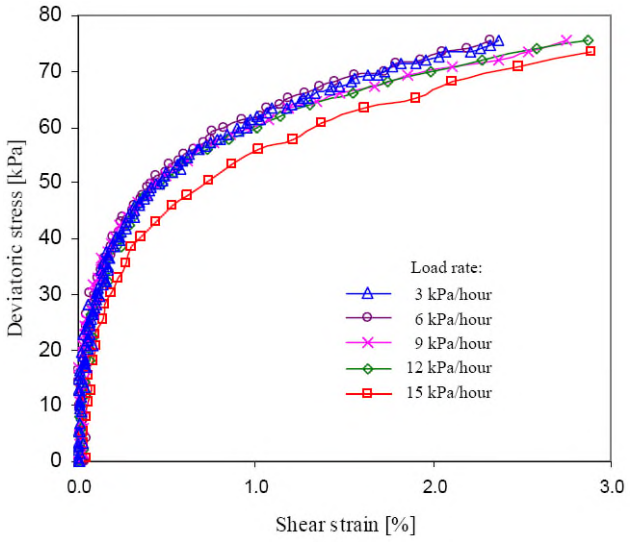

Figure 3.12. Stress-strain response at different loading rates during a triaxial compression stress path on silt specimens with suction of 50 kPa and initial effective confinement of 25 kPa (Porras 2004).

3.3 PORE-WATER PRESSURE MEASUREMENT IN SUCTION CONTROLLED TRIAXIAL TESTS

In recent years, many published research deals with monitor pore-water pressure (u_w) during unsaturated soil testing. It should be added, though, that many contributions used invasive techniques such as the inclusion of miniature suction probes inside (e.g. Gallage and Uchimura 2006) or onto side of soil specimens (e.g. Toll 1998; Meilani et al. 2002). In this section has been presented the apparatuses and results obtained by different authors.

One of the first attempts to measure pore-water pressure during suction controlled tests has been done by Toll (1986). The layout of the used triaxial apparatus is shown schematically in Figure 3.13. To impose suction, pore-air pressure was controlled by an air line connected to the sample through the top cap, and pore-water pressure was controlled at the sample base. The pore-water pressure was measured at the mid height of the sample using a pore-water pressure (P.W.P.) probe installed in the side of the sample (Figure 3.13).

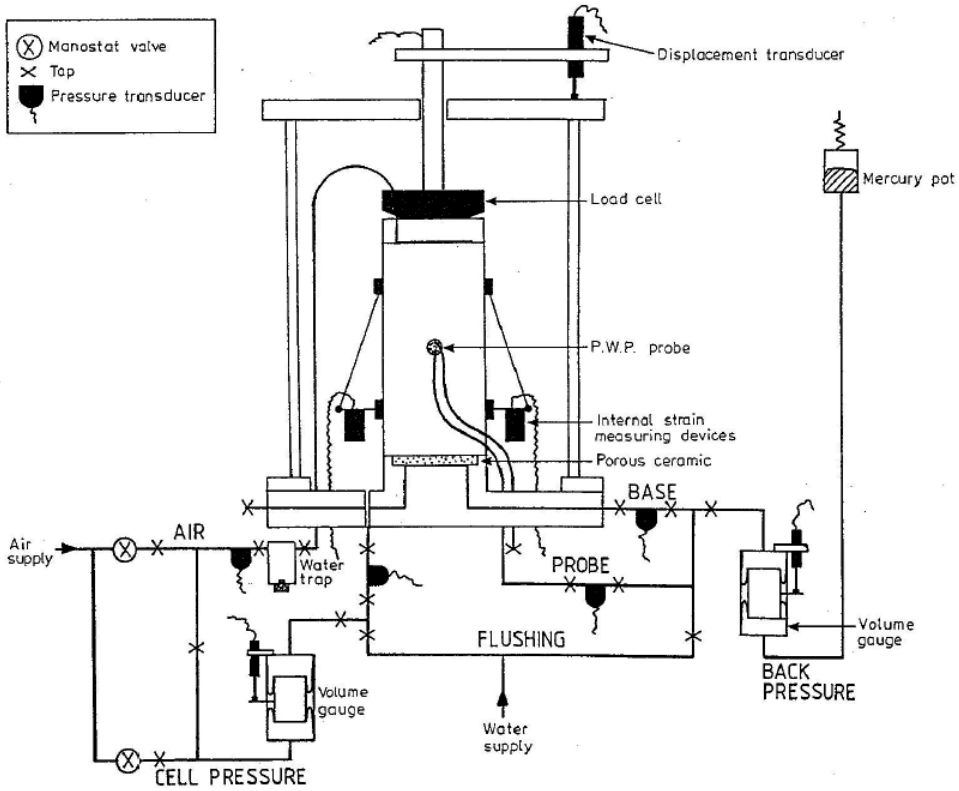

Figure 3.13. Triaxial cell and control system (Toll 1986).

Another attempt was done by Cunningham et al. (2003). A standard stress-path triaxial cell was modified in order to test unsaturated soils. To control suction, the apparatus employs an air-circulation system to remove moisture from the base of the soil sample (Figure 3.14). The suction was independently measured using two suction probes. The probes correspond to the design presented by Ridley (1995), with a capability of directly measuring suction in the range 0 to1500 kPa.

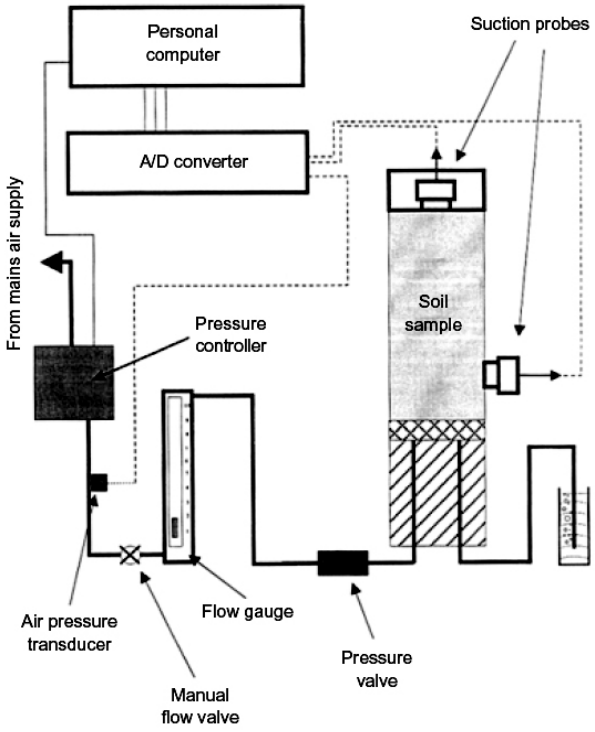

Figure 3.14. Schematic diagram of configuration of air-circulation suction-control system (Cunningham et al. 2003).

Figure 3.15 shows the results of measured pore-water pressure by the top and lower suction probes during the three stages of a triaxial test. Starting from a fully saturated state, the soil sample was dried to a suction of 850 kPa, then loaded isotropically to a confining stress of 400 kPa and finally sheared at constant suction.

To measure pore-water pressure during suction controlled triaxial tests, Meilani et al. (2002) used a modified triaxial apparatus equipped with three mini suction probes along the height of a specimen. The suction probes were placed at 3/4, 1/2, and 1/4 height of the specimen from its base and at 120° apart in the lateral direction (Figure 3.16a). Figure 3.16b shows the installation of a probe onto a soil specimen.

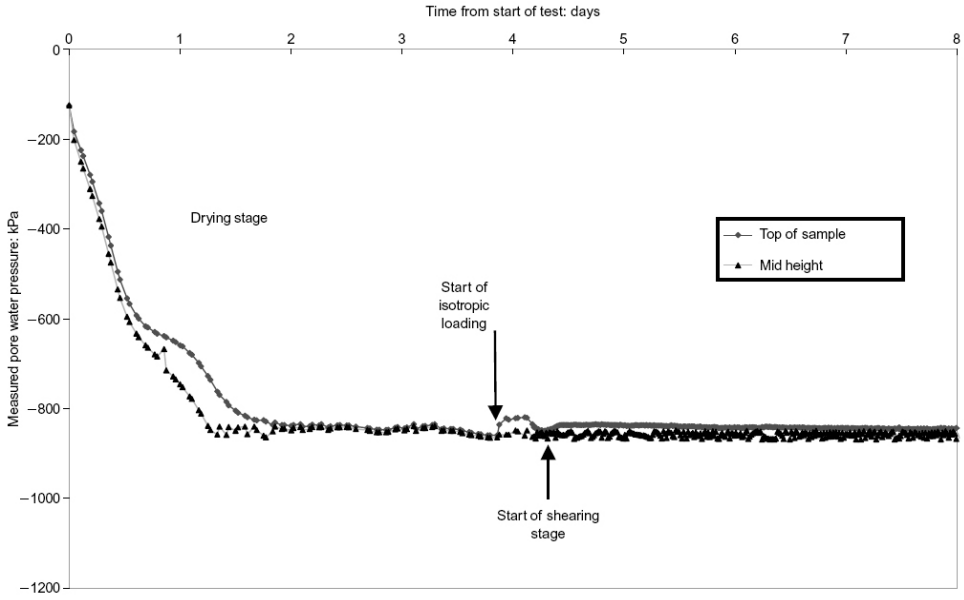

Figure 3.15. Plot of measured pore-water pressure against time for constant-suction shearing test with s=850 kPa (Cunningham et al. 2003)

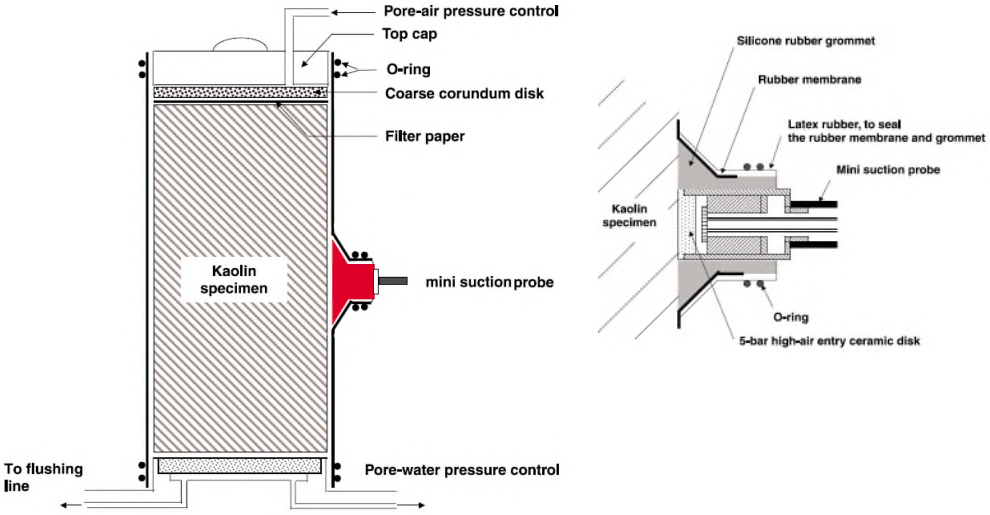

Figure 3.16. Installation of the mini suction probe to the specimen. (a) Only the mid-level mini suction probe is shown. (b) Details of the mini suction probe placed on a kaolin specimen (Meilani et al. 2002).

Meilani et al. (2002) reported the results of three tests (TU25-100, TU25-200 and TU100-400) conducted on compacted specimens of kaolin. Figure 3.17 shows the pore-water pressure measurements obtained by the three probes installed along the height of specimen TU25–100, for the matric suction equalization and shearing stage. Starting from a fully saturated sample, a matric suction of 100 kPa was applied by imposing an air pressure of 290 kPa to the top of the soil specimen and subsequently lowering the water pressure at the bottom of the specimen from 290 to 190 kPa. The probes sustained 100 kPa of positive pressure for about 130 h until the shearing stage was complete. During shearing, the pore-water pressure increases slightly. This increment was stopped and the pore-water pressure stabilized by reducing the strain rate from 0.001 mm/min to 0.0008 mm/min. For tests at suction value of 200 and 400 kPa (TU 25–200 and TU100-400) information about the values of the pore-water pressure imposed is missing. However, the authors report errors in tensiometers readings due to air diffusion; these took place about 30 h after (for TU25-200) and even before (for TU100-400) shearing.

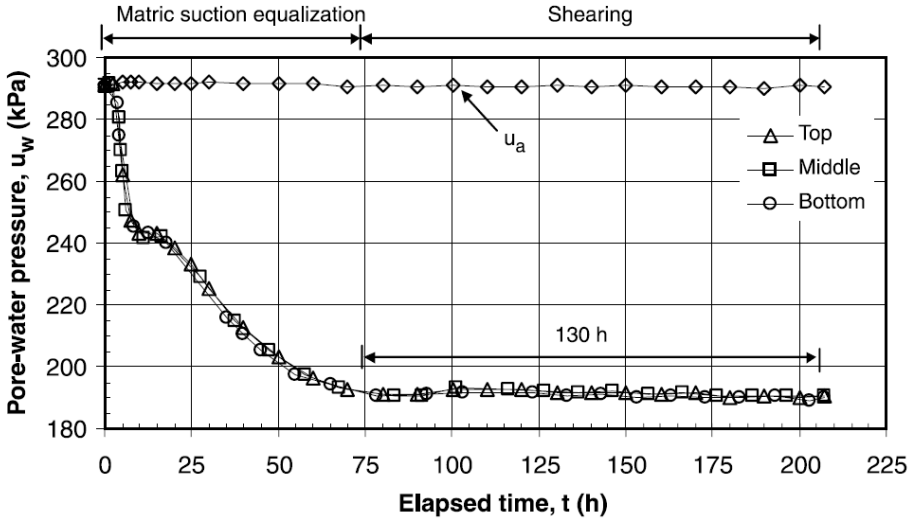

Figure 3.17. Pore-water pressure measurements during matric suction equalization (s = 100 kPa) and the shearing stage (Meilani et al. 2002).

Meilani et al. (2002) conclude that testing time has to be as short as possible to avoid diffusion that causes cavitation. The authors also recommended the use of an optimum strain rate during the shearing stage to reduce the testing time.

Gallage and Uchimura (2006) tested recompacted soil specimens of silt-sand by using a modified triaxial which simplified scheme is drawn in Figure 3.18. The

apparatus was designed to test unsaturated samples measuring 75 mm in diameter and 150 mm in height. The suction was controlled by means of the axial translation technique. The pore-air pressure was applied through the top cap and the pore-water pressure is controlled at the sample bottom. The apparatus is equipped with a miniature pressure transducer to measure pore-water pressure inside the sample (Figure 3.18). The local measurement of pore-water pressure was done to verify if the equalization of desired suction is achieved inside the sample. During sample compaction, the miniature pore pressure transducer was placed at two-third height from the bottom of sample.

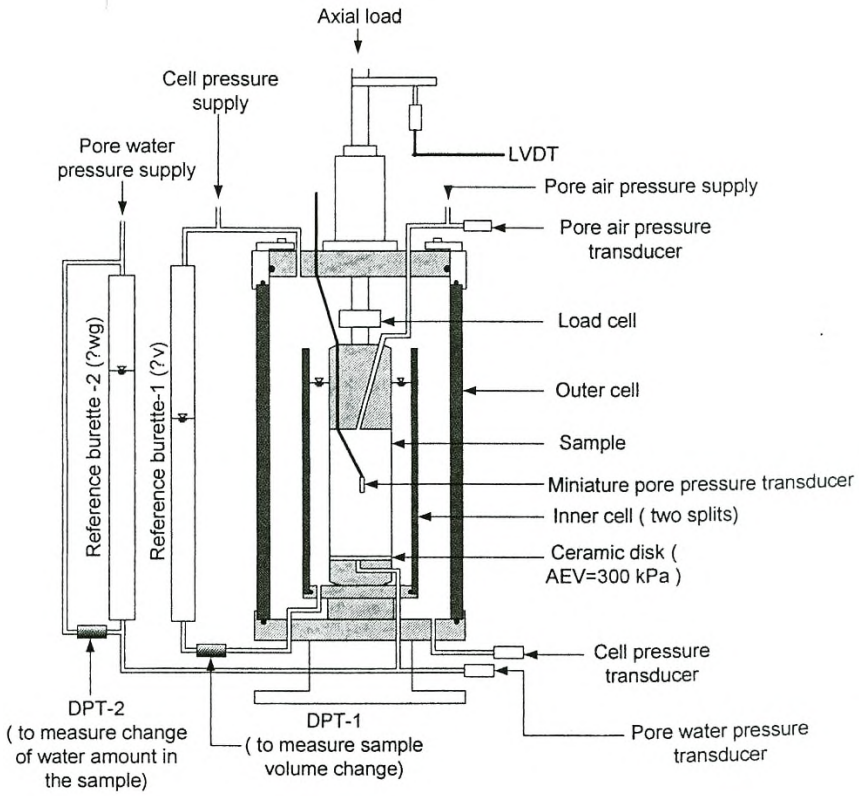

Figure 3.18. Modified triaxial apparatus for unsaturated soil testing (Gallage and Uchimura 2006).

Figure 3.19 depicts the pore-water pressure measurements during equalization after axis translation application. The equalization was ensured when the pore water pressure measurement of the miniature sensor was relatively equal to the applied pore-water pressure.

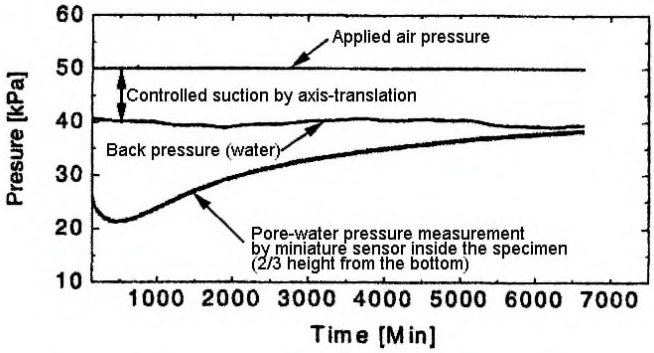

Figure 3.19. Pore-water pressure equalization at wetting (Gallage and Uchimura 2006).

Summarizing, the triaxial apparatuses modified to conduct suction controlled test and measure pore-water pressure use the axis translation technique to impose suction on soil samples (except Cunningham et al. 2003). In these equipments the pore-air and pore-water are controlled by the top and bottom of the sample. Under this configuration both ends of samples are occupied by the systems of pore-air and pore-water pressure control. Then, only is possible to install probes in the side or inside the samples. The presence of probes in these points may be considered as an invasive technique affecting samples behaviour during tests. On the other hand, the testing time is a crucial factor for probes response. The reliability of measurements is conditioned by the volume of air diffused into the probe that affects the instrument performance. Then, an optimum strain rate should be applied to reduce the testing time and to avoid diffusion that causes cavitation.

Chapter 4

UNSATURATED STRESS PATH TRIAXIAL CELL

4.1 INTRODUCTION

Starting from 1994, a triaxial device (USP) has been developed at the University of Napoli Federico II in order to test soils under unsaturated conditions (Rampino 1997). In the original version of this cell, a modified version of a Bishop & Wesley (1975) apparatus, the axis-translation technique (Hilf 1956) was used, with pore-air and pore-water pressures controlled at the top and bottom of the sample, respectively. The USP device has been used during several testing campaign as for example Rampino et al. 1999; Aversa & Nicotera 1999; Bilotta et al. 2005; Vassallo et al. 2007; Casini et al. 2007; Cattoni et al. 2007; Papa et al. 2008.

4.2 UNSATURATED STRESS PATH TRIAXIAL CELL – 2nd VERSION

A triaxial apparatus capable of testing unsaturated samples under controlled-suction condition were developed at the Department of Geotechnical Engineering of the University of Naples Federico II in association with Megaris company. A scheme of the triaxial apparatus, named USPv2 (Unsaturated Stress Path, 2nd version), is presented in Figure 4.1.

The USPv2 triaxial device is an improving of the Rampino's (1997) apparatus in order to control air and water-pore pressures by both ends of the soil specimen. The

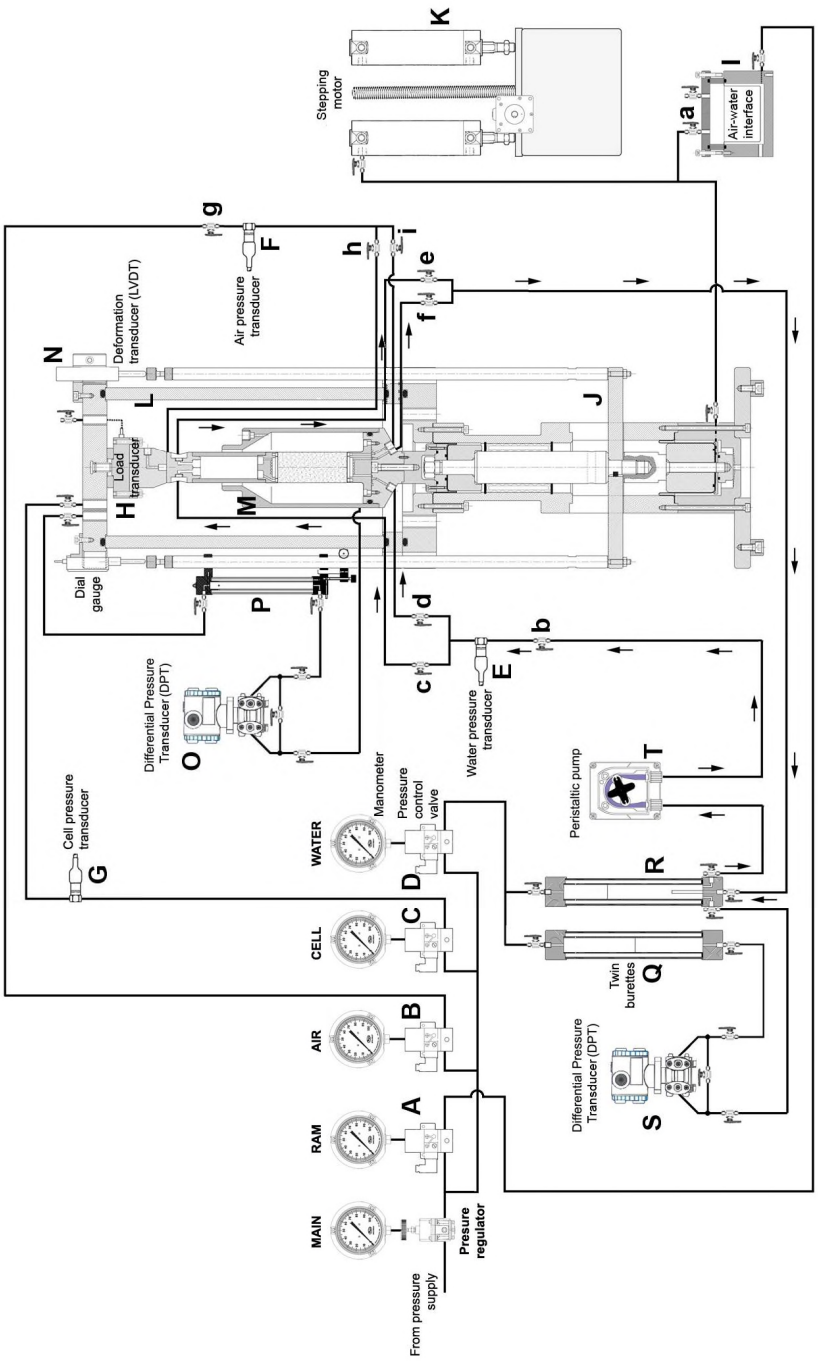

Figure 4.1. Scheme of USPv2 triaxial apparatus.

suction is controlled by means of the axis translation technique (Hilf 1956). The apparatus is designed to test unsaturated samples of 38 mm in diameter and 76 mm in height in both axial compression and axial extension under either controlled rate of loading or controlled rate of strain.

The main new features of the USPv2 different from the original USP triaxial device proposed by Rampino et al (1999) are:

1. The inclusion of a double drainage system to shorten the testing time.
2. The capability to measure pore-water pressure changes during suction-controlled isotropic compression tests (see Chapter 8).
3. The replacement of the inner acrylic cell by a stainless steel cell to eliminate the effect of cell pressure and water absorption

Two USPv2 triaxial apparatuses were constructed. In this work the letters L (left) and R (right) are used to identify the equipments in relation of their position on Figure 4.2.

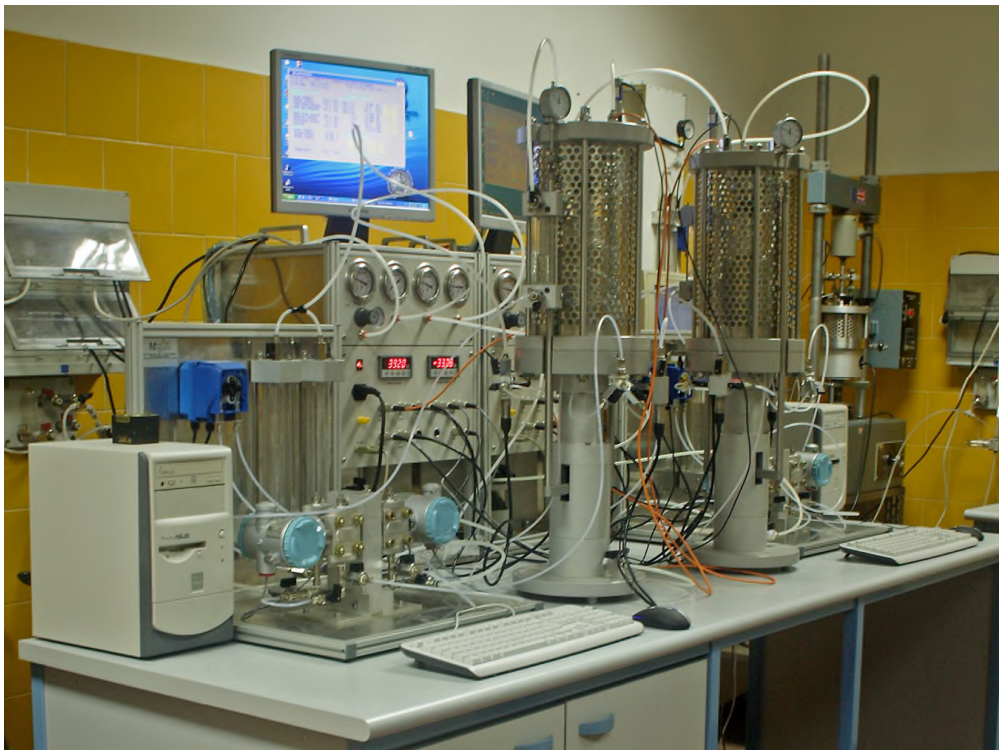

Figure 4.2. The two triaxial apparatus model USPv2.

4.3 TESTING CONTROL AND DATA ACQUISITION

The automated triaxial testing system uses closed-loop feedback systems to control the loadings (i.e. axial load, cell pressure, pore-air pressure and pore-water pressure). In this closed-loop control system, the transducers read the output variables and give voltage inputs to a computer via an analogue to digital board. Based on what reference value is set within the computer program, the control system continuously adjusts the actuator input voltage to increase or decrease the load as necessary to keep the control error to a minimum. Feedback on how the system is actually performing allows the actuator to dynamically compensate for disturbances to the system, such as load variations, parameter variations and other disturbances (e.g. temperature variations). This process is continuous during the test.

Table 4.1. Specifications of the pressure control valves.

Control	Device	Manufacturer /Type	Rated limit (FSD)	Supply sensitivity*	Calibration factor [kN/bit]
RAM	R	Norgren VP10	800 kPa	± 0.025 %	5.2742
	L				5.1332
Cell pressure	R				5.1840
	L				5.1324
Water pressure	R				5.1377
	L				5.0937
Air pressure	R				5.0738
	L				5.1983

* span output change per % supply pressure change

The voltage output of transducers are continuously acquired via analog to digital converters, transformed in engineering unit values by applying linear calibrations, and finally recorded in data files. The logged data are: time, axial load, cell pressure, pore-water pressure, pore-air pressure, radial volume change, water volume change and axial displacement.

The stress state on the tested specimens is obtained regulating the air pressure supplied by an air compressor through four electro-pneumatic pressure converters (A, B, C, D in Figure 1), and controlled in feedback through the pressure transducers E and F for the pore-water and pore-air pressures, respectively, and by the pressure transducer G and the load cell H, for the cell (σ_c) and deviatoric (q) stresses, respectively. The output range of pressure converters is 20 kPa to 800 kPa and the pressures are controlled to within ± 1 kPa of the targeted value. The main characteristics of pressure control valves and transducers are presented in Table 4.1 and Table 4.2, respectively.

Table 4.2. Specifications of the transducers.

Transducer	Device	Manufacturer /Type	Serial number	Rated limit (FSD*)	Accuracy (% FSD)	Calibration factor [kN/bit]
Load cell	R	CCT	2203	300 kg		7535.6
	L	BC02	2202			7615.8
Cell pressure	R	Druck PDCR810	2160106	1000 kPa	± 0.1	31.361
	L		2160109			31.008
Air pressure	R		2160109			31.110
	L		2163500			31.063
Water pressure	R		2160103			31.124
	L		2160111			31.103
Water volume	R	Druck STX2100	A3L1724F	60 mbar	± 0.1	---
	L		A5G9218F			---
Radial volume	R		A5G9216F			---
	L		A3M2813F			---
Axial deformation	R	RDP ACT500A	80963	±12.5mm	±0.25	-1192.6
	L		80964			-1194.4

* FSD = Full Scale Deflection; R = right apparatus; L = left apparatus (see Figure 4.2).

4.4 SUCTION CONTROL SYSTEM

The main change introduced in the USPv2 is the inclusion of a double drainage system to reduce the drainage path, and consequently to shorten the testing time. As a matter of fact, the base platen and the top-cap in Figure 4.3 incorporate a combination of two different porous disks, including a peripheral annular standard porous stone (3 mm thick porous stainless steel) connected to the pore-air pressure line and an internal HAEV disk (7 mm thick and 24 mm in diameter) connected to the pore-water pressure line. The HAEV disk has been sealed in the top-cap and base platen, using epoxy resin in order to prevent the passage of air and water around its circumference.

Operating by such a system suction control and the drainage of air and water is allowed by both the sample ends. The new design includes the possibility to change the base platen and the top-cap in order to select different values of the air entry pressure of the HAEV disk

To apply pore-air and pore-water pressure by the upper end of specimen, leak-tight connections are inserted in the top part of the top-cap (Figure 4.4). This arrangement hinders the positioning of the inner cell when the top-cap is placed onto the specimen. For this reason the design of top-cap has been split in a loading cup containing the porous elements and a top part hosting the joints of the water and air lines (Figure 4.4). During the assembling process, initially only the loading cup is mounted in the upper part of specimen. After that, the rubber membrane is

positioned. Subsequently, as represented in Figure 4.4, the inner cell is placed and the top part is screwed on the top of the loading cap.

On screw tightening, sample disturbance is avoided using an auxiliary split collar to resist the torque and consequently to eliminate the torsional strength acting on the soil sample. By this way, the tilting and bedding errors (Figure 4.5) that can be induced during the set-up of a sample are minimised. These measures introduced to allow an accurate sample positioning are believed crucial especially when loss sands or soft clays are tested. This design greatly simplifies and speeds up the test set-up.

A single system is used to measure and control pore-water pressure at base and top of the sample. The electro-pneumatic converter D (Figure 4.1) controls the sample pore-water pressure, and the pressure transducer E measures it. Nevertheless, a system of valves lets to drainage or circulates water separately by the base platen or top-cap (Figure 4.6a, b).

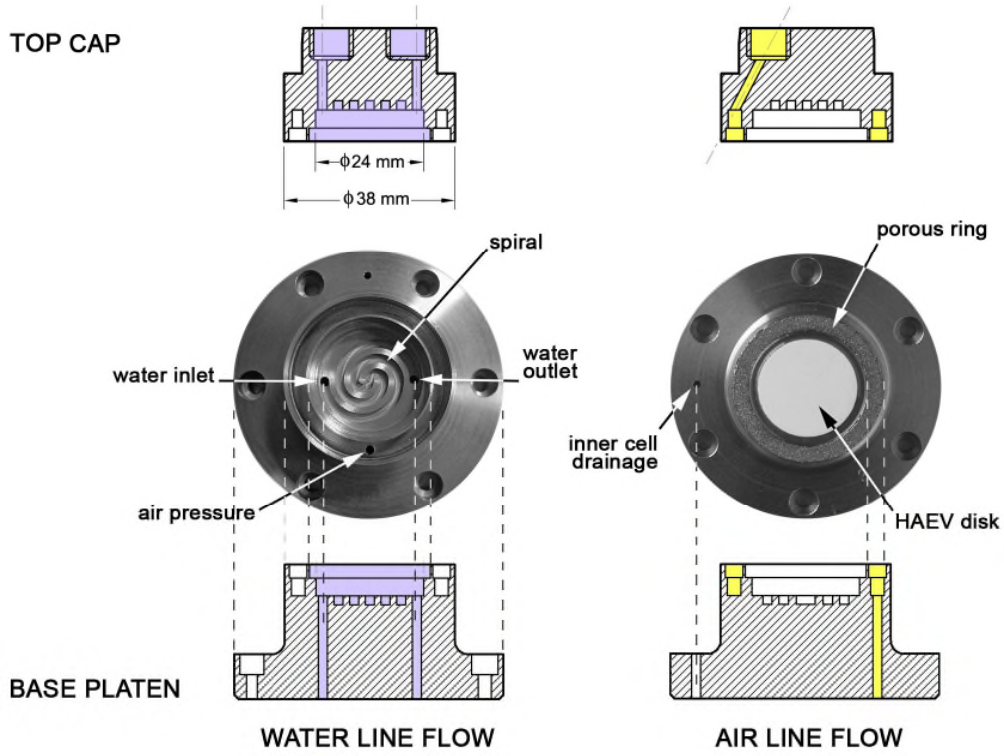

Figure 4.3. Top-cap and base platen design of USPv2 triaxial cell.

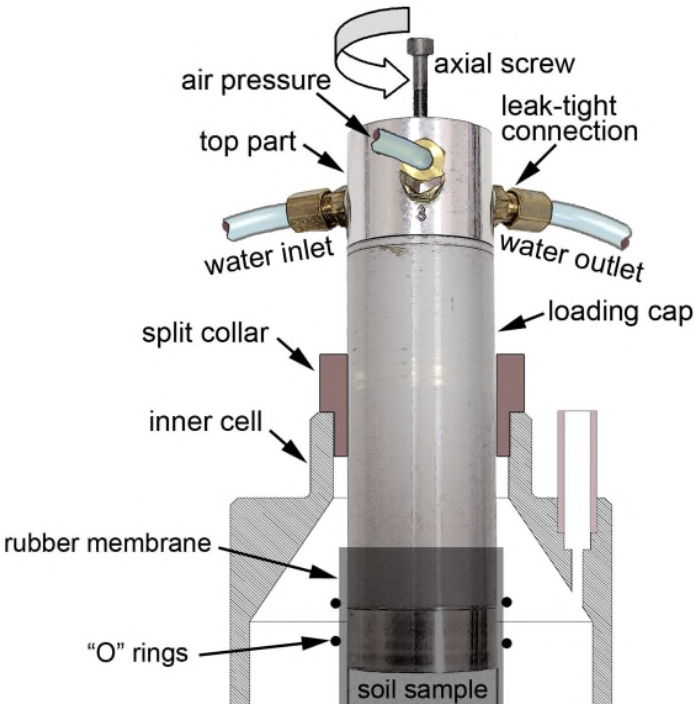

Figure 4.4. Top-cap assembling.

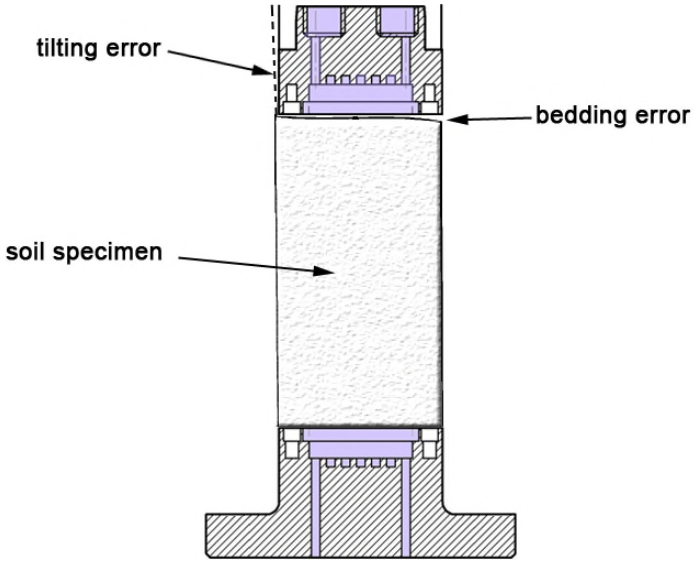

Figure 4.5. Tilting and bedding errors caused by set-up of a sample.

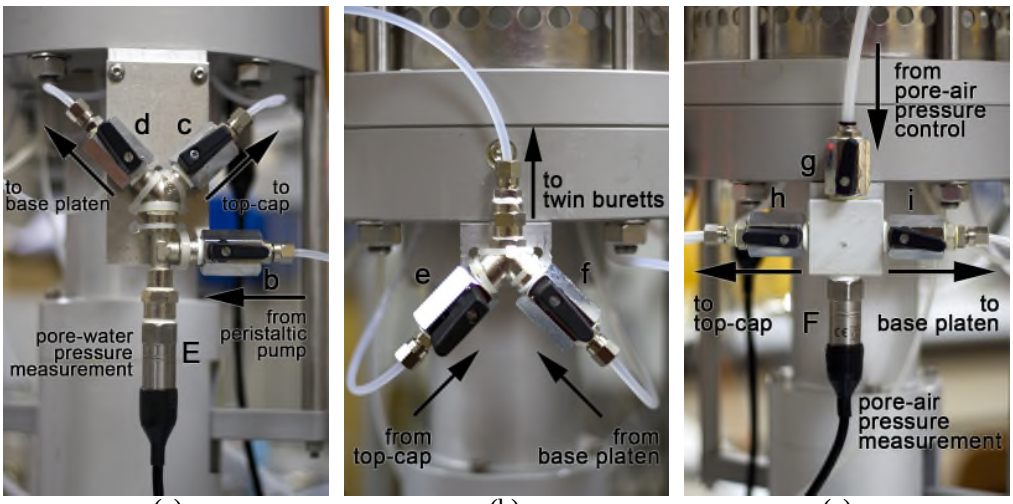

(a) (b) (c)

Figure 4.6. Valves arrangement to flow distribution. a) upstream water line; b) downstream water line; c) air line.

The pore-air pressure is controlled in feedback by the electro-pneumatic converter B and measured by the pressure transducer F (see Figure 4.1). The system to measure and control pore-air pressure at base and top of the specimen is unique. Similar to pore-water pressure line, via a valves system (Figure 4.6c) the air pressure can be supplied separately by the base and top of specimen.

All the pressure transducers and electro-pneumatic converters have been calibrated against a precision calibrator (i.e. Druck MCX-II). The results of calibration procedure are presented in Annex A, and the slope of the linear calibration functions is presented in Table 4.1and Table 4.2.

4.5 CELL PRESSURE MEASUREMENT/CONTROL

The electro-pneumatic converter **C** is used to control the cell pressure and the pressure transducer **G** to measure the confining pressure of the cell (Figure 4.1). Also in this case the devices **C** and **G** have been calibrated against a precision calibrator (Druck MCX-II). The calibration curves are in Annex A.

4.6 AXIAL LOAD MEASUREMENT/CONTROL

The magnitude of the axial load acting upon the soil sample is measured using a submergible electric load cell (**H** in Figure 4.1) type CCT-BC02 (Figure 4.9). This device is placed inside the cell, this avoid the error due to the friction between the piston and the outer cell cap. Calibration of the load cell was done using dead loads. The result of a loading/unloading cycle was reported to give a linear plot with no hysteresis for the load cells; the calibration curve is in Annex A, Figures A.15 and A.16.

The electro-pneumatic converter (**A**) controls the axial load: the air pressure passes through the air-water interface **I** and is converted to hydraulic pressure controlling the moving pedestal **J** and pushing the soil sample against the stationary load cell **H**, see Figure 4.1.

The valve **a** allows to switch from stress to strain control thanks to a dual axial control. A stepping motor (**K**) drives the screw pump for the axial strain control.

4.7 MEASUREMENT OF SPECIMEN VOLUME CHANGE

Volume change of the soil specimen in triaxial tests is essential in cases such as in consolidated drained triaxial tests. The volume change of a soil specimen tested is an indispensable parameter, which shall be measured and is valuable for understanding the volumetric compression or dilation characteristics of the soil.

Measurement of total volume changes in an unsaturated soil specimen is much more complicated than on a saturated soil specimen. In a saturated soil, the volume change of a specimen during consolidation or compression is generally assumed to be equal to the volume of water coming out or into the specimen, and is relatively easy to measure it using a volume gauge. In an unsaturated soil, however, the water volume change constitutes only part of the overall volume change of a specimen. The total volume change involves two components: changes in the volume of the air and changes in the volume of the water present in the specimen voids.

Bishop and Donald (1961) used a double system (i.e. an open-top inner cell inside an outer cell) for measuring volume changes of partly saturated soils. The proposed method is based on the measurement of the volume of fluid entering or leaving the confining pressure cell to compensate for the volume change of the soil specimen. The bottom of the inner cell was filled with mercury and the rest of the inner cell is filled with water, which is connected to the water in the outer cell to maintain equal pressure between the cells. Volume changes were measured by monitoring the

vertical position of a stainless steel ball floating on the surface of the mercury using a cathetometer. Afterwards, the double cell technique was modified by using air to provide the confining pressure above the inner cell filled with water (e.g. Yin (1998); Rampino et al. (1999); Aversa & Nicotera (1999)).

For continuous measurement of the volume change the USPv2 triaxial apparatus uses the Bishop & Donald (1961) double cell technique using air above a water-filled inner cell, as shown in Figure 4.1. The next paragraphs are devoted to describe the main parts of the system used to measure volume change.

4.7.1 *Outer cell*

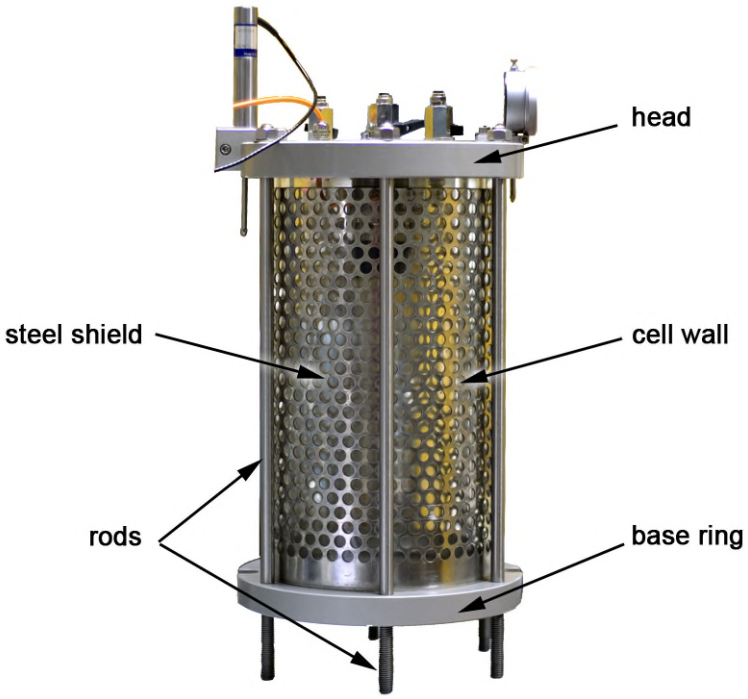

Figure 4.7. Outer cell.

The outer cell (Figure 4.7 and **L** in Figure 4.1) is constituted by a stainless steel head and base ring connected to a cell wall made of Poly(methyl methacrylate)[1]. Six

[1] Poly(methyl methacrylate) is a highly transparent, water-white, crystal-like solid similar to glass at room temperature, is available commercially under the trade names Lucite, Perspex, or Plexiglas,

external rods are used to connect the parts. The cell wall, with 1.6 cm in thickness, has a confining pressure capacity of 1000 kPa. The internal dimensions of the cell are 16.8 cm in diameter and 31.5 cm in height. Pressurized air is used to provide the confining pressure above the inner cell filled with water. As the use of pressurized air in the pressure cell poses safety concerns, a perforated cylindrical steel shield around the cell acts as protection of an eventual cell failure. Also has been included a pressure relief valve for operator safety (Figure 4.7).Figure 4.8 shows the cell base design where 10 take-off positions are drilled for pore-water pressure lines (4 positions), pore-air pressure lines (2 positions), cell pressure measurement, inner cell drainage and two auxiliary positions. Take-off positions are also drilled in the head (Figure 4.9) for cell pressure control (2 positions), pressure relief valve, load cell wire, suction cup air purge and one auxiliary position. Two anvils for a dial gauge and a transducer datum are fitted to the cell head.

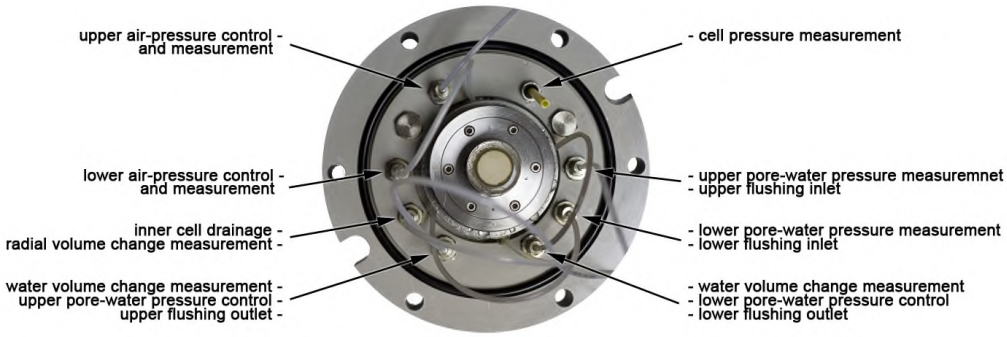

Figure 4.8. Cell base design.

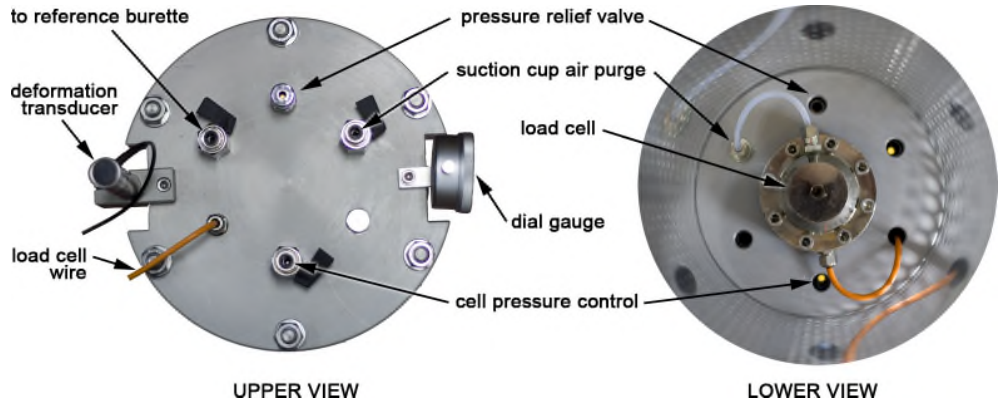

Figure 4.9. Upper and lower view of the head cell.

4.7.2 *Inner cell*

The inner cell is a cylindrical bottle-shaped device (Figure 4.10, and **M** in Figure 4.1) made of stainless steel to avoid cell expansion due to cell pressure and water absorption from the measuring device it self (Agus et al. 2000). At the upper end of the cell (bottleneck) the internal diameter (46 mm) is slightly larger than the diameter of the top-cap (38 mm), in this way, the sensitivity improves due to the small cross-sectional area (528 mm^2) at the bottleneck. The measurement of water level changes is conducted inside the bottleneck region. To observe qualitatively the water level variations a thin glass piezometer has been included. The cross-sectional area of the piezometer (31.2 mm^2) is added to obtain the total area (559.2 mm^2).

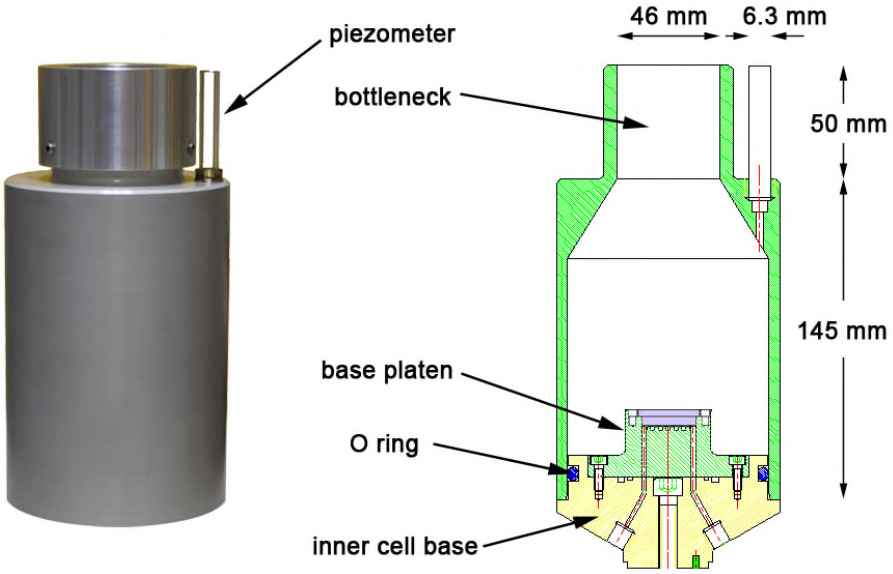

Figure 4.10. Inner cell and his cross-section view when mounted.

4.7.3 *Axial strain*

The axial sample strain (ε_a) is measured by means a commercial Linear Variable Differential Transformer (LVDT) displacement transducer type RDP-ACT500A (**N** in Figure 4.1), with a maximum displacement of 25 mm. The LVDT is fixed to the top of the outer cell, as shown in Figure 4.9, making an accurate position measurement of the movement of the moving pedestal (**J** in Figure 4.1) relative to the outer cell, allowing the calculation of the axial sample strain. Calibration of the LVDT transducers is simple and was done by means a micrometer mounted over a bench; the results are presented in Appendix A.

4.7.4 *Radial strain*

As mentioned before, the radial volume change (ε_r) of the specimen is monitored by the change in the volume of water inside inner cell. The differential pressure transducer (**O** in Figure 4.1) register the pressure difference between the water level in the water bath surrounding the soil sample (i.e. water into the inner cell) and the water level of an external reference double walled burette (**P**) (Figure 4.11). The specification of the DPT is presented in Table 4.2. To minimize the water evaporation, a thin layer of silicon oil above the water surfaces of the inner cell and the reference burette is applied.

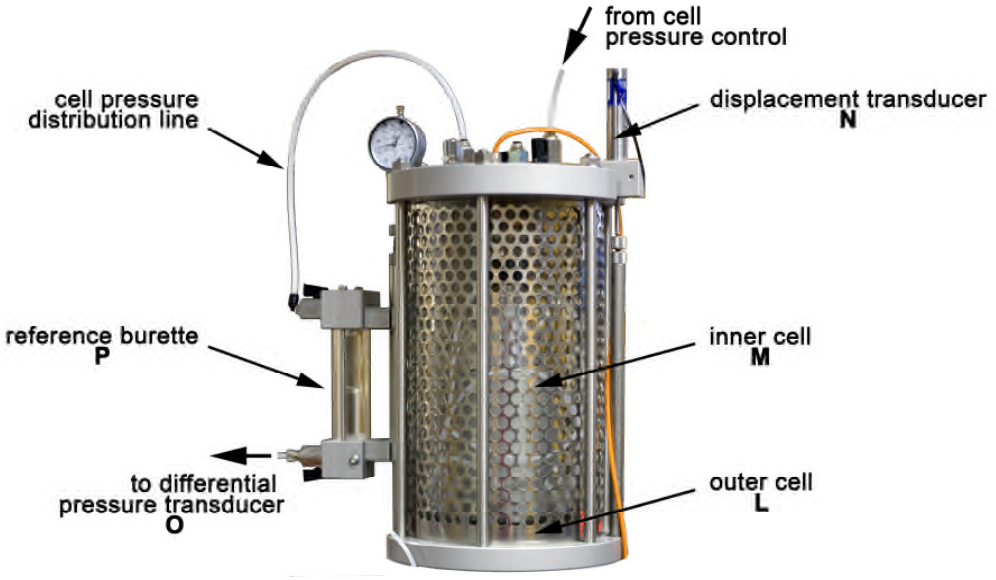

Figure 4.11. Reference burette and inner cell.

The average radial strain is related to the water level changes in the inner cell (ΔI_r), as follows (Aversa & Nicotera 2002):

$$\varepsilon_r = -\frac{1}{2}\frac{A_b - A_{s0}}{V_{s0}}\Delta I_r \tag{4.1}$$

where: A_b and A_{s0} represent respectively the cross section of the inner cell and the initial sample cross section, while V_{s0} is the initial volume sample. Due to the inclusion of piezometer (Figure 4.10), its cross section (A_p) should be added:

$$\varepsilon_r = -\frac{1}{2}\frac{A_b + A_p - A_{s0}}{V_{s0}}\Delta I_r \tag{4.2}$$

To calibrate the system, as Aversa & Nicotera (2002) suggested, precise amounts of water (100 mm^3) measured with an accurate pipette were introduced into the inner cell in order to relate the term $\Delta V = (A_b + A_p - A_{s0}) \times \Delta I_r$ in Eq. 4.1 to the output of the DPT. The results of the calibration are presented in Figure A-19 and A-20 in Annex A.

4.8 MEASUREMENT OF WATER VOLUME CHANGE

Changes in soil water content are obtained measuring the water volume by means of two double walled burettes (Figure 4.12) connected to the HAEV disks (Figure 4.3). Any change between the level of water in the reference burette (**Q**) and in the measurement one (**R**) is obtained by means the differential pressure transducer (**S**). The signal convention refers as negative the water that get out of the sample and positive the get in water. The water level variation due to evaporation at the water-air interface in the burettes is balanced by the system symmetry.

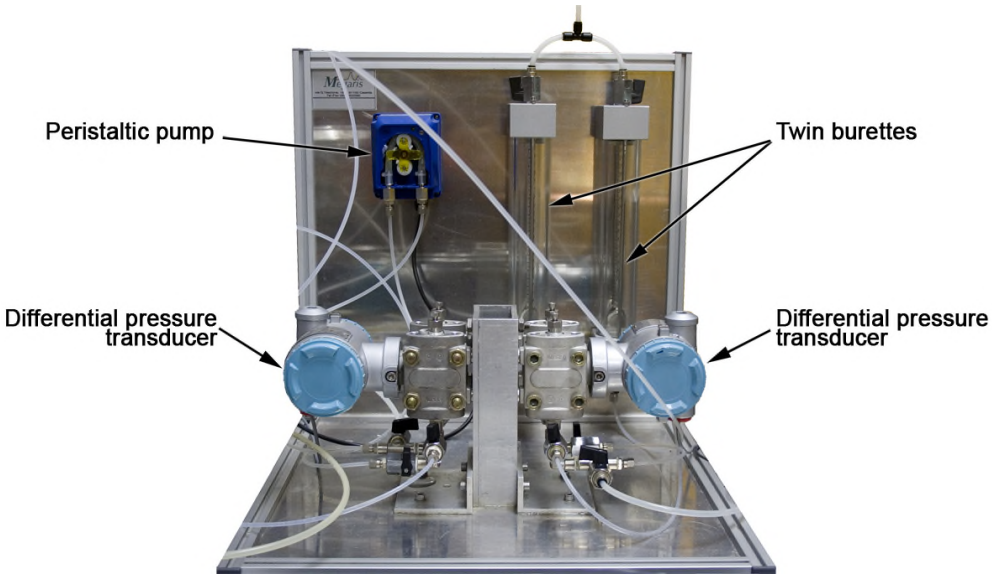

Figure 4.12. Devices used to measure water and radial volume change.

Due to technique used to control the matric suction (i.e. axis translation), water losses as evaporation flux on pore-air pressure control lines and air diffusion on pore-water pressure control lines disturbs the water volume change measurements. Evaporative fluxes originated in the difference in vapour pressure between soil voids and the overlying at open system is detected in the water volume change devices

under steady-state conditions. In order to accurately determine water volume changes it is necessary to account for water volume losses due to evaporation in the open-air pressure chamber. The evaporation is registered as water inlet into soil mass, and the diffusion as water outlet.

The rate of evaporation linearly decreases with the imposed matric suction (Romero 1999; Airò Farulla & Ferrari 2005; Rojas et al. 2006). De Gennaro et al. (2002) indicate that an exponential relation exists between the rate of diffused air and the applied pressure.

In the USPv2 a peristaltic pump (**T**) (Figure 4.12) is used to eliminate the air diffused in the water drainage line; the speed of the pump can be adjusted with a trim potentiometer, in order to obtain flow rates from 0.3 l/h to 1.0 l/h. The peristaltic pump acts on the drainage line flushing water through the spiral circuit carved inside the base pedestal (Figure 4.3) and top cap, drives the air bubbles into the burette **S** and expels them acting as an air trap. The arrows on Figure 4.1 shows the water path followed during the flushing process.

4.9 CELL SETTING UP

Each step of the cell setting up is shown in Figure 4.13 and illustrated in the following:

Step 1 – clean the water placed onto the HAEV disk using a humid wipe.

Step 2 – place the specimen on the base platen. Check that the specimen is aligned vertically.

Step 3 – place gently the loading cap on the upper end of the specimen.

Step 4 – fit the rubber membrane to the specimen using a membrane stretcher, and seal the ends of the rubber membrane with O-rings.

Step 5 – to positioning the inner cell, lower it carefully over the specimen taking care not to knock the specimen with the walls of the cell. When the device is positioned centrally over the specimen push down up to ensures the maximum contact with the base. The finish between the inner cell and his base includes the fitting of an O-ring seal and the use of silicon grease to reduce friction to a minimum and prevent water leakage.

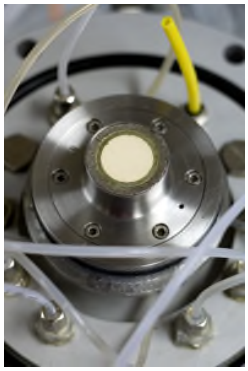
Step 1


Step 2


Step 3


Step 4


Step 5


Step 6

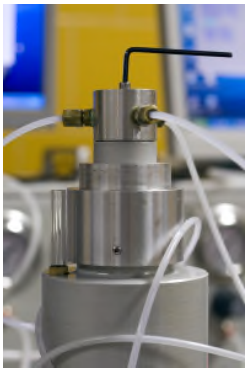
Step 7


Step 8

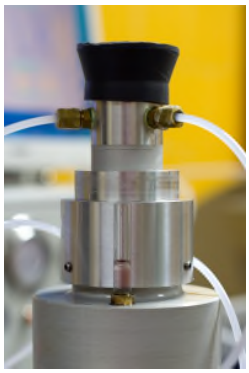
Step 9


Step 10


Step 11


Step 12

Figure 4.13. Steps of the cell setting up.

Step 6 – place the two parts of the auxiliary split collar on the open end of the inner cell.

Step 7 – position the top part on the top of the loading cap so that the index mark is coincident. Fix the two parts by means of an axial screw. During the screwing process hold the split collar steady with one hand to resist the torque and consequently to eliminate the torsional strength acting on the soil specimen.

Step 8 – fill the inner cell with distilled deaired water, slow down the rate of filling as the water level nears the top, and as soon as the water reaches the middle part of the glass piezometer shut off the water supply. The water is allowed into the inner cell from the supply line using the inner cell drainage (Figure 4.1).

Step 9 – place the rubber suction cup on the top-cap.

Step 10 – ensure that the cell sealing ring is in position. Lower the cell body (i.e. cell wall and base ring) into position over the specimen. After that, move away the auxiliary split collar and cover the water surface on inner cell with a thin layer of silicon oil. Overlaying the water with silicon oil prevents evaporation effects.

Step 11 – place gently the head cell on the top of the wall cell. Six external rods are used to connect the cell parts with his base, seat properly the nuts on the upper and lower part of the rods. The tightening should be done systematically, first opposite pairs moderately tight, then two other pairs, and so on, and gradually increase the tightness in similar order.

Step 12 – finally, mount the external reference burette and the reference rod to measure the axial deformation by means the LVDT transducer.

Chapter 5

HIGH CAPACITY SUCTION PROBES

5.1 INTRODUCTION

The initial literature survey mainly deals with design considerations of strain-gauged instruments not because the concepts involved are complex, but mainly due to the fact that knowledge in this field is limited among geotechnical engineers.

In order to study the cavitation phenomena in suction measurement instruments such as high capacity tensiometers, it is necessary to have a good knowledge of both the water phase change and the nucleation phenomena in free water as well as water in contact with a surface. A recall of the theoretical framework for addressing this issue has been presented, before pointing out its relevance in suction measurement.

The two high capacity tensiometers developed at University of Napoli Federico II are described together with a saturation device that has been also designed.

Finally, free evaporation tests, cyclic evaporation tests and equilibration time tests are described and evaluated here.

5.2 HIGH CAPACITY TENSIOMETERS

Tensiometers are based on the high tensile strength of the water that can directly measure in a soil (matric suction). In relation to the capacity to measure matric suction, tensiometers are divided in two categories: low capacity tensiometers (able to measure suctions below 100 kPa) and high capacity tensiometers (above 100 kPa).

In this report the term tensiometer or suction probe is used to refer high capacity tensiometer.

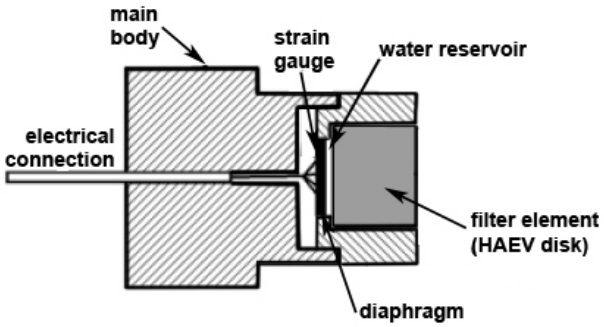

Figure 5.1. Imperial College tensiometer (after Ridley and Burland 1999).

Tensiometers have been developed in the last ten years by a number of researchers at different universities worldwide (e.g. Ridley and Burland 1993; Guan and Fredlund 1997; Tarantino and Mongiovì 2002; Take and Bolton 2003; Chiu et al. 2005; He et al. 2006; Lourenço et al. 2006). Depending on the particular design of the probe, different performances are obtained in terms of robustness, sensitivity, speed of response and ability to measure large suctions for long time.

Basically, a tensiometer is constituted of three parts (Figure 5.1):

1) a HAEV ceramic disk as the interface between soil and the pressure measurement device.
2) the water reservoir (a small gap between the HAEV ceramic disk and the diaphragm).
3) the system to measure pressure changes (diaphragm, strain gauge and electrical connection).

The suction measurement is obtained by the diaphragm responds to the external pressure applied. The water present in the water reservoir acts as a continuous medium that connect the HAEV ceramic disk and the diaphragm, getting possible the equilibrium between the pore-water pressure in the soil and the pore-water pressure in the water compartment. To reach the equilibrium, water flows from the water compartment into the soil, or vice versa.

As mentioned, many studies considering direct suction measurements with high capacity tensiometers have been published. Three important elements of probe's design are the pressure transducer, the volume of water reservoir and the elements used to seal the water reservoir. Table 5.1 summarizes information on the type of

Table 5.1. Design data of high capacity tensiometers.

Tensiometer	Pressure transducer		Water reservoir		
	Type	Range [Bar]	Sealing	Volume [mm^3]	Thickness [mm]
Ridley & Burland (1993)	Entran EPX-500	35	O-rings	3	0.25
Marinho & Chandler (1994)	Keller PR-27-100	---	---	---	---
Ridley & Burland (1996)	integral strain-gauged*	> 40	epoxy resin	---	0.1
Guan & Fredlund (1997)	non specified	15	O-rings	---	0.1 – 0.5
Marinho & Pinto (1997)	Entran EPX-35	---	epoxy resin¢	---	---
Muraleetharan & Granger (1999)□	Druck PDCR81	15	epoxy resin†	---	0.09
Tarantino & Mongiovì (2002)	integral strain-gauged*	40	epoxy resin‡	---	0.05 – 0.1
Meilani et al. (2002)	Druck PDCR81	15	epoxy resin§	---	0.4
Toker (2002)	Data InstrumentsAB-HP200	14	copper gasket	---	---
Take and Bolton (2003)	Entran EPB-C1	7	O-rings	---	---
Chiu et al. (2005)	Druck PDCR81	7	non specified	---	---
He et al. (2006)	Entran EPX-10I-250A	35	O-rings	2	0.1
Lourenço et al. (2006)	Ceramic Wykeham Farrance	8	epoxy resin	10	---
Mahler & Diene (2007)	Entran EPX1,01;ASH1,2	5 – 15	O-rings	5 – 112	0.2 – 3

* home made; ¢ loctite No.542; □ low capacity tensiometer; †Dow Coring No.3145; ‡ Araldite® 2011; §Araldite® 2021.

pressure transducer and characteristics of the water reservoirs used by the various authors. As regard their diaphragm, tensiometers may be classified as:

- commercial transducer
- integral strain-gauged

And as regard the reservoir sealing, tensiometers may be:

- O-rings
- epoxy resins
- copper gasket

5.2.1 *Tensiometers based on commercial transducers*

Tensiometer designs have been presented in the literature where the probe was obtained by fitting a high AEV disk to a commercial transducer. Some of the pressure transducer used to construct suction probes are shown in Figure 5.2.

The first high-capacity tensiometer by Ridley & Burland (1993), presented in Figure 5.3, establish a significant progress in direct suction measurement. This tensiometer basically is composed of a HAEV ceramic disk, the water reservoir and a commercial pressure transducer. The novel instrument uses a 35-bar miniature pore-water pressure transducer, Entran EPX series (similar to Entran EPB in Figure 5.2c), manufactured by Strain Sense Limited.

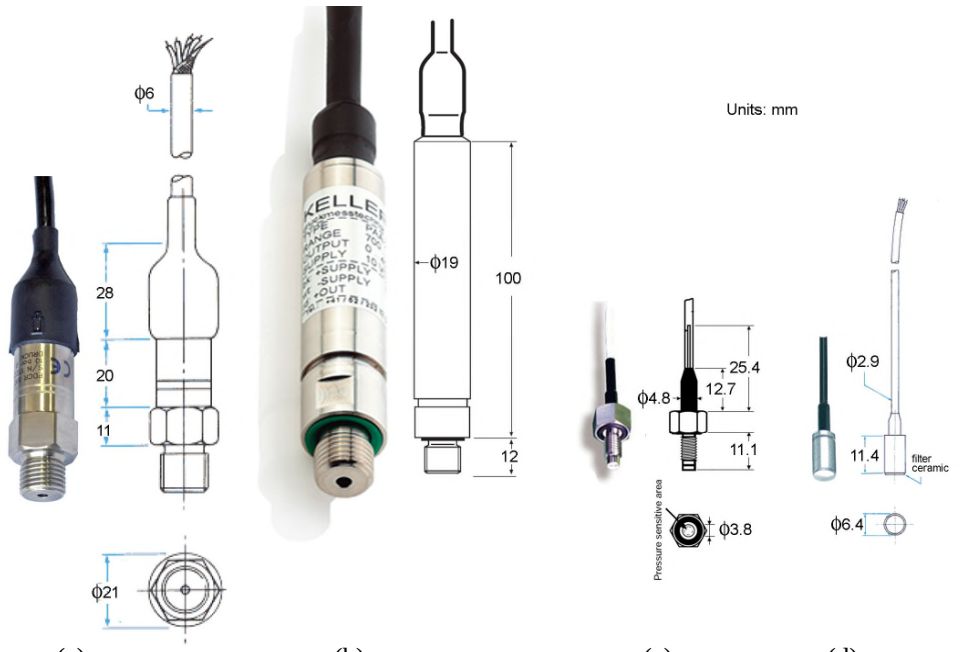

Figure 5.2. Pressure transducers: (a) Druck PDCR 810; (b) Keller series 27 W; (c) Entran EPB; and (d) PDCR 81

After the pioneer probe of Ridley & Burland (1993), authors like Guan and Fredlund (1997), Marinho and Pinto (1997), Take and Bolton (2003) and Mahler and Diene (2007) used Entran bonded-gauge transducers (see Table 5.1 and Figure 5.2c) as sensor in the design of high capacity tensiometer. Figure 5.4, Figure 5.5, and Figure 5.6 shown some Entran transducer based probes.

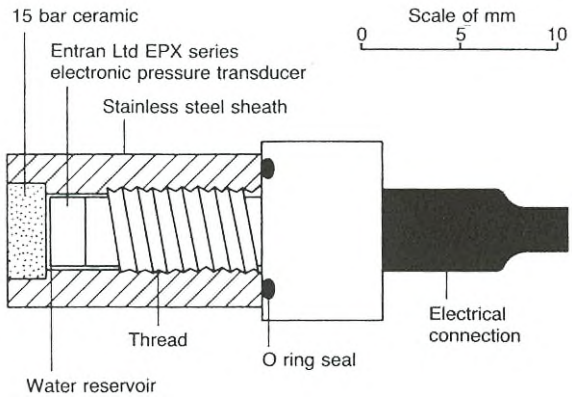

Figure 5.3. Imperial College tensiometer (Ridley and Burland 1993).

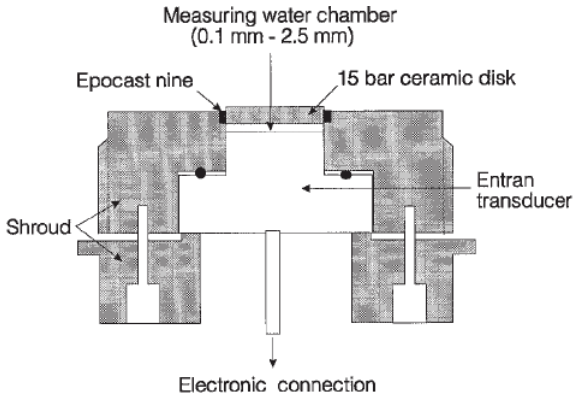

Figure 5.4. Saskatchewan suction probe (Guan and Fredlund 1997).

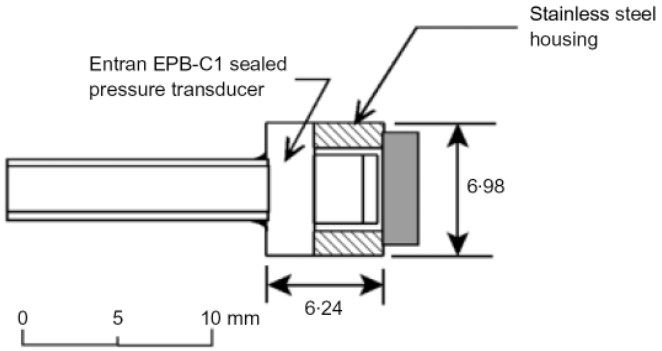

Figure 5.5. Prototype commercial design of a pore pressure and tension transducer (Take and Bolton 2003).

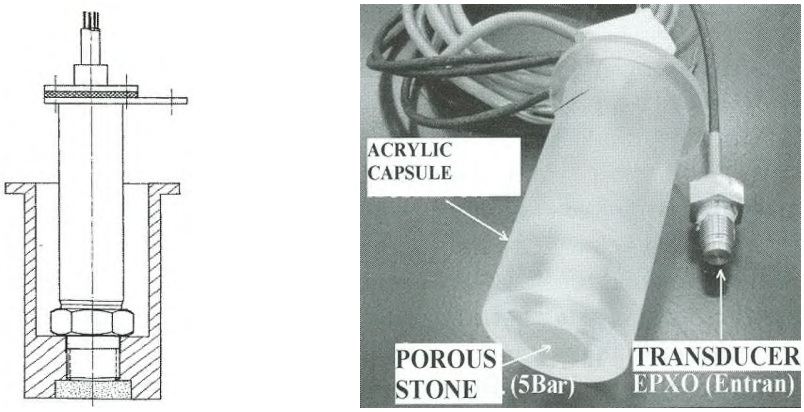

Figure 5.6. Suction probe (Mahler and Diene 2007).

The miniature pore pressure probe Druck PDCR81 (Figure 5.2d) has been successfully used in measuring positive pore water pressures in testing of saturated soils. Muraleetharan and Granger (1999) tested the probe PDCR81 to determine if it can also be used in measuring the negative pore water pressure in unsaturated soils to measure matric suction. Is important to note that the mentioned Authors used a PDCR81 transducer attached to a high-air entry ceramic disk as shown in Figure 5.7 and Figure 5.2d, and that the AEV of the ceramic disk is around 100 kPa. Muraleetharan and Granger (1999), using the original HAEV ceramic disk, analyzing low suction ranges (i.e. less than 100 kPa) found that this transducer can be effectively used in measuring negative pore water pressure in unsaturated soils.

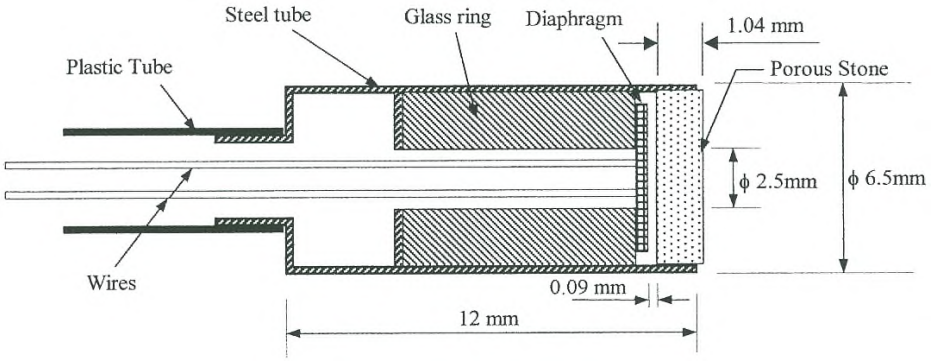

Figure 5.7. Miniature pore pressure transducer PDCR81 (Muraleetharan and Granger 1999).

Meilani et al (2002) use the PDCR81 to measure suction during shear triaxial tests. As the maximum expected suction was in the 200 kPa range, hence, the original ceramic disk was removed and replaced with a new high-air entry ceramic disk (5 bar). Figure 5.8 presents the transducer and the substituted porous ceramic. The response of the mini suction probe was found satisfactory when used to measure matric suctions up to 400 kPa.

Take and Bolton (2003) observe that the pressure transducer PDCR81 exhibits exceptional performance characteristics for the measurement of positive pore pressures, however, presents a lack of robustness for the measurement of high suctions means it is not ideally suited for this application. These authors identify three weaknesses:

- under large tensile pressures, the outward deflection of the diaphragm has been seen to cause a leak around the diaphragm to the vented sleeve, thereby venting the water reservoir to atmosphere;

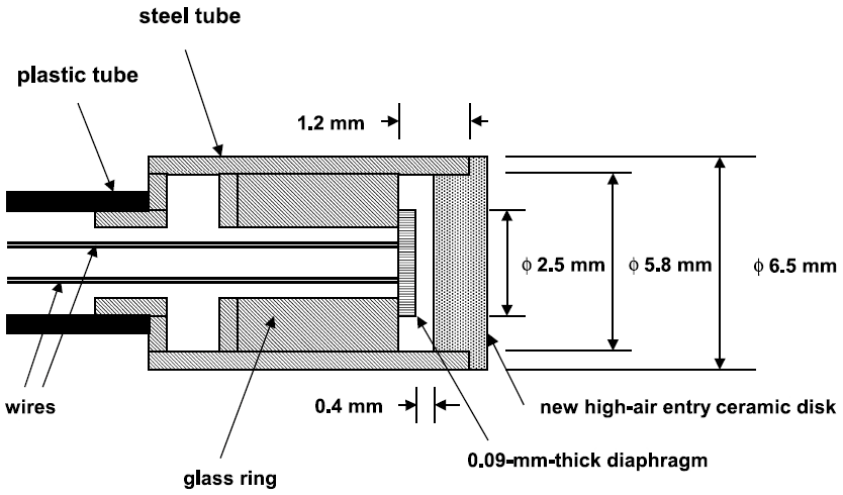

Figure 5.8. . Schematic diagram of the modified transducer PDCR81 (Meilani et al. 2002).

- small holes in the vented sleeving of the device, although watertight under working pressures, are susceptible to water entry under the high water pressures associated with the second phase of filter saturation.
- there is considerable risk associated with both the initial sealing operation (excess epoxy bonding the diaphragm to the filter), and the subsequent extraction of a porous filter for replacement.

According to Marinho and Chandler (1994) if the requirements listed in section XXX are followed carefully, it is possible to use an ordinary high pressure transducer to measure soil water suction, and a special design of tensiometer probe with low water volume is not required. As a matter of fact, they performed some successfully suction measurement test by using a Keller PR-27-100 (Figure 5.2b) transducer in conjunction with a 15 bar air entry ceramic disk. Nevertheless, Marinho and Pinto (1997) have pointed out that although it is possible to use an ordinary tensiometer, properly conditioned, the internal volume of water associated with the internal surface area of the tensiometer increase the likelihood of cavitation inside the tensiometer. In addition, Tarantino and Mongiovì (2003) suggested that cavitation takes place in the porous ceramic rather than the water reservoir. Thus, the size of the water reservoir would not be a critical factor. This subject was also covered by Ridley and Burland (1999). In this context the authors refer that the original version of the Imperial College tensiometer (Ridley and Burland 1993) (Figure 5.3) was very good at making quick measurements of soil suction up to about 1500 kPa, however, it was less successful for making long term measurements, and accompanied by tension break down in an apparently random manner.

5.2.2 *Integral strain-gauge tensiometer*

The alternative to commercial transducer as system to measure pressure changes on suction probes is the integral strain-gauge. The first tensiometer of this type (Figure 5.1) was proposed by Ridley and Burland (1996). This version of the Imperial College probe is an alternative to the previous probe based on a commercial transducer (Ridley and Burland 1993), which presents problems (i.e. random tension break down) when long term suction measurements were carried out. The authors associate the problems of the early version of the probe with the relatively large volume of water in the reservoir and regions where air can easily become trapped. Then, the integral strain-gauge tensiometer was designed with a water reservoir of a reduced size (approximately 3 mm^3). This reduction in reservoir volume was motivated by the crevice model of tension breakdown (Ridley et al., 1998). A smaller reservoir will have a smaller number of imperfections and be statistically less likely to suffer from unpredictable tension breakdowns.

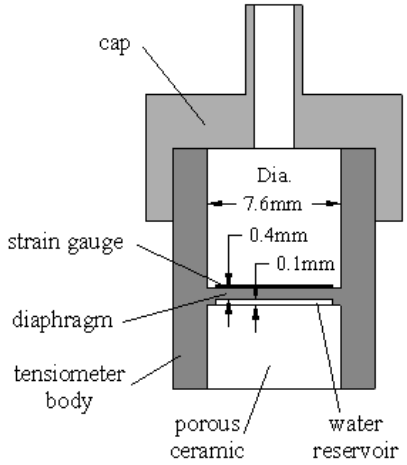

Figure 5.9. Trento tensiometer (Tarantino & Mongiovì 2002).

Another tensiometer equipped with an integral strain-gauge has been presented by Tarantino & Mongiovì 2002 (Figure 5.9). This design is very similar to the IC tensiometer, the top section of the tensiometer was prolonged so as the diaphragm is positioned at midheight of the stainless steel body. This is the unique probe which allows direct calibration in the negative range. Its performance was found to be very similar to the IC tensiometer.

Delage et al. 2008 have noted that integral strain-gauged diaphragms and epoxy resins assembled probes reached the maximum sustained tension, exceeding the nominal AEV of the ceramic disk.

5.3 STRAIN-GAUGED DIAPHRAGMS

In order to help with the understanding of terms and concepts involved in the design of strain gauged diaphragms, a definitions review and design considerations are presented below.

5.3.1 *Wheatstone bridge*

To make an accurate strain measurement, extremely small resistance changes must be measured. The Wheatstone bridge is a basic electrical bridge circuit widely used to convert the gauge's micro-strain into a voltage change that can be fed to the input of the ADC. In the circuits shown in Figure 5.10a, the bridge can be imagined as two ballast circuits, composed of R_1, R_2 and R_3, R_4, connected so that the initial steady state voltages are cancelled in the measurement of the output voltage (E_o).

The ballast circuit is a simple system used to make measurements of resistance. It consists of a simple voltage source and a gauge placed in series with a ballast resistor, making the voltage source resemble a constant current source. If the input current (E) is known and forced through the unknown resistance, and according to Ohm's Law the resulting voltage drop across it is directly proportional to the resistance

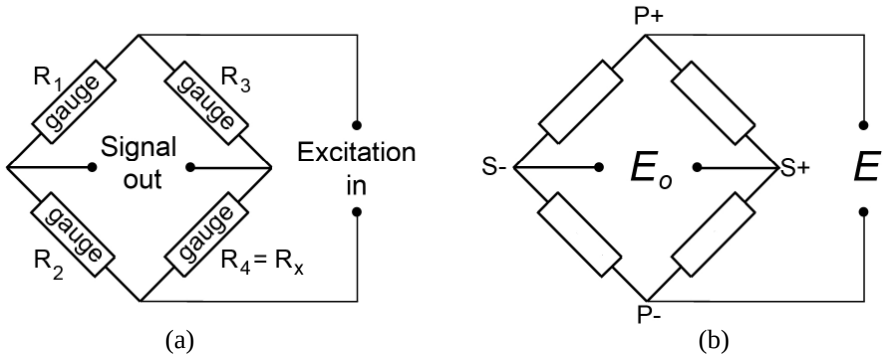

(a) (b)

Figure 5.10. Diagram of a) basic full-bridge circuit and b) undefined full bridge circuit.

In other words, if in the Wheatstone bridge in Figure 5.10a R_1, R_2 R_3 and R_4 are resistors of known resistance subject to the voltage flow (E), the output voltage E_o can be obtained as the difference between two ballast circuits:

$$E_{ov} = \frac{R_2}{R_1 + R_2} E - \frac{R_4}{R_3 + R_4} E = \frac{R_2 R_3 - R_1 R_4}{(R_1 + R_2)(R_4 + R_3)} \tag{5.1}$$

When the bridge arms are symmetrical, as mentioned before, the initial steady state voltage (E_o) is cancelled (i.e. E_{ov} = 0). Such a configuration with zero output of

balance voltage is termed a “Balanced Bridge”. It is provided when the numerator in the last term of the Equation (5.1) is zero

$$R_2R_3 = R_1R_4 \tag{5.2}$$

When any of the resistors in such a system is strained, its resistance R_j will change by fractional amount and the bridge produces a significant out of balance in the voltage (i.e. $E_o \neq E$). This is the basic idea of strain gauged diaphragms. As a matter f fact, if Wheatstone bridge is firmly glutted to a deformable membrane (as for example Figure 5.9), any deformation of the membrane will result in a deformation of the resistor, in a consequent change of its R_j, and in a difference between E and E_{ov}. The resistance change (R_j) is related to the strain by the quantity known as the gauge factor (GF), and represents the measure of the sensitivity of the resistor:

$$GF = \frac{dR/R}{\varepsilon} \tag{5.3}$$

where: R is the resistance of the undeformed gauge, dR is the change in resistance caused by strain, and ε is the strain[1].

Considering infinitesimal changes in each resistor (i.e. $R_i \Rightarrow R_i + dR_i$) the differential change in E_o can be compute as:

$$E_o = E_{ov} + dE_o = \frac{R_2R_3 - R_1R_4}{(R_1 + R_2)(R_3 + R_4)}E + \frac{GF}{4}(\varepsilon_1 - \varepsilon_2 + \varepsilon_3 - \varepsilon_4)E \tag{5.4}$$

where: ε_i is the strain in the gauge placed in the i-th arm of the bridge. If the bridge is initially balanced (i.e. $E_{ov} = 0$), the Equation 5.4 can be represented by the Equation 5.5, which is the basic equation relating the Wheatstone bridge output voltage to strain in each gauge.

$$E_o = \frac{GF}{4}(\varepsilon_1 - \varepsilon_2 + \varepsilon_3 - \varepsilon_4)E \tag{5.5}$$

The real arms are “nominally” resistively symmetrical about an axis joining the output corners of the bridge and their “balanced” condition is expressed in the following relation:

$$\frac{R_1}{R_2} = \frac{R_3}{R_4} = 1 \tag{5.6}$$

If the “balanced” condition is not to be applicable, as the strain gauges are strained the voltage output of the bridge won’t be proportional to the resistance changes, but

[1] The strain units are the microstrains (με) (e.g. 10 000με = 1% of gauge deformation)

nonlinear with strain, and the Wheatstone bridge is operated in a resistively "unbalanced" state.

The unbalance state may be increased if the resistance of strain gauge is altered significantly from the manufactured value, as can be occurs by:

- poor installation technique during the bonding of the strain gauge,
- assembly or preload stresses before subsequent strain measurements are to be made.

The magnitudes of initial resistive unbalance should be measured and properly accounted for in making nonlinearity corrections. However, for some instruments the nonlinearity errors will have to be determined by direct calibration; for instance, the strain gages installed on a transducer have been readily calibrated against a previously calibrated transducer.

5.3.2 *Design considerations*

One of the most important elements in the suction probe is the strain-gauged diaphragm, which should be designed so that the yield point of the material being used is not exceeded when the greatest anticipated overload occurs, but deformable enough to obtain an adequate sensitivity to suction changes. It is assumed that the strain gauge is so thin that its mechanical effect on the diaphragm can be neglected and that the strain of the strain gauge is the same as the strain of the diaphragm.

The accuracy and hysteresis of the diaphragm are dependant on his geometry, its boundary conditions and the kind of applied load. Typically, a thick diaphragm[2] clamped at their circumference is used, rather built as an integral part of the transducer body.

The strain distribution in a rigidly clamped diaphragm under uniform pressure distribution is shown in Figure 5.11.

At the centre of the diaphragm, the radial and tangential strains are identical, and reach their maximum positive value, expressed by the following equation:

$$\varepsilon_R = \varepsilon_T = \frac{3PR_o^2\left(1-\nu_d^2\right)}{8t^2E_d} \tag{5.7}$$

where E_d = Elasticity modulus of the diaphragm.

[2] A thick diaphragm is defined by a small centre deflection compared to its thickness.

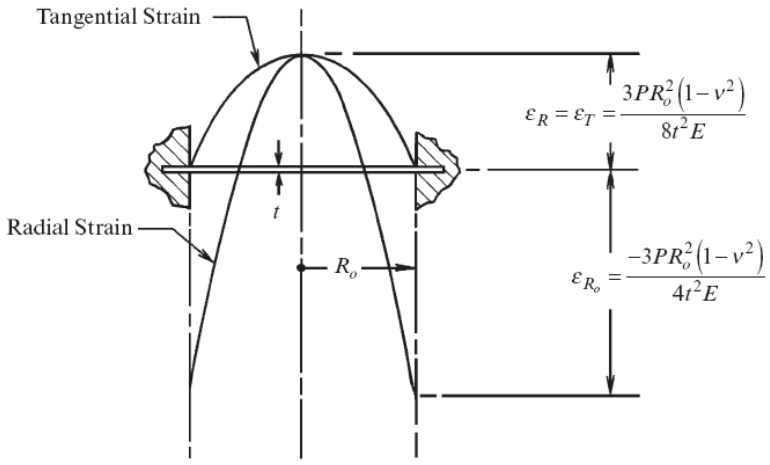

Figure 5.11. Strain distribution in clamped diaphragm (Vishay® 2005a).

At the periphery, the tangential strain decreases to zero, while the radial strain becomes negative, and equal to twice the centre strain.

To calculate the resistance change of strain gauges clamped to a diaphragm deflected as described above, the effect of straining on resistors need to be known. The highest predictable sensitivity occurs at the rim of a diaphragm, where the radial strains are maximum (in absolute value) and the resistance change associated to the resistor deformation reaches is the strongest function of radial position and orientation towards the centre; and the alignment in the centre is quite uncritical (Schomburg et al. 2004).

It is necessary to cover a considerable area of a micro diaphragm with strain gauges. Radial strain gauges next to the rim and tangential strain gauges (i.e. spiral grid) adjacent to the radial ones promise to generate the highest sensitivity when combined in a Wheatstone bridge; this results in a rosette-like design (Schomburg et al. 2004).

A Wheatstone bridge designed according to the previous consideration is that in Figure 5.12a. Taking account of the sign difference in the strains sensed by the radial and tangential grid elements, and dividing the elements into symmetrical pairs, permits incorporating a full bridge into a single strain gage. Another advantage is the solder tabs setting, it's have been located in a region of low strain.

Since, the strains are maximum on the surface of the diaphragm, practical design considerations dictate that the strain gauge should be mounted next to the surface and not embedded into the diaphragm. This produces the maximum allowable signal output consistent with the strength of the spring element material.

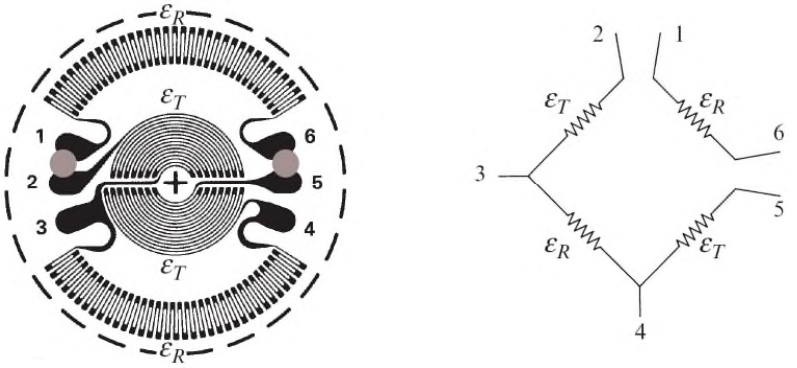

Figure 5.12. Circular strain gauge for pressure transducers. a) diaphragm b) internal circuit (modified from Vishay® 2005a).

To illustrate the position of the grid elements on a strain-gauged diaphragm, when used a circular pattern, a structural simplification of the strain-gauged diaphragm is represented on Figure 5.13. The Figure 5.13 also includes the deflection diagram, with the deflection greatly exaggerated for clarity. Grid elements positions are sketches by short line segments labelled T and C for tension and compression, respectively.

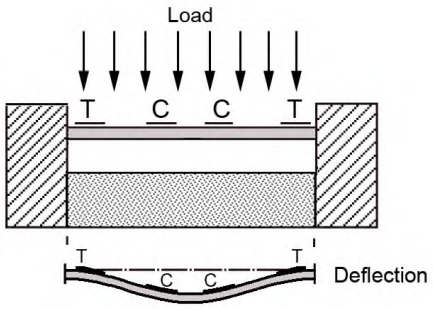

Figure 5.13. Grid elements position of a circular pattern on a strain-gauged diaphragm.

According to Equation 5.5, the sensitivity of strain-gauged diaphragms is expressed by the output current E_o. According Vishay® (2005a), for a circular pattern, averaging the strain over the region covered by each sensing element (assuming a gage factor of 2.0), and averaging the outputs of all sensing elements, E_o in millivolts per volt (mV/V) of supply volt can be expressed approximately by the expression:

$$E_o = \frac{3PR_o^2\left(1-\nu_d^2\right)}{4t^2E_d}\times 10^3 \tag{5.8}$$

5.4 DESIGN OF THE UNINA SUCTION PROBE – INTEGRAL STRAIN-GAUGED

A high capacity tensiometer has been developed at University of Napoli Federico II using a design layout similar to that initially propose by Ridley & Burland (1995) (i.e. a integral strain-gauged tensiometer), but including some variants to allow the substitution of HAEV disk without changing the hole probe. This measure has been adopted in order to easily tune the measurement capacity of the tensiometer and its time-response to any particular application under study.

The UNINA probe (Figure 5.14), utilizes a circular clamped-edge diaphragm. The strain-gauged diaphragm is 6 mm in diameter and 0.4 mm in height. As suggested in section 5.3.2, the strain gauge has a rosette-like design with the radial strain gauges next to the rim and tangential strain gauges adjacent to the radial ones, generating the highest sensitivity when combined in a Wheatstone bridge. The circular trim diameter of the strain gauge covers a considerable area of the micro diaphragm. To produce the maximum allowable output signal the strain gauge is bonded to the non-pressurized side of the diaphragm.

The novel piece is an interchangeable filter cap containing a HAEV ceramic disk of 7.4 mm in diameter and 6.0 mm in height. The operating range is determined by the filter's AEV (i.e. 5 or 15 bar), allowing to a single unit to operate in different suction ranges by changing filter. The water reservoir between the ceramic disk and the strain-gauged diaphragm has an approximate volume of 3 mm^3.

Two are the stainless steel housings (Figure 5.14), one to hold the diaphragm, and the another one to provide a support and isolating of an electrical connectors. A vented waterproof sheating ensures the atmospheric pressure in the back of the strain-gauged diaphragm and isolates the electronic parts from water and dust.

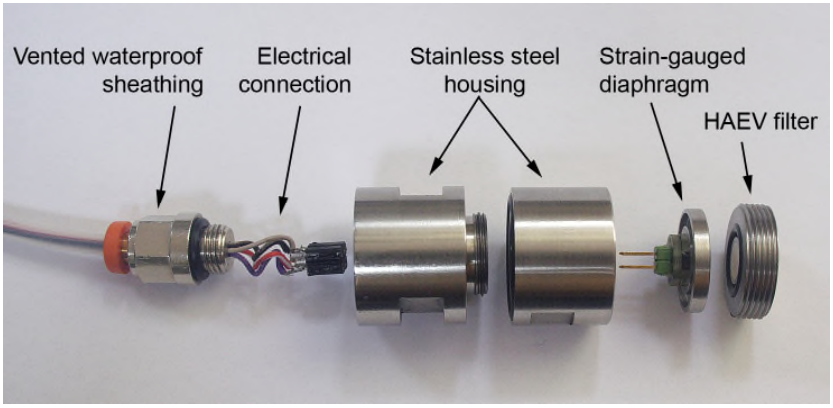

Figure 5.14. UNINA high capacity tensiometer.

The strain-gauge measurements are acquired through a bridge amplifier static strain indicator and stored in a digital data logger (Figure 5.15a). The recorded data (i.e. up to 1 per second of observation) are stored on a memory card and transferred by an USB port to a PC. The strain gauge is connected to the acquisition system through appropriate input terminals. An undefined full-bridge circuit is used as input (Figure 5.12b and Figure 5.15b) selected on the basis of the net output of the active strain gages without mathematical correction for either bridge configuration or nonlinearity applied. Operating in this way, the nonlinearity errors will have to be determined by direct calibration against a previously calibrated transducer. Table 5.2 shown the design parameters characterizing the UNINA probe, it were determined assuming 2000 kPa as the maximum pre-pressurization pressure. The maximum radial strains in the diaphragm are well-suited with the reference of the strain gauge manufacturer (i.e. > -2×10^{-3}). The maximum expected deflection is very little compared whit the water reservoir depth (0.1 mm), then, the design ensures the free deformation of the diaphragm. Also, the maximum radial stress remains below the yielding stress for the stainless steel.

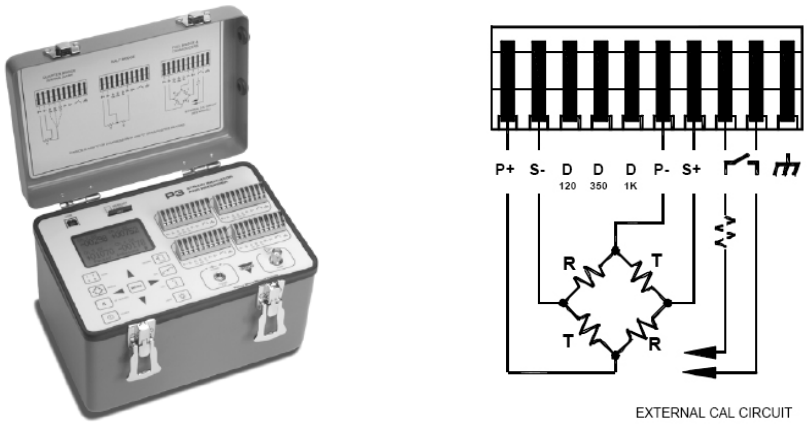

(a) (b)

Figure 5.15. a)Vishay P3 strain indicator and recorder; b) Full-bridge connection.

Table 5.2. Characteristics corresponding to a maximum applied pressure of 2000 kPa

Parameter	Symbol	Critical magnitude	Units
Radial strain ‡	ε_R	-3.8×10^{-4}	-
Total gage output	E_o	0.125	mV/V
Sensitivity§	-	0.28	μV/kPa
Deflection	Y_c	2.1×10^{-3}	mm
Radial stress ‡	σ_R	54210	kPa

‡ at the periphery of the diaphragm; § energy supply 1.5 V.

5.5 DESIGN OF THE UNINA SUCTION PROBE – COMMERCIAL TRANSDUCER BASED

The design of the probe based on a commercial transducer is addressed to provide a probe for pore-water pressure monitoring during suction controlled tests. That means an airtight sensor capable to read pore-water pressure variations with a minimum of lag.

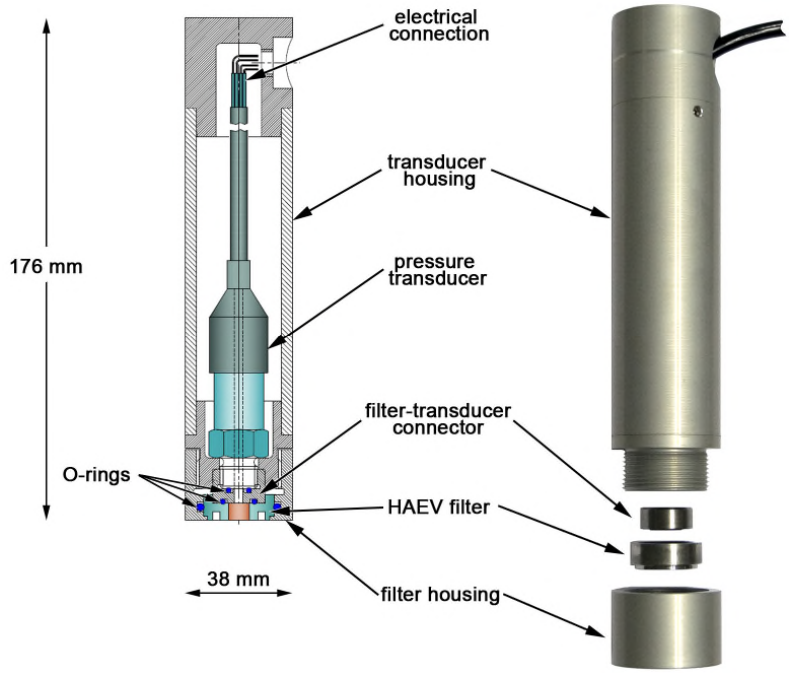

Figure 5.16. Pressure transducer based probe.

Basically, the probe has been obtained by fitting a HAEV ceramic disk to a commercial transducer (Figure 5.16). The probe utilizes a Druck PDCR 810 pressure transducer (Figure 5.2a), with a rated limit of 1000 kPa and accuracy of 0.1 % (i.e. 1 kPa). The novel piece is a removable HAEV filter containing a 500 kPa AEV ceramic disk of 7.4 mm in diameter and 6.0 mm in height. Two stainless steel housings are used (Figure 5.16), one to hold the transducer, and the another one to provide a support to HAEV filter. A filter-transducer connector is used to join the pressure transducer and the filter housing. Rubber O-rings, one in each side of the filter-transducer connector and a third one between filter housing and HAVE filter, act as sealants. The parts are fixed by driven the filter housing into the transducer housing.

The strain gauge of the transducer is connected to the acquisition system through a removable connector. The cable of transducer wherein electrical contact comprises one pair of insulated electrical wires for providing electrical power to pressure transducer and one pair of insulated electrical wires for receiving electrical signals from pressure transducer. A detail of the connection between the removable connector and the cables of the transducer is shown in Figure 5.17. The probe measurements are acquired through a bridge amplifier static strain indicator and stored in a personal computer. Inside the cable the pressure transducer contains an air vent tube for providing a pressure differential relationship between the applied pressure and the atmosphere. During mounting process, is important to ensure no damage occurs to the cable as cable damage represents the most frequent cause of transducer failure. Good cables are quite flexible and care needs to be taken when bending the cable to do not crimp the vent tube inside. Is recommended do not bend the cable tighter than a 2.5 cm radius.

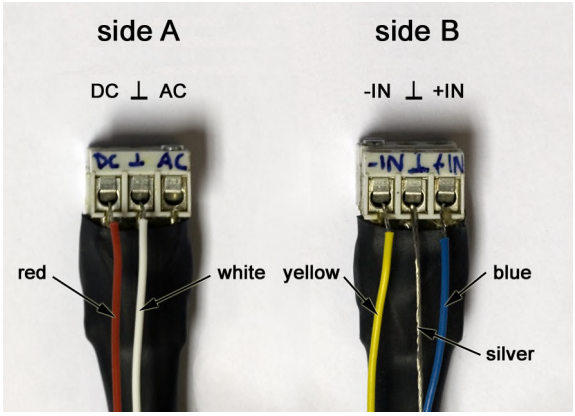

Figure 5.17. Connector detail.

The gap between the HAEV filter and the transducer's diaphragm was made as small as possible to obtain a fast response and sensitivity of the pore-water pressure measurement. The gap also named water reservoir is the space comprised of the transducer chamber (i.e. in front of the diaphragm, volume = 0.5 cm^3) and the inner hole present in the filter-transducer connector (volume = 0.035 cm^3). The water reservoir volume corresponds to almost 100 times the average volume used in most of the suction probes described in literature.

5.6 PROBES SATURATION

The water reservoir and the voids of the HAEV ceramic disk must be filled with deaired and demiralized water to give a continuous water phase between the pore water of samples and the pressure transducer.

To obtain a good response of a tensiometer is clear that the design plays an important role. Equally clear is that the design of an appropriate saturation device and procedures is also critical. In particular, Guan & Fredlund (1999) suggested that there is a cavitation tension for a particular pre-pressurization procedure and a particular suction probe. Ridley & Burland (1999) found, on the contrary, that for a thoroughly saturated suction probe the stress required to cause a tension breakdown in the reservoir water is uniquely related to the AEV of the filter.

Table 5.3 summarizes information on the characteristics of saturation processes used by the various authors. The relevant characteristics of saturation procedure are: the initial condition of the HAEV porous disk (i.e. dry or saturated) at assembly time, if vacuum is used during the flooding process, the pre-pressurization pressure and the loading unloading cycles.

Table 5.3. Data of saturation process used in previous studies.

Tensiometer	Filter AEV (bar)	Assembly	Vacuum saturation	Pre-pressurization pressure (kPa)	Pre-pressurization cycles
Ridley & Burland (1996)	15	dry	yes (60 min)	4000 (24 h)	no
Guan & Fredlund (1997)	15	under water	no	12000 (1 h)	yes (6 cycles)
Tarantino & Mongiovì (2002)	15	dry	yes	4000 (24 h)	no
Meilani et al. (2002)	5	dry	no	800 (4 days)	no
Take and Bolton (2003)	3	oven dried	yes (20 min)	1000 (1 h)	yes
Chiu et al. (2005)	5	dry	yes (60 min)	700 (24 h)	no
He et al. (2006)	5	dry /sat	no	2000 (1 month)	no
Lourenço et al. (2006)	15	dry	yes	800 (72 h)	no
Mahler & Diene (2007)	5, 15	dry	yes (15 h)	> than filter AEV	yes

According to crevice model (see section 5.7.3), Tarantino & Mongiovì (2001) observed that saturation of the ceramic filter is achieved mainly through cycles of cavitation and subsequent pressurization, and that an inadequate initial saturation simply increases the number of cycles required to obtain a satisfactory performance of the probe. Contrarily, Guan & Fredlund (1999) indicated that repeated cavitation of the sensor appeared to reduce the maximum sustainable tension. Finally, Chiu et al. (2005) and Lourenço et al. (2006) show unclear evidence to support the hypothesis of an increase of cavitation suction with cycles of cavitation and pressurization. In summary, after Marinho & Chandler (1994), the main requirements to avoid cavitation in the measurement system and improve the ability to measure negative water pressure seems to be: a) the water and all surfaces within the

measurement system must be pure and clean (Henderson & Speedy 1980), b) the surfaces in contact with the water system must be as smooth as possible to avoid or reduce the number and the size of the crevices, c) the system should be air-evacuated by vacuum application prior to the pre-pressurization in order to remove the maximum amount of air entrapped into the crevices (Jones et al. 1981), d) pre-pressurization of the sys-tem to high pressure is required in order to dissolve all the free air (Harvey et al. 1944), e) the HAEV disk must be brought to a low initial moisture content prior to the application of initial saturation, as this has been demonstrated a crucial factor for the saturation of the disk itself (Take & Bolton 2003). All these factors should be considered in the design of a saturation device and the saturation procedure adopted for any probe.

To understand the saturation steps defined in previous works and to establish a proper saturation process for the designed probes is necessary to review concepts from physics involved in the cavitation process, like water phase change, nucleation and cavitation itself. A recall of these definitions is presented in the next section.

5.7 WATER PHASE CHANGE, NUCLEATION AND CAVITATION

When water is depressed below its saturated vapour pressure (P_{sat}), it is expected to transform into vapor, which is more stable. This transformation is also called cavitation. However, if care is taken to use a very pure water in a very clean chamber, with smooth and hydrophilic walls, cavitation may occur only far beyond the line of thermodynamical equilibrium; in such systems, the pressure may even be negative, which means that the liquid is subjected to a mechanical tension.

Then, the water can sustain tension (negative pressure). At such a negative pressure, a liquid cannot be in equilibrium but it can stay metastable for a very long time.

5.7.1 *Water phases*

The solid, liquid, and gaseous phases of a substance are stable only over a certain range of temperatures and pressures. In dealing with the behaviour of a fluid near liquid-vapor phase transition, the equation of state proposed by van der Waals (Eq. is quite satisfactory in describing many aspects of the observed behaviour.

$$\left(P + \frac{a}{V_m^2}\right)\left(V_m - b\right) = RT \tag{5.9}$$

where P is the pressure, V_m is the molar volume, and a and b are two coefficients characteristic of the substance under study. The parameter a reflects the long-range attractive interactions (van der Waals forces) while the parameter b reflects the short-range repulsive ones. Although, this equation is not useful to describe quantitatively most liquid/vapor systems, the phase diagrams and stability lines calculated from it are topologically correct (Imre 2007). The van der Waals equation can describe not only gases but liquids states too, also predicting the existence of critical and supercritical states.

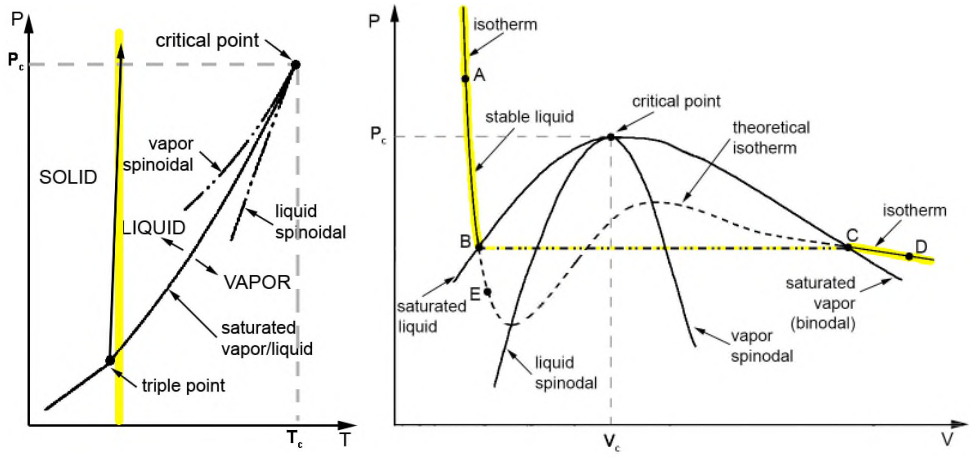

Figure 5.18. Typical phase diagrams (Brennen 1995).

Figure 5.18a shows a typical state diagram, indicating the P and T values characterizing the phase transitions under equilibrium conditions, as the continuous lines separating the solid, liquid and vapor states. The solid, liquid, and vapor phases can coexist in equilibrium only at the triple point. In any different position on the solid lines, only two phases can coexist: the solid and the liquid along the fusion curve, and the liquid and the vapor along the vaporization curve (saturated vapor/liquid line). The top limit of the saturated liquid/vapour line is the critical point where liquid and vapor assume the same characters. Above the critical point a fluid is termed supercritical. No phase transition is possible at pressure and temperature above the critical point: the liquid state is not achievable and the gas possesses some properties similar to a liquid (e.g. the density) and some analogous to a gas (e.g. its viscosity).

Figure 5.18b represents a generic at $T < T_0$ isotherm in a space pressure against volume like that highlighted in Figure 5.18a. The line linking the critical point and the maxima in the theoretical isotherms is called the vapor spinodal line; the line

joining the minima is called the liquid spinodal line (both of them represented on Figure 5.18a too). The vapour spinodal marks the border where a supersaturated vapour can not exist any more; it has to condensate partly or fully into a liquid phase. The liquid spinodal marks the border where a liquid can not be overheated or stretched any more, it has to form vapour phase. The isotherm crossed three times by the line. The middle crossing point does not have physical meaning. Points B and C gives the stable liquid state and the stable gas phase, respectively.

In the saturated vapor/liquid line one of the two coexisting phases can be obtained from the other by isothermal volumetric changes, leading through intermediate but unstable states. Brennen (1995) presented a theoretical example of the possible paths that a pure liquid (point A on Figure 5.18b) can follow if pressure is reduced below the saturated vapor pressure (point B) at constant temperature:

- If sufficient numbers of “nucleation sites” of sufficient size are present the liquid will become vapor as the state moves horizontally from B to C, and at pressure below the vapor pressure the state will come to equilibrium in the gaseous region at a point such as D.
- If no nucleation sites are present, the depressurization may lead to continuation of the state down the theoretical isotherm to a point such as E, called a “metastable[3] state” since imperfections may lead to instability and transition to the point D.

The pressure difference between B and E represents the magnitude of the tension at point E.

Figure 5.19 represents the schematic phase diagram of the fluid water. The state boundary lines are: the equilibrium lines (borders between stable and metastable states) and the stability lines (borders between metastable and unstable states). Is interested remark that P = 0 line is neither an equilibrium nor a stability line for liquids.

Theoretically water can survive tension values in the range of -200 MPa and -400 MPa. In 1850 Berthelot subjected pure water to a pressure of -5 MPa, at this time a record on liquids tension measurements. The deepest tension reached in water up to now, measured by Imre (2002), is around –200 MPa.

The liquid-gas transition is discontinuous. An interface between a liquid and its vapour phase, with a non-zero surface tension, exist. There is an energy barrier

[3] Metastability is the ability of a non-equilibrium state to persist for a long period of time; unless sufficiently disturbed to pass to a more stable state of equilibrium. However, metastable states may be easily stimulated to become unstable.

against the nucleation of the stable phase. As a result, metastability is possible. However, a liquid at constant temperature and under a metastable state could suffer a rupture in pressure. The process of rupturing is often called cavitation.

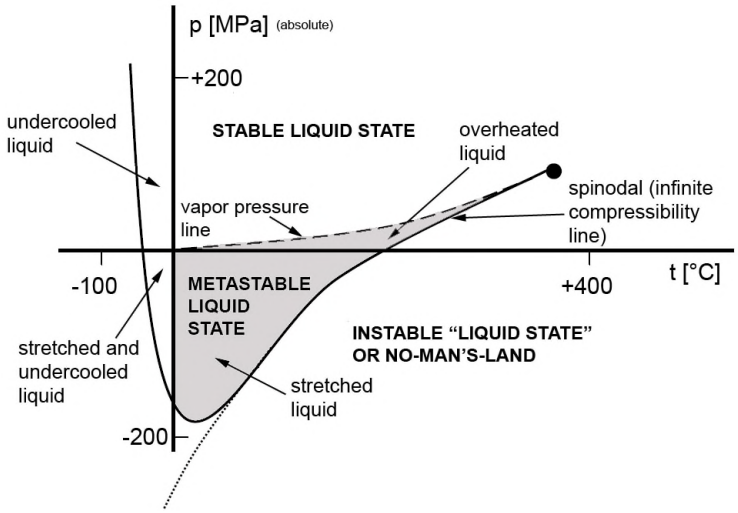

Figure 5.19. Schematic phase diagram of fluid water with two type of liquid–vapour stability line (Imre 2007).

5.7.2 *Nucleation*

Nucleation is a non-equilibrium process. This process brings a system that is out of equilibrium to a new equilibrium. In other words, nucleation is the process of phase transition by heterogeneous density fluctuations (i.e. cluster[4] formation). The phase transition can be the formation of a bubble or of a crystal from a liquid, if pressure or temperature is decreased, respectively. In advance, only the nucleation caused by transition from liquid to vapour will be considered.

Nucleation normally occurs at nucleation sites on surfaces containing the liquid. Heterogeneous nucleation involves the formation of a cluster on a substrate, in contrast to homogeneous nucleation, which involves the formation of a cluster in the parent phase. The heterogeneous nucleation is influenced by the presence inhomogeneities. These inhomogeneities, be they free bubbles, dirt particles, clusters

[4] In physics, the term clusters denotes aggregates of a small and finite number of atoms or molecules. They range from the dimer, consisting of only two atoms, up to large clusters made up of several tens of thousands of atoms. In this sense clusters bridge the gap between the isolated atom and the infinite solid.

of organic, or ionic molecules, or due to a cosmic ray or other form of radiation, have been given the generic name of cavitation nuclei. In the absence of the mentioned causal, nucleation is an intrinsic property of the system caused by thermal motions within the liquid that form temporary, microscopic voids (clusters) that can generates the called homogeneous nucleation, it usually takes place very far from equilibrium conditions. In nature and technical applications heterogeneous nucleation is more commonly encountered than homogeneous nucleation.

In water, another important form of weakness are microbubbles of gas, which could be present in crevices within the solid boundary or within suspended particles or could be simply be freely suspended within the liquid (Brennen 1995). In water, microbubbles of air seem to persist almost indefinitely and are almost impossible to remove completely.

5.7.3 *Gas trapping crevice model*

In general, cavitation nuclei are long lived and are comprised at least in part by a volume of gas. Thus, the nucleating bubble is treated as a sphere filled with vapour, separated from the metastable liquid by abrupt walls. Free bubbles will quickly dissolve in liquids that are not supersaturated with gas, and bubbles having radii of less than a critical value will dissolve even in a supersaturate liquid. Bubbles of larger than critical radius will grow in a supersaturated liquid. In either case, free bubbles are unstable and the liquid will soon be free of them. The nucleation model explains the instability theory of cavitation nuclei. One of the most successful nucleation models is the gas-trapping crevice model (Harvey et a1 1944, Apfel 1970, Winterton 1977).

Henry's Law establishes that the pressure of the gas above a solution (P_g) is proportional to the concentration of the gas in the solution:

$$c = K(T)P_g \tag{5.10}$$

where: c is the molar concentration of the gas, and $K(T)$ is the Henry's law constant, function of temperature.

Regarding a chamber partially filled with liquid (Figure 5.20). The left over space contains vapor and gas at pressure, P_v and P_g, respectively. Then, neglecting hydrostatic effect, the pressure in the liquid (P_L) are equal to the total pressure above the liquid:

$$P_L = P_v + P \tag{5.11}$$

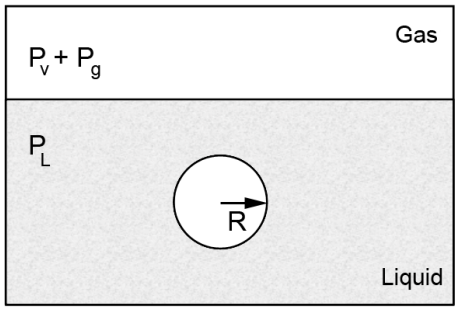

Figure 5.20. Diagram of a chamber partially filled with a liquid (Atchley and Prosperetti 1989).

The gas concentration at liquid saturation (c_s) is obtained substituing Eq. 5.11 into Eq. 5.10:

$$c_s = K(T)(P_L - P_v) \tag{5.12}$$

If a free bubble is present in the liquid, the pressure inside it is equal to P_g.

In the steady state the Laplace equation describes the effect of surface tension on a bubble as:

$$P_v + P_g = P_L + \frac{2\sigma_{gL}}{R} \tag{5.13}$$

where: σ_{gL} is the gas-liquid interface surface tension and R is the interface radius of curvature. R is considered positive when the radius of curvature lies on the gas side of the interface, as represented in Figure 5.20. Then, for a bubble to be stable under increased pressure the surface tension term ($2\sigma/R$) needs to be negative, this can only occur if R is negative. For a spherical bubble this is impossible.

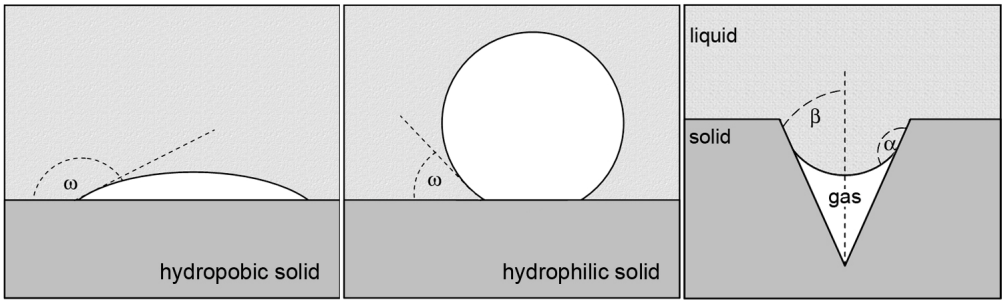

Figure 5.21. Modes of heterogeneous nucleation. a) flat hydrophobic surface; b) flat hydrophilic surface; c) conical crevice.

Another possible condition is a bubble in contact with a flat hydrophobic or hydrophilic surface (Figure 5.21a, b). The external contact angle is denoted by ω. In the case of a flat hydrophobic surface ($\omega > \pi/2$) the tensile strength could be zero and for the flat hydrophilic surface ($\omega < \pi/2$) would cause heterogeneous nucleation and much reduced tensile strength (Brennen 1995).

Nevertheless, at the microscopic scale surfaces are not flat. For simplicity, a conical cavity is considered to take in account for the effects of the local surface geometry.

According to Apfel (1970), for gas trapped in a conical crevice with an apex angle of 2β (Figure 5.21c), the stability of the meniscus between gas and water is assured if:

$$\alpha_A \geq \alpha \geq \alpha_R \tag{5.14}$$

where: α the angle that the free surface forms with the solid ($\beta + \pi/2$); α_A is the advancing contact angle; and α_R the receding contact angle.

The nuclei behaviour depends on the crevice shape (β) and on the gas saturation degree of the liquid, as Table 5.4 shown.

A very important fact that Atchley and Prosperetti (1989) noted is the contact angle hysteresis. If the contact angle did not exhibit hysteresis (i.e. $\alpha_A = \alpha = \alpha_R$) only nuclei with a sharply shape (defined by Eq. 5.14) could be stable in a saturated liquid. The shape defined by Eq. 5.14 restricts the number of possible nuclei and consequently the cavitation events, in contrast with experimental observations. Thus, the mechanism responsible for contact angle hysteresis is valid also at submicrometer scale.

$$\beta = \alpha_R - \pi/2 = \alpha_A - \pi/2 \tag{5.15}$$

Table 5.4. Data of saturation process used in previous studies.

Relation	Unsaturated liquid	Saturated liquid	Supersaturated liquid
$\alpha = \beta + \pi/2$	A		
$\alpha_A < \beta + \pi/2$	B	B	A
$\alpha_R > \beta + \pi/2$			C

A - the interface must be flat; B - the interface moves towards the bottom up to dissolute the gas; C - the interface recede drawing gas from the solution into the nucleus, which evolve into a gas bubble.

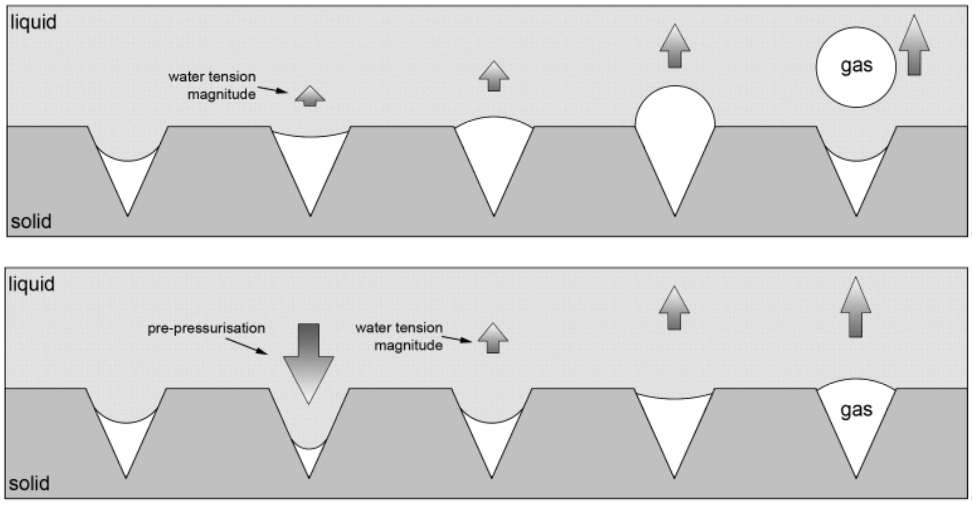

Figure 5.22. Crevice model of ceramic saturation (modified from Take and Bolton 2000).

The model crevice proposed by Harvey's et al. (1944) establish that after saturation of a water reservoir, a small volume of air remains trapped within minute crevices within the bounding surfaces of the water reservoir. The application of water tension will cause the volume of air to increase. This expansion will continue until bubble stability is lost, causing uncontrollable bubble expansion (i.e. cavitation) (Figure 5.22a)

Subjecting a liquid to high pressure (pre-pressurisation) inhibits the subsequent formation of cavities when tension is applied to the liquid. The value of α and the penetration of the liquid into the crevice depends on the past history of the system (Atchley and Prosperetti 1989). When the liquid is initially at atmospheric pressure an then progressively a pressure is applied, the liquid surface starts out as a plane and becomes more and more convex towards the gas. If the applied pressure increase, the whole interface starts moving deeper towards the apex of the crevice so as to make the curvature more negative, but always maintaining $\alpha = \alpha_A$. Upon restoring the atmospheric pressure the equilibrium is attained with $\alpha \leq \alpha_A$. Hence the crevice offers a mechanism by which a gas bubble may be stabilized against dissolution under tensions previously causing cavitation (Figure 5.22b).

5.7.4 *Other factors influencing cavitation*

With repeated cavitation the nuclei size decrease. When cavitation occurs the meniscus advances towards the bottom end of a crevice. Since the variations in P_L at cavitation are larger than those in P_g, the increasing trend reflects the fact that the

crevices are, on average, thin at the ends. The maximum negative pressure attainable with water contained in a metal Berthelot tube is raised with repeated cavitation (Ohde et al.1988).

Trevena (1989) summaries the experimental results reported in literature regarding time effects in cavitation experiments. The analysed data mainly concerns tension measurements applying Berthelot tube and dynamic stressing methods. Their conclusions can be outlined as:

- If the nucleation site is the solid surface, to a very rapid tension increase corresponds a lower breaking tension.
- When the cavitation starts in the body of the liquid itself, the breaking tension increases as the stressing rate increases.
- The longer the time of pressurization, greater the tension needed to cavitate the water afterwards.

The breaking tension increase steadily with each stressing until it levelled off at an upper limit.

5.8 SATURATION SYSTEM

Two different procedures were used to saturate the integral strain-gauged and the commercial transducer based tensiometers.

5.8.1 *Saturation method for the integral strain-gauged tensiometer*

As the saturation procedure of high capacity tensiometers has been demonstrated very important in literature, a conditioning system was designed to calibrate and pre-pressurize the integral strain-gauged tensiometer (Figure 5.23). The apparatus consists of two chambers (**c1** and **c2**), a vacuum generator (**g**), a manometer (**m**), two heaters (**h1** and **h2**), and five valves (**v1** - **v5**).

The tensiometer saturation process is performed as follows. Initially the valve **v1** is opened to drive distilled water into the chamber **c1**. The water is then de-aired keeping all the valves closed except valve **v2** and applying a positive pressure (**p1** = 600kPa) to vacuum generator **g**, this allow to impose a negative pressure (-95 kPa) in chamber **c1**. The water is de-aired for at least 3 h. The tensiometer **T** is then screwed into the chamber **c2**. To dry the tensiometer, the heaters **h1** and **h2** are switched on to reach a 70 °C constant temperature into chamber **c2**, and opening valve **v3** the atmospheric pressure is turned to a high vacuum; under this condition the water change from liquid to vapour phase. After the tensiometer has been left in this state for at least 16 h, the heaters are switched off, and valve **v5** is opened slowly

introducing water to the chamber **c2** (and porous filter) while under vacuum. Four hours after, the vacuum is released turning off the heaters and further time is allowed for saturation of the filter and water reservoir under atmospheric pressure. Valve **v2** is open, **v3** and **v5** are closed. In order to force any residual amount of air into solution, a pressure (**p2** = 800 kPa) is applied to the chamber **c2** for 72 h.

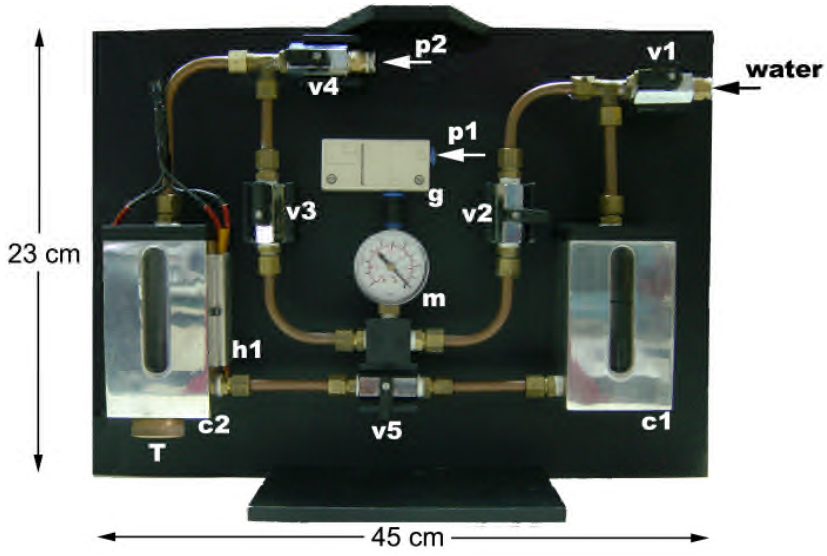

Figure 5.23. Saturation system.

The tensiometer is then calibrated in the chamber **c2** varying pressure **P2** from 0 to 800 kPa. The response of the miniature tensiometer during the loading unloading process (Figure 5.24) shows a linear response without appreciable hysteresis. The calibration curve in the negative pressure range was extrapolated from the calibrated positive range (Figure 5.24).

As Tarantino and Mongiovì (2002) observes, sensitivity resulting from calibration is not so different from the expected value, 0.25 μV/kPa and 0.28 μV/kPa, respectively.

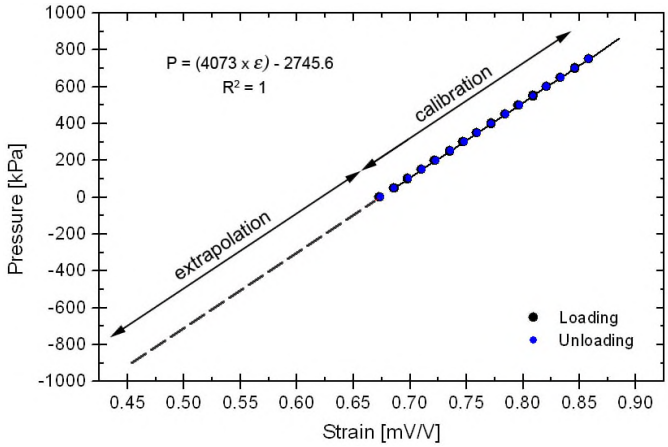

Figure 5.24. Tensiometer calibration curve.

5.8.2 *Saturation method for the commercial transducer based tensiometer*

The saturation process of the commercial transducer based probe was conducted in three stages: a) saturation of HAEV ceramic disk, b) saturation of the reservoir and c) prepresurization.

The procedure adopted to saturate the HAEV disk is the presented in the previous section.

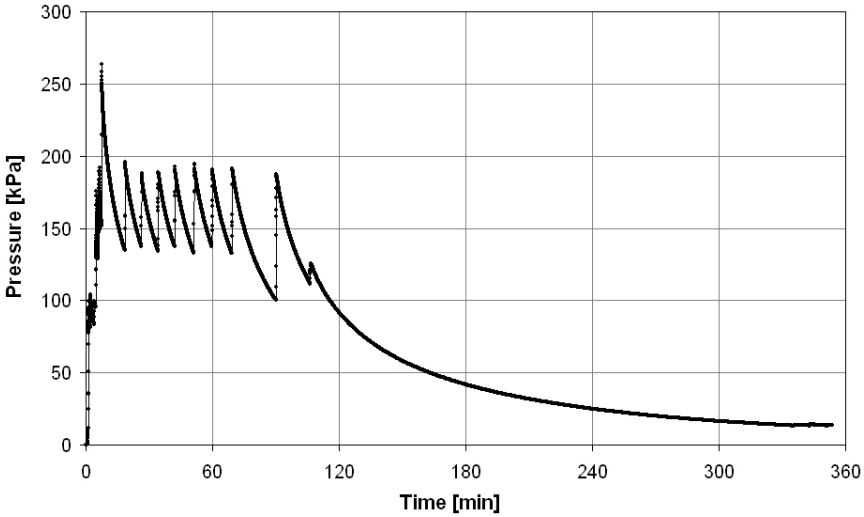

Figure 5.25. Tensiometer calibration curve.

As mentioned before, the water reservoir is the space comprised of the transducer and the HAEV filter. The transducer's chamber is saturated using a syringe. The syringe is charged with de-aired distilled water and the water should be inserted gently in the chamber, otherwise a big volume of air will remain.

Once the HAEV disk and transducer's chamber have been saturated, all the components are carefully assembled together under de-aired distilled water by screwing the transducer housing into the filter housing (Figure 5.16). During the screwing process, the pressure is monitored to control the rate of screwing in order to avoid an increment in the pressure higher than the rated limit of the transducer (i.e. 1000 kPa). Figure 5.25 presents the generated pressures during screwing process.

To increase the degree of saturation of the probe a programme of pressurization has been conducted. To not damage the pressure transducer the imposed pressure was limited to 725 kPa. In order to verify the saturation of the instrument after the pressurization period, sudden pressurization tests have been conducted. If the probe has achieved saturation (i.e., water reservoir totally filled with water) the probe should respond quickly to the applied pressure.

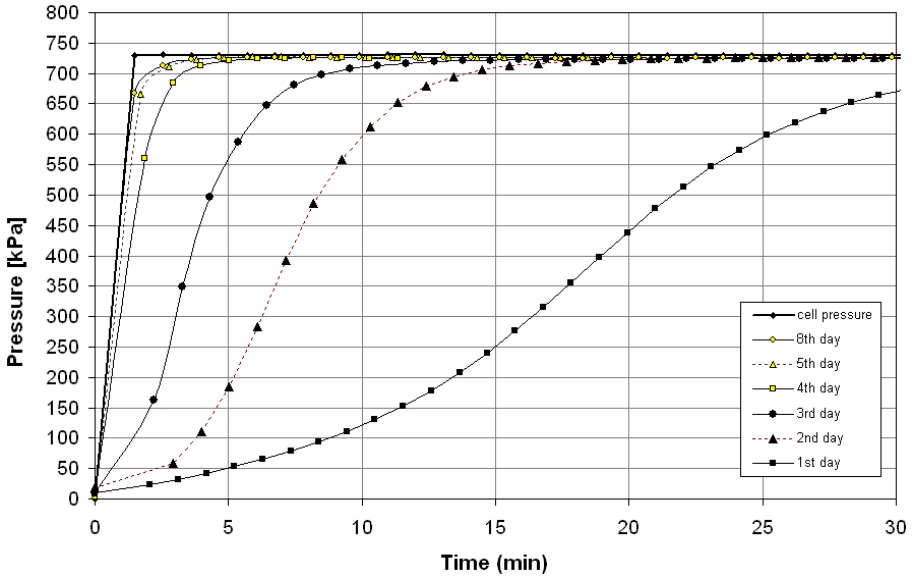

Figure 5.26. Prove response to pressure change.

The procedure was carried out by immersing the probe in the triaxial cell, which was previously filled with water up to its top. The pressure was imposed from the top-port hole. During the application of pressure, a pressure transducer attached to the triaxial cell gives the feedback information. A pressure higher than the ceramic's

AEV is applied (i.e. 725 kPa) during one day. After this period the pressure is released and when the readings of the prove are constant, the pressure in the cell is quickly increased (i.e. 725 kPa in 90 sec). The described procure is repeated until no significant improvements in probe's response is observed. The results of pressurization process are shown in Figure 5.26 and Table 5.5. From the Figure 5.26 it can be seen that an enhanced saturation of the system is achieved through cycles of pressurization; and the probe's performance improves up to reach an upper limit.

Table 5.5. Equilibration time.

Day	Equilibration time [min]
1st	180
2nd	20
3rd	15
4th	5
5th	3
8th	3

A drawback of this design is the big volume of the water reservoir, since as larger the volume the water reservoir holds, higher is the amount of water that must flow into or out of the probe in order to reach the equilibrium.

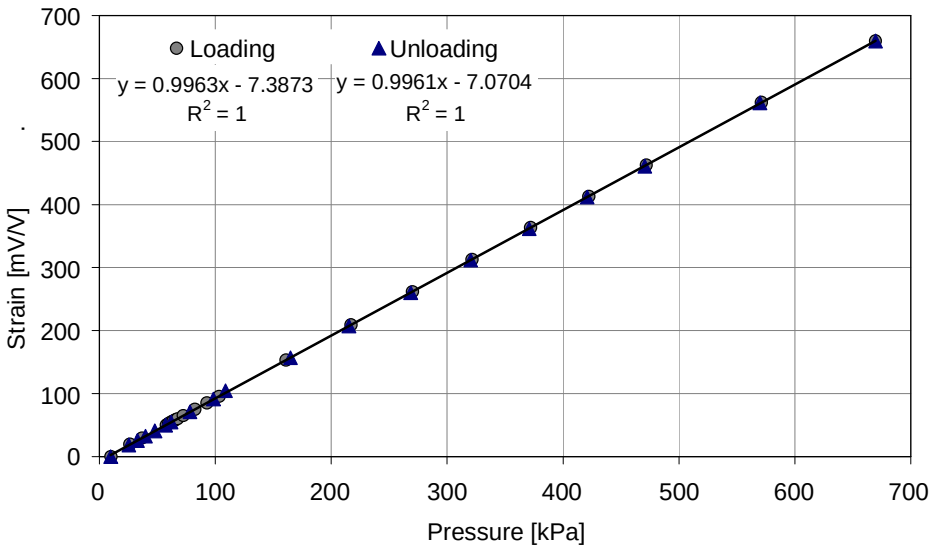

Figure 5.27. Calibration of the transducer Druck PDCR810 by using air pressure.

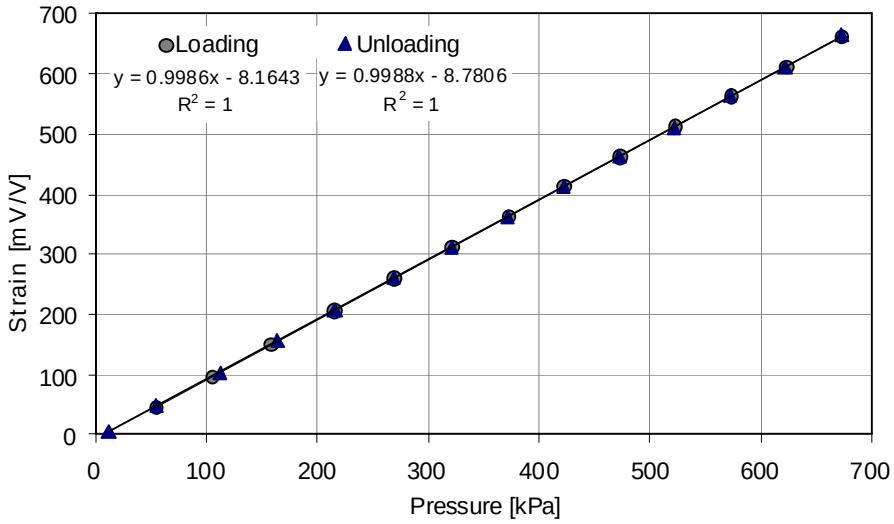

Figure 5.28. Calibration of the transducer Druck PDCR810 by using water pressure.

The probe was calibrated by comparison with an accurate air pressure gauge. The obtained results (Figure 5.27) compared with the calibration of the transducer before the saturation (Figure 5.28) shows that no relevant effect of the presence of water on the transducer response and that the instrument was not damaged during the assembling process.

5.9 EVALUATION TESTS

To check the performances of the tensiometers some evaluation tests have been conducted in a 22 °C constant temperature room. Most of the tests were performed by using the integral strain-gauged probe, only evaporation tests were conducted also with the commercial transducer based probe.

5.9.1 *Comparison of measurements against known suction values*

Comparisons of the integral strain-gauged tensiometer measurements against known values of suction were conducted to verify its time response, its ability to stand high suction for long time and to roughly verify the calibration data. The data presented in Figure 5.29 were obtained using a 15 bar filter. Similar results were obtained when 5 bar filter was used. The equilibration time of the tensiometer was examined using

silty-sand. Matric suctions of 200, 250 and 350 kPa were generated in the different samples of this material using a modified Wisa oedometer working under the axis translation technique. Matric suction of the sample was then measured dismounting the oedometer, putting the sample to the atmospheric pressure and using the UNINA probe. A thin layer of the soil paste was used to improve contact between the soil sample and the miniature tensiometer. During the test the sample remains isolated to avoid large suction changes associated to the environment conditions.

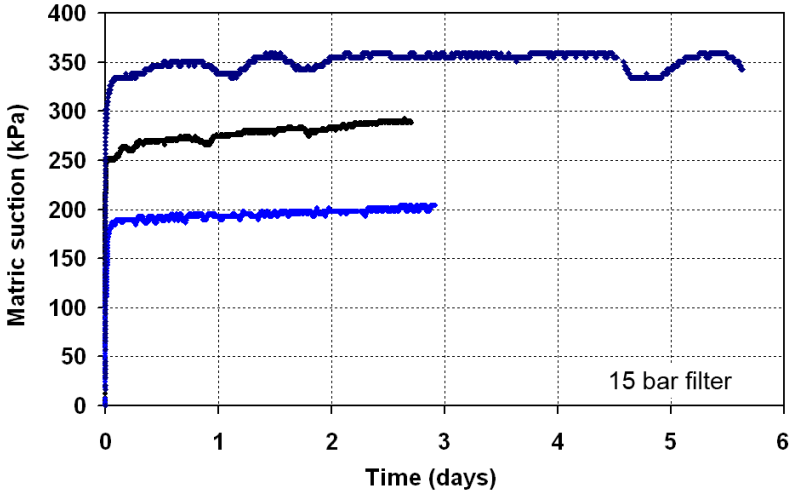

Figure 5.29. Long time suction measurements on soil samples.

The observed trend of matric suction with time may be subdivided in three parts and explained following Guan & Fredlund (1999). In the Part I, a sudden increase of readings is observed up to reach suction values a bit less than those expected on the basis of the suction applied with the axis translation technique. Subsequently, in the Part II of the tests, a slow process of suction equalization is observed. In the Part III, after a period in which suction is almost levelled to the expected value, a slow increase in tension is observed, mainly attributed to the moisture loss due to evaporation from both the soil and the suction probe during the measurement. The measurements performed on the sample preconditioned to a suction of 350 kPa present some cyclic variations. It is worth noting that large variations are observed during the I, II, V and VI day, while no variations were registered in III and IV day corresponding to Saturday and Sunday, respectively. This seems to suggest that the observed variations are related to small temperature changes in the controlled temperature room during working days.

The tests were stopped when probe measure constant suction for a time enough to validate the capacity of probe to stand high suction for long time.

5.9.2 *Evaporation tests*

Evaporation tests were performed to determine the maximum measurable suction. These tests consist in leaving the tensiometer free to dry under ambient condition until cavitation is observed. For the integral strain-gauged probe, the maximum suction value registered are 450 (Figure 5.30a) and 720 kPa (Figure 5.30b) when used 5 and 15 bar filters, respectively. For the 5 bar filter the maximum value registered is approximately the expected one (i.e. ≈ 500 kPa). This implies that the saturation process for this AEV seems to have worked properly. However, the maximum suction obtained for the 15 bar filter is almost one half of the expected value, but very near to the pre-pressurization pressure applied during saturation process (i.e. 800 kPa). It is worth noting that Figure 6 indicates a drop of the reading to -100 kPa on cavitation, indicating some accuracy of the probe calibration procedure.

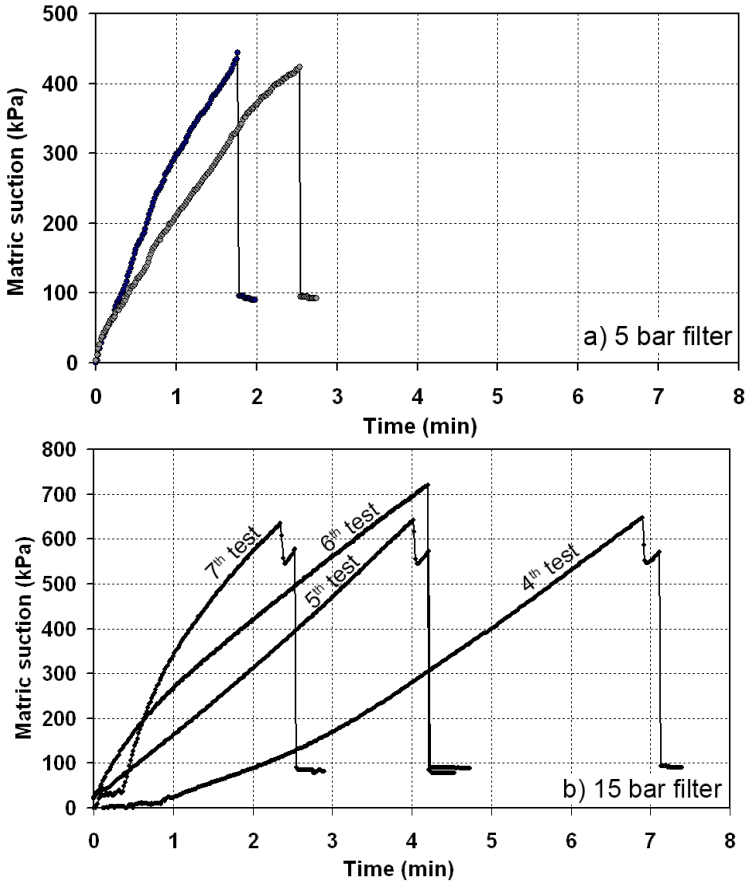

Figure 5.30. Cavitation tests: maximum measurable suction.

Table 5.6. Tension breakdown values using 15 bar filter.

Test	Maximum measured suction [kPa]
1st	330
2nd	481
3rd	566
4th	647
5th	646
6th	720
7th	635

Table 5.6 presents the values of suction measured at cavitation when the 15 bar filter is used. According to Tarantino & Mongiovì (2001), the data in Table 5.6 seem to indicate that an enhanced saturation of the ceramic filter is achieved through cycles of cavitation and subsequent pressurization and, according to Trevena (1982), that the upper limit of the tensiometer is of about 645 kPa. Obviously, if a probe is saturated at his upper limit the cycles of cavitation will not increase the probe performance and higher pre-pressurization pressure may improve its response.

Then, according to the crevice model of Atchley & Prosperetti (1989) it appear that the maximum cavitation suction depends on the past history of the system. Contrarily to the observed on Berthelot tube test, the tension breakdown value seems not affected by the tension increase rate (Figure 5.30a, b).

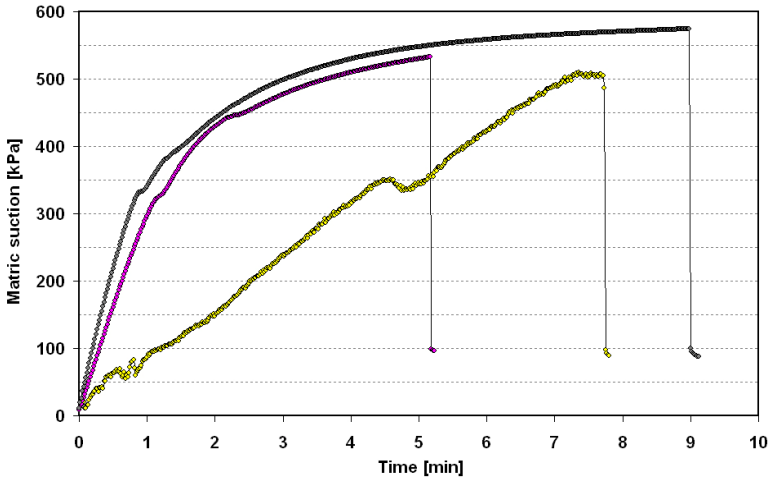

Figure 5.31. Cavitation tests: maximum measurable suction.

Figure 5.31 presents the result of tests aimed to determine the maximum sustainable suction value of the commercial transducer based probe. The procedure is

similar to the evaporation test, the variant is the use of an air-dried sample to induce high negative pressures instead to dry the HAEV porous disk under ambient condition. The maximum suction registered was 575 kPa a value slightly higher than the AEV of the porous disk, and higher than the maximum suction measured by the integral strain-gauged probe (450 kPa) when the 5 bar porous disk is used (see Figure 5.30a).

5.9.3 *Cyclic evaporation tests*

The probe ability to register rapid suction changes was examined using cyclic evaporation tests. Figure 5.32 shows several evaporation cycles, consisting in free evaporation stages up to prescribed suction value (i.e. lower than the theoretical filter's AEV) and stages in which the atmospheric pore water pressure was applied by immerging the tensiometer tip in water. The probe response to suction reversals was found excellent on properly preconditioned probes (Figure 5.32a). However, when not properly saturated the offset decrease after every reversal (Figure 5.32b), clearly indicating a lack of prove saturation.

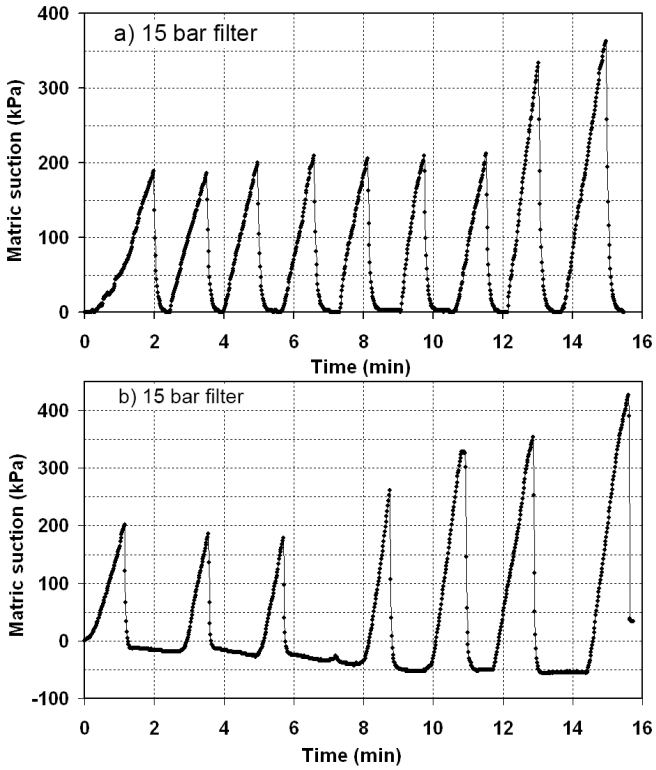

Figure 5.32. Response of the probe to suction reversals.

Chapter 6

MATERIAL PROPERTIES, SAMPLE PREPARATION AND EXPERIMENTAL PROGRAM

6.1 INTRODUCTION

This chapter begins with a description of the soil used in this investigation, the procedure for sample preparation, and the procedure followed to conduct suction controlled drained tests. It is followed by a description of the procedure used to check the performance of the triaxial.

6.2 MATERIAL PROPERTIES

The tested soil comes from a flow slide in Cava dei Tirreni, Italy (Figure 6.1).

The Cava dei Tirreni soil is pyroclastic (pyro = igneous, clastic = fragment) sand with pumice originated from pyroclastic flows fallout, consisting of particles that have been ejected from vents and have travelled at high temperature through the atmosphere before falling to earth (i.e. subaerial fallout) and then cooled. In the natural state the studied material corresponds to silty sand with gravel (SM) in the Unified Soil Classification System while the material used during the experimentation was reduced in size by sieving through a 5 mm sieve, obtaining a silty sand (SM) soil. The soil material used in this study was called “Cava dei Tirreni silty sand”. The Cava dei Tirreni silty sand consists of 60% sand, 30% silt, and 10% clay. The grain size curves are represented in Figure 6.2.

Figure 6.1. Map showing the location of Cava dei Tirreni in Campania region, Italy.

This material is a mixture of pumice particles constituting part of the coarse fraction (sand and gravel) and finer materials (sand and silt, with low clay fraction). Based on the distribution of particles (Figure 6.2), the uniformity coefficient, C_u = 144, and the coefficient of curvature, C_c = 0.2, has been determined. From this coefficients the Cava dei Tirreni silty sand can be defined as well-graded soil (i.e. C_u > 4) and gap-graded (i.e. C_c < 1). In a gap-graded soil certain range of soil grains is missing. As shown in Figure 6.3 the pore-size distribution and the pore-size density curves of a gap-graded soil are both bimodal. If the particle sizes of the coarse grains are far larger than the sizes of the fine grains and the fine grains do not completely fill the pores formed by the coarse grains, the soil can be considered as being poorly mixed and there will be two pore series in the soil governed by the coarse grains (macro pores) and the fine grains (micro pores), respectively (Zhang et al. 2005).

The dual-porosity is related with the mechanisms of secondary consolidation (Barden 1969; Navarro & Alonso 2001; Santamarina et al. 2001). This theory assumes that the soil is composed of macro (interaggregate) pores and micro (intraaggregate) pores. Primary consolidation is a consequence of the dissipation of the pore-water pressure in macropores, and secondary consolidation results from water release from micropores.

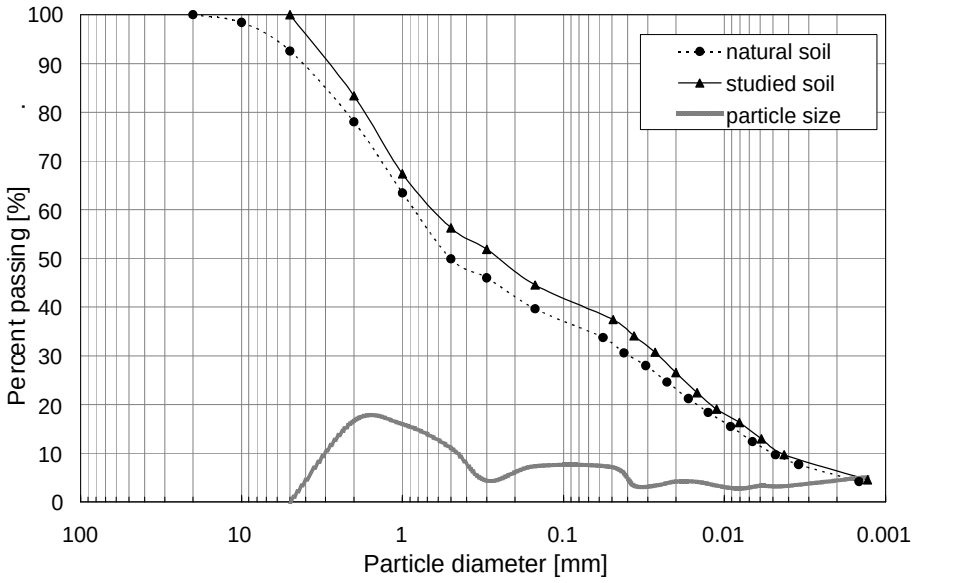

Figure 6.2. Grain size distribution curves of Cava dei Tirreni soil: natural gradation and fraction passing 5 mm sieve.

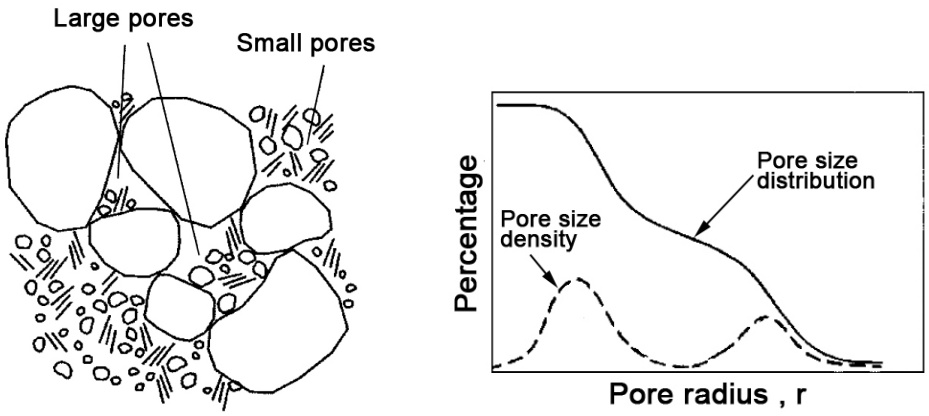

Figure 6.3. Structure, pore-size distribution, and pore-size density curves for bimodal soils (after Zhang et al. 2005).

6.2.1 *Physical properties of pyroclastic soils with pumice*

As mentioned, the Cava dei Tirreni soil is composed of coarse fraction (sand) and finer materials (silt, with low clay fraction). Pumice particles constitute the majority of the coarse fraction; the most notable feature is its very low density, which enables pumice to float on water for a period of time before eventually waterlogging enough to sink (see Figure 6.4). The pumice microstructure consists of sub-angular grains of very variable size with rough surfaces and intrinsic inter-particle bonds of the same constituents, probably due to the original mode of deposition. The presence of inter- and intra-particles voids within the pumice can cause differences in the physical and volumetric parameters, of this volcanic soil, compared with common sandy soils.

Figure 6.4. Presence of pumice in Cava dei Tirreni silty sand.

The pumice grains are highly vesicular[1] and soft. The vesicularity of all pumice clasts is 75 to 88 %, with >90 % interconnected pore volume (Whitam & Sparks 1986; Klug et al. 2002). On the contrary, Pellegrino (1967) and Wesley (2001) showed the existence of unconnected voids in the pumice from the Phlegraean Fields, Naples (Italy) and New Zealand, respectively. Figure 6.5a shows a close up of a characteristic pumice particle with vesicular texture, where most of the voids are clearly interconnected, and the presence of inter- and intra-particle voids are evident. Figure 6.5b presents a close up of the Cava dei Tirreni pumice particles having similar texture to that shown in Figure 6.5a.

[1] The term vesicular refers to the presence of vesicles, or irregularly shaped cavities, that produce a sponge-like or bubbly texture and very low density in volcanic material.

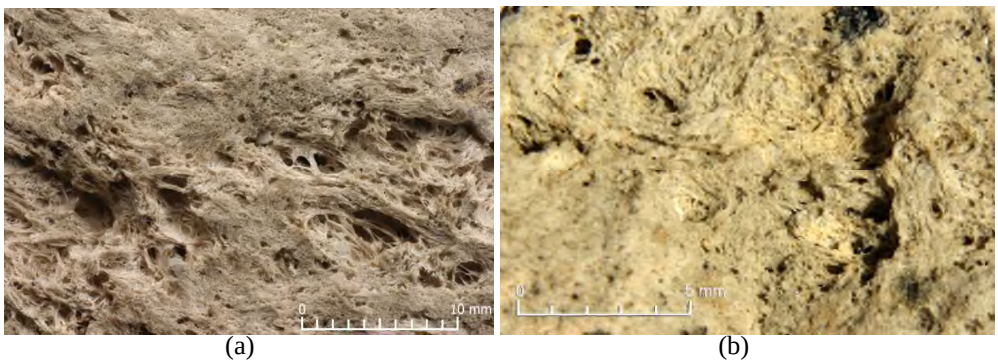

(a) (b)

Figure 6.5. Vesicular texture of pumice particles. (a) characteristic texture of vesicular pyroclastic particles (http://facweb.bhc.edu/); (b) pumice particles of Cava dei Tirreni soil.

The presence of intraparticles voids (vesicles in Figure 6.6c) difficult the measurement of soil parameters like specific gravity and void ratio (Wesley 2001). The state of packing of the particles is represented by the spaces around the particles; parameters like void ratio are calculated in function of this space (i.e. the space out of dotted line in Figure 6.6b). However, when standard procedures are used to determine specific gravity[2], the result tend to approach that of the material are composed, rather than that of the particles as a whole (Wesley 2001). And consequently, this assumption is transferred to the void ratio determination; representing the total void volume (Figure 6.6a) instead of only the interparticle voids (Figure 6.6b).

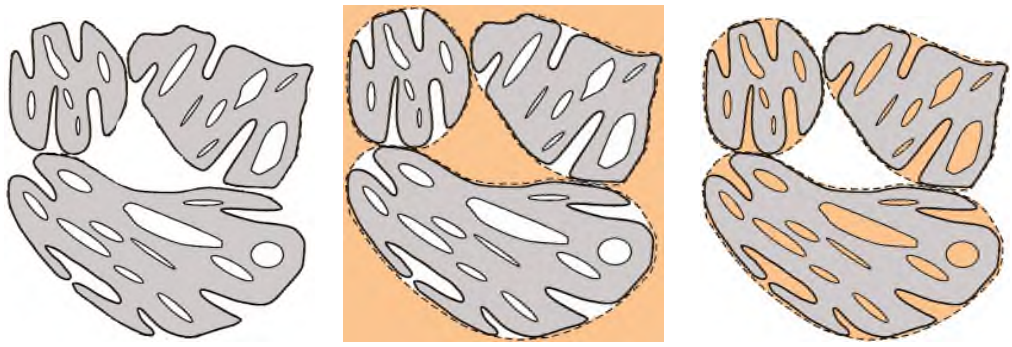

Figure 6.6. Schematic representation of pumice particles (modified from Wesley 2001). (a) vesicular pumice particles; (b) interparticle voids. (c) intraparticle voids.

[2] In the standard methods, the air present in the void space between soil particles is removed by applying the vacuum extraction technique.

In spite of the limitations of the standard method encountered by many Authors, for this study, the specific gravity was determined by the standard test ASTM D 854. Following this method, a specific gravity of 2.68 was determined for the Cava dei Tirreni soil.

6.3 SPECIMEN PREPARATION PROCEDURE

Once the soil was classified, a compaction method had to be selected to generate a specimen that could be duplicated. The duplication was in terms of moisture content and dry density. This duplication was important to eliminate any adverse effects that the properties of the specimens might have from test to test.

The main problem to deal with is to produce reconstituted volcanic silty-sand samples with a low enough density so as to be similar to the undisturbed volcanic ones. In the Campania region (Italy), pyroclastic soils are characterized by high void ratio; ranging from 0.7 to 2.3 (Pellegrino 1967). According to these values, two void ratios have been selected: e = 1.30, to validate the improved triaxial apparatuses; and e =1.66 for soil characterization.

The choice of using reconstituted specimens introduced the problem of selecting an appropriate preparation method, since the behaviour of granular soils is strongly affected by the procedure selected, especially in the case of sands containing fines. Air pluviation (AP), water pluviation (WP) and moist tamping (MT) are the literature methods considered. According to Kuerbis & Vaid 1998 WP and AP techniques resulted in segregation when used with silty sands as revealed by thin lenses of fine particles. Opposite to some literature works (Vaid et al. 1999) indicating that specimens reconstituted by MT method tend to be non-uniform compared to the WP and AP (Frost & Park 2003) in the case of the soil under study the MT method appeared the most stable one due to the high content of fines (i.e. 40 %).

In the tests reported in this study, all the specimens were prepared using the MT method. This was considered prudent due to the presence of fines, and the problems of segregation that characterise the WP and AP techniques had to be avoided.

The MT method produces very loose to dense unsaturated samples. Due to the large water tension forces between grains generated in silty sand soils, structures may be assembled in such a loose state (even above the maximum void ratio, e_{max}) that they may undergo large strains during the saturation process due to the removal of water tension forces between grains (Ishihara 1993). The compressibility of the MT sand is very high compared to that of the AP and WP sand. The observed behaviour is believed due to the potentially collapsible fabric that generates the MT method (Vaid et al. 1999).

6.3.1 *Initial moisture content*

The soil was taken from a batch prepared by combining several samples obtained from the same place. The batch was thoroughly mixed and then air-dried. After that, the dry silty sand material was mixed with a defined amount of water. The target water content for the samples was 28.5 % by weight. Thereafter, the soil was stored and sealed inside a double plastic bag so that the water could be distributed evenly throughout the soil.

6.3.2 *Moist tamping compaction*

The moist tamping method was used for preparing the samples. Figure 6.7 shows a schematic of the moist tamping device. Basically, in this method, a reference collar attached to the tamping rod is adjusted prior to the compaction of each layer to guarantee that the compaction foot could no be advanced beyond the desired elevation during the compaction of the layer.

The undercompaction method (Ladd et al. 1978) was used to achieve uniform specimens. The moist-tamped specimens tested in this study were placed in five equal-thickness layers. Due to the low compactive effort used, the underlying layers showed no further settlement during subsequent layer placement and compaction. Then, each sample was prepared in five layers of equal height.

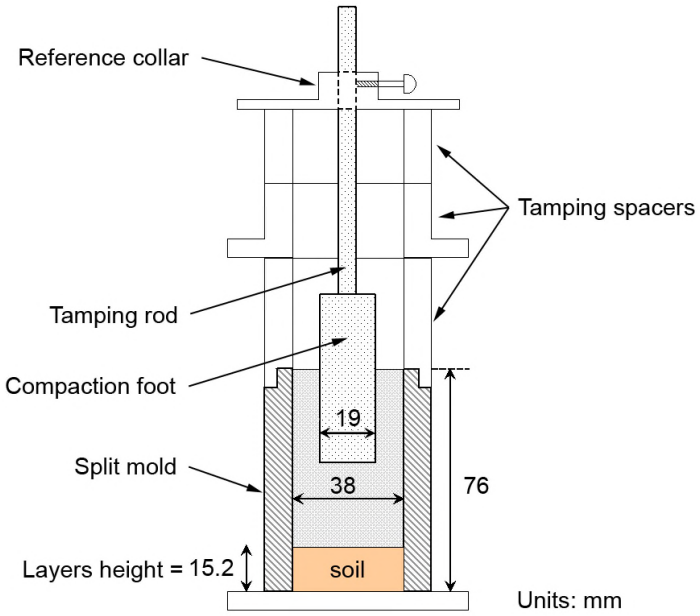

Figure 6.7. Schematic layout of moist tamping device.

The moist silty sand was carefully spooned into the split mold and roughly levelled with a spoon. The eight of each layer was taken as one-fifth the distance from the top of the split mold to the bottom. A calliper was used to position the reference collar on the tamping rod for the height of the first layer. The tamper was then lowered into the mold, and the soil was gently compressed until the set ring contacted the top of the split mold. Since the tamping foot had a diameter equal to one-half the diameter of the split mold, the entire surface was compacted by moving the tamper around the perimeter of the mold. This process should be conducted carefully, the loss of compaction in the perimeter generate a roughness external surface on samples. The top of the compacted layer was then scarified slightly to promote bonding of the next layer. A piece of plastic was used to cover the split mold to prevent any moisture loss while the material for the following layer was being weighted.

This procedure was repeated for each five layers. However, tamping spacers was placed atop the split mold to facilitate the tamping of the last three layers. When the last layer was completed, a very flat surface is obtained. A 50 g fraction of the remaining sandy soil was used to determine the water content.

A summary of the sample preparation is shown in Figure 6.8 and illustrated in the following:

Step 1 – joint the three parts of the mold (i.e. the mold walls and the 1st tamping spacer); and place the mounted mold onto a flat, non adherent and non absorbent surface (e.g. glass).

Step 2 – weight 22.5 g of soil and regulate the reference collar of tamping rod in order to obtain a layer of 15.2 mm. Repeat the process five times.

Step 3 – after compact the fifth layer, the soil reach the upper level of split mold (i.e. 76 mm)

Step 4 – remove all the sample spacers.

Step 5 – a sample ejector is used just to support the specimen during the split-mold dismounting process. The split mould combined with the sample ejector eliminates any frictional resistance when the specimen is extracted.

Step 6 – as result of the compaction process a sample of 38 mm in diameter, 76 mm in height, 112.5 g in total mass, and 1.67 in void ratio is obtained.

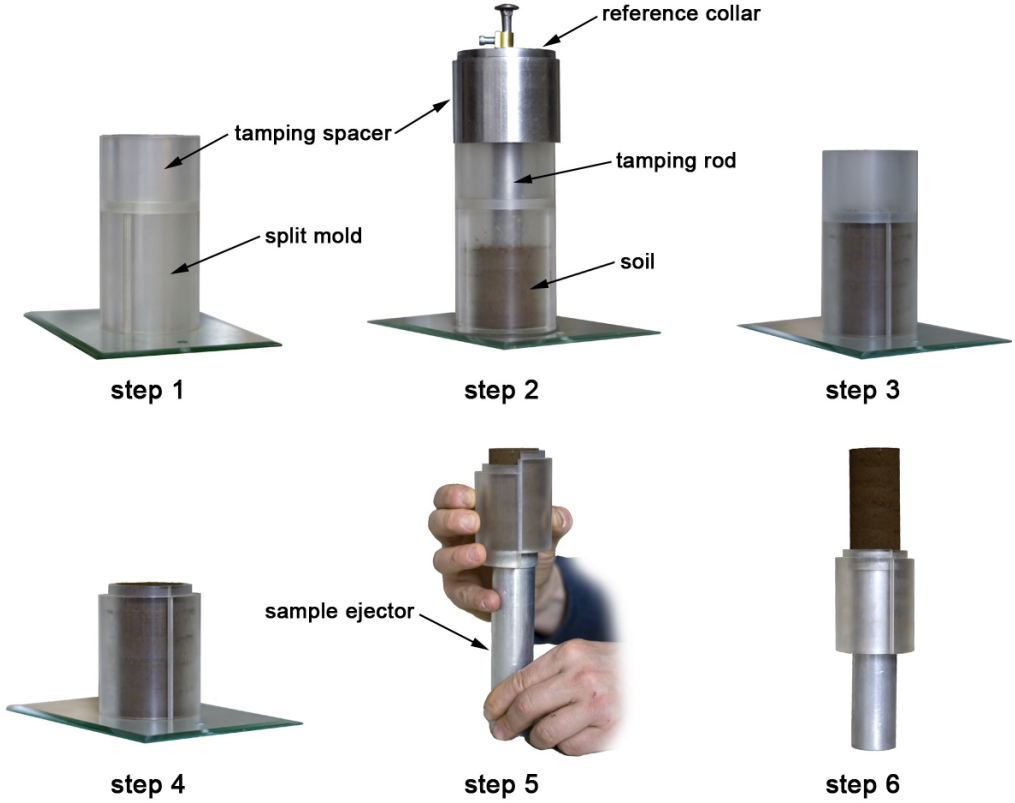

Figure 6.8. Steps of sample preparation.

6.4 TESTING PROGRAM

The testing program has been divided in three: Isotropic compression tests, shear compression tests and pore-water pressure measurement during suction controlled tests.

The specimens were designated using the symbol $\mathbf{s}x\boldsymbol{\sigma}_3y(z)$, in which:

- x is the matric suction ($u_a - u_w$),

- y is the net confining pressure ($\sigma_3 - u_a$),

- z denotes the rate of loading applied in isotropic compression test or the strain rate (i.e. slow S or fast F) in deviatoric compression tests.

6.4.1 *Isotropic compression stage*

A total of 13 drained isotropic compression tests were conducted in the triaxial test devices to characterize the behaviour of unsaturated soil under different loading rates. Once the specimens were equalized at the specified initial suction (i.e. 15, 45 and 300 kPa), while maintaining the suction constant at the ends of sample, these were isotropically compressed to the required net mean stress. The loading rates applied in tests were 8, 32 and 128 kPa/h. For the 300 kPa suction series an additional test applying a loading rate of 2 kPa/h was conducted. And for suction values of 0, 5 and 100 kPa only one loading rate was tested (i.e. 32, 8, 32 kPa/h). Details of the testing program are summarized in Table 6.1.

Table 6.1. Summary of the isotropic compression testing program.

No.	Test	Matric suction ($u_a - u_w$)	Isotropic compression	
			Net confining stress ($\sigma_3 - u_a$)	Rate of loading
		[kPa]	[kPa]	[kPa/h]
1	s0$\sigma_3$600(32)	0	600	32
2	s5$\sigma_3$670(8)	5	670	8
3	s15$\sigma_3$660(8)	15	660	8
4	s15$\sigma_3$660(32)	15	660	32
5	s15$\sigma_3$660(128)	15	660	128
6	s45$\sigma_3$600(8)	45	600	8
7	s45$\sigma_3$600(32)	45	600	32
8	s45$\sigma_3$600(128)	45	600	128
9	s100$\sigma_3$575(32)	100	575	32
10	s300$\sigma_3$375(2)	300	375	2
11	s300$\sigma_3$375(8)	300	375	8
12	s300$\sigma_3$375(32)	300	375	32
13	s300$\sigma_3$375(128)	300	375	128

6.4.2 *Triaxial compression tests*

Based on previous test conducted on similar samples, the 0.025 mm/min rate was selected as the baseline. Since significant behaviour changes typically manifest themselves over logarithmic cycles, the 0.25 mm/min was selected as the next higher rate.

A total of 18 drained triaxial compression tests were conducted in the triaxial test devices to characterize the behaviour of unsaturated soil under different loading rates. Once the specimens were equalized at the specified initial suction (i.e. 15, 45 and 300

kPa), while maintaining the suction constant at the ends of sample, the isotropic load has been applied in tests at 32 kPa/h loading rate. Details of the testing program are summarized in Table 6.2.

Table 6.2. Summary of the isotropic compression testing program.

No.	Test	Matric suction ($u_a - u_w$)	Isotropic compression		Shearing
			Net confining stress ($\sigma_3 - u_a$)	Rate of loading	Strain velocity
		[kPa]	[kPa]	[kPa/h]	[mm/min]
1	$s0\sigma_3 50S$	0	50	32	0.025
2	$s0\sigma_3 50F$	0	50	32	0.25
3	$s0\sigma_3 400S$	0	400	32	0.025
4	$s15\sigma_3 50S$-a	15	50	32	0.025
5	$s15\sigma_3 50S$-b	15	50	32	0.025
6	$s15\sigma_3 50F$	15	50	32	0.25
7	$s15\sigma_3 100F$	15	100	32	0.25
8	$s15\sigma_3 200S$	15	200	32	0.025
9	$s15\sigma_3 200F$	15	200	32	0.25
10	$s45\sigma_3 20F$	45	20	32	0.25
11	$s45\sigma_3 50F$	45	50	32	0.25
12	$s45\sigma_3 100F$	45	100	32	0.25
13	$s45\sigma_3 200S$	45	200	32	0.025
14	$s45\sigma_3 200F$	45	200	32	0.25
15	$s300\sigma_3 50S$	300	50	32	0.025
16	$s300\sigma_3 50F$	300	50	32	0.25
17	$s300\sigma_3 100F$	300	100	32	0.25
18	$s300\sigma_3 200F$	300	200	32	0.25

6.4.3 *Pore-water pressure measurement*

In order to determine an optimum loading rate for the Cava dei Tirreni pyroclastic soil, a series of suction-controlled isotropic compression tests were conducted on half-size compacted samples of the pyroclastic silty sand. To compare the data with the obtained when full-size samples (76 mm in height) were tested, a similar testing program was followed.

A total of 14 drained isotropic compression tests were conducted at different suction values (i.e. 15, 45 and 300 kPa), while maintaining the suction constant at the ends of sample, during the different stages the pore-water pressure was measured. The loading rates applied in tests were 8, 32 and 128 kPa/h. For the 300 kPa suction series an additional test applying a loading rate of 2 kPa/h was conducted. And

additional test was conducted for a suction values of 150 kPa, and only one loading rate was tested (i.e. 128 kPa/h). Details of the testing program are summarized in Table 6.1.

Table 6.3. Summary of the isotropic compression testing program in half-size sample.

No.	Test	Matric suction $(u_a - u_w)$	Isotropic compression	
			Net confining stress $(\sigma_3 - u_a)$	Rate of loading
		[kPa]	[kPa]	[kPa/h]
1	s15$\sigma_3$660(8)h	15	660	8
2	s15$\sigma_3$660(32)h	15	660	32
3	s15$\sigma_3$660(128)h	15	660	128
4	s45$\sigma_3$600(8)	45	600	8
5	s45$\sigma_3$600(32)h-a	45	600	32
6	s45$\sigma_3$600(32)h-b	45	600	32
7	s45$\sigma_3$600(128)h-a	45	600	128
8	s45$\sigma_3$600(128)h-b	45	600	128
9	s150$\sigma_3$500(128)h	150	500	128
10	s300$\sigma_3$375(8)h	300	375	8
11	s300$\sigma_3$375(32)h	300	375	32
12	s300$\sigma_3$375(128)h-a	300	375	32
13	s300$\sigma_3$375(128)h-b	300	375	32
14	s300$\sigma_3$375(128)h-c	300	375	128

Chapter 7

EXPERIMENTAL RESULTS AND INTERPRETATION

7.1 ISOTROPIC COMPRESSION TESTS

For the isotropic compression tests, samples (38 mm in diameter and 76 mm in height) were obtained by moist tamping compaction method, as explained in Chapter 3. Before the isotropic compression, predefined suction values were imposed. The results and the conclusions obtained from suction equalization and isotropic compression stages are described in this section.

7.1.1 *Suction equalization stage*

All the equalization stages are run under a constant net confining stress ($\sigma_3 - u_a$) of 20 kPa and a deviator stress (q) of about 5 kPa. Such values are selected in order to prevent collapse (i.e. irreversible volume decreases on wetting) and to allow the identification of even low yield stresses in the subsequent compression stages. Water content changes are reported in Figure 7.1, the results shows that the suction value after compaction is about 45 kPa, for suction values less than this value (i.e. 5 and 15 kPa) a flow of water towards the soil occurs (i.e. water content increase) and for suction values higher than 45 kPa (i.e. 100, 200 and 300 kPa) the water flows in the opposite direction (i.e. water content decrease).

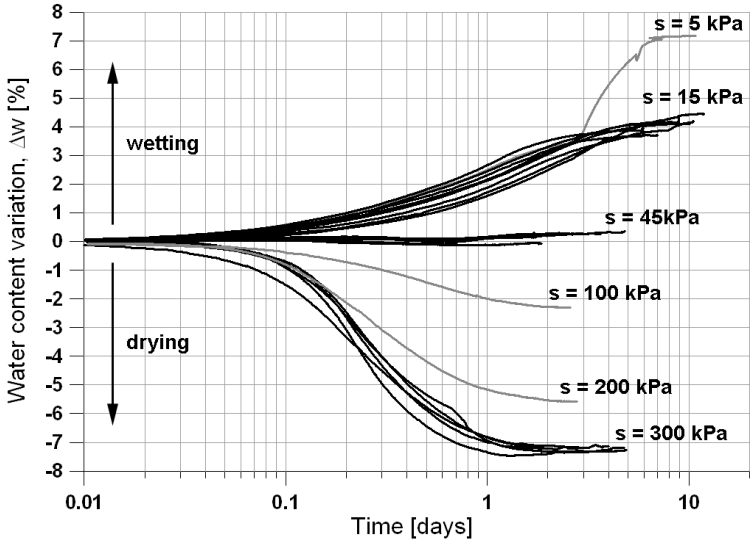

Figure 7.1. Water content changes during the equalization stages.

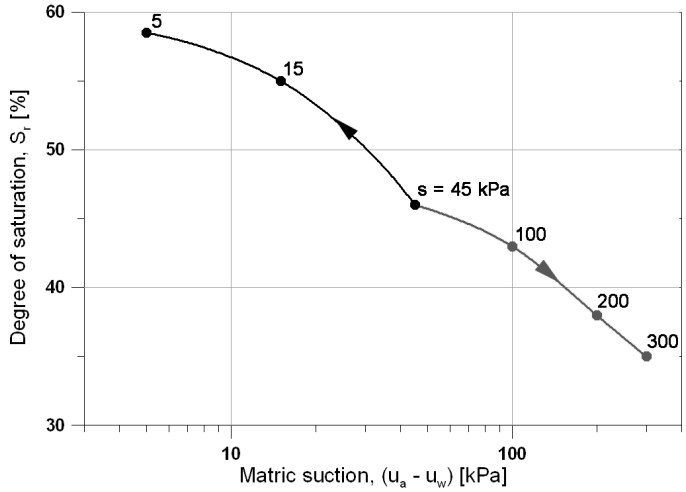

Figure 7.2. Soil water retention curve (SWRC) obtained from the suction equalization stage.

Figure 7.2 shows the soil water retention curve (SWRC) obtained from the equalization stage data. As the initial suction value of samples is approximately 45 kPa (S_r = 46 %), neither main drying curve nor main wetting curve was determined. The two different paths presented in Figure 7.2 are: (i) the black one corresponds to a wetting scanning curve, and (ii) the gray one to a drying scanning curve. Figure 7.2 demonstrates that this soil remains unsaturated on a wetting path at low suction

values (up to 5 kPa). Further suction reduction led to a significant increment in degree of saturation.

7.1.2 *Isotropic compression stage*

The result of each test is summarized in two graphs:

a) net confining stress (σ_3 - u_a) versus specific volume variation Δv,

b) net confining stress (σ_3 - u_a) versus degree of saturation Sr,

Figure 7.1 shows the experimental data pertaining to the isotropic compression tests on 15 kPa suction specimens. As expected for the low suction range, the applied loading rates seem to have an insignificant effect on the specific volume and degree of saturation. The data obtained for this series (i.e. 15 kPa) is summarized in Table 7.1.

Also three rates of loading, 8, 32 and 128 kPa/h, were employed for this pyroclastic soil under a pseudo-constant suction of 45 kPa, but there was no a clear trend in the effect of the rate in this range of loading rate, as shown in Figure 7.4a. The maximum difference in the preconsolidation pressures is not negligible, but is relatively small (Table 7.1). The net confining stress (σ_3 - u_a) versus degree of saturation Sr relation for the samples at 45 kPa of suction are shown in Figure 7.4b. Similar paths of degree of saturation change are observed for the rate of loadings 8 and 128 kPa/h. However, a higher change is observed when the rate of 32 kPa/h is applied, especially at high net confining stress values.

Table 7.1. Summary of main parameters obtained from the isotropic compression tests.

No.	Test	Preconsolidation stress p_0[kPa]	Compressibility coefficient $\lambda(s)$
1	$s0\sigma_3600(32)$	45	0.121
2	$s5\sigma_3670(8)$	---	0.148
3	$s15\sigma_3660(8)$	58	0.168
4	$s15\sigma_3660(32)$	51	0.163
5	$s15\sigma_3660(128)$	58	0.161
6	$s45\sigma_3600(8)$	70	0.170
7	$s45\sigma_3600(32)$	60	0.169
8	$s45\sigma_3600(128)$	73	0.175
9	$s100\sigma_3575(32)$	91	0.170
10	$s300\sigma_3375(2)$	107	0.206
11	$s300\sigma_3375(8)$	118	0.190
12	$s300\sigma_3375(32)$	110	0.153
13	$s300\sigma_3375(128)$	113	0.160

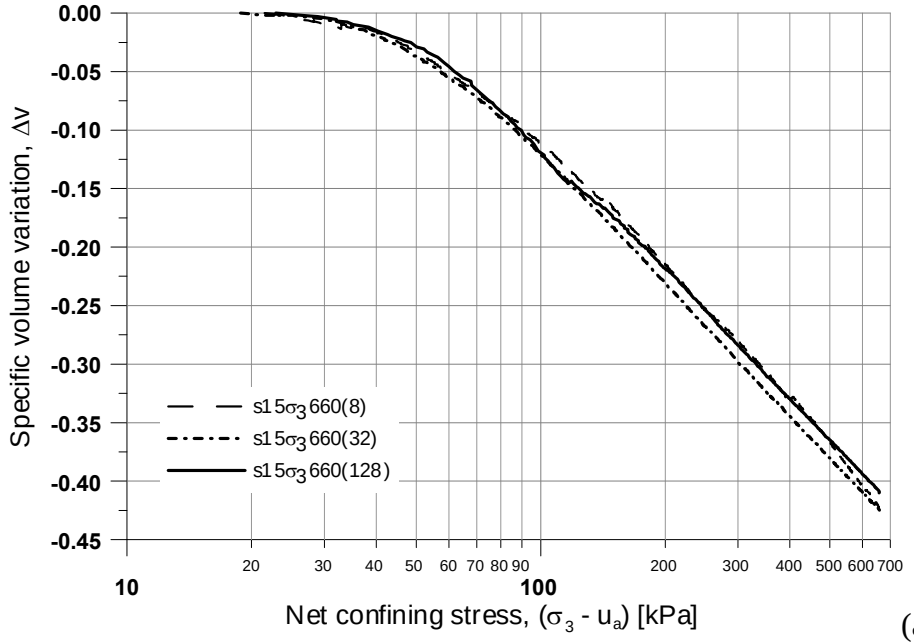

(a)

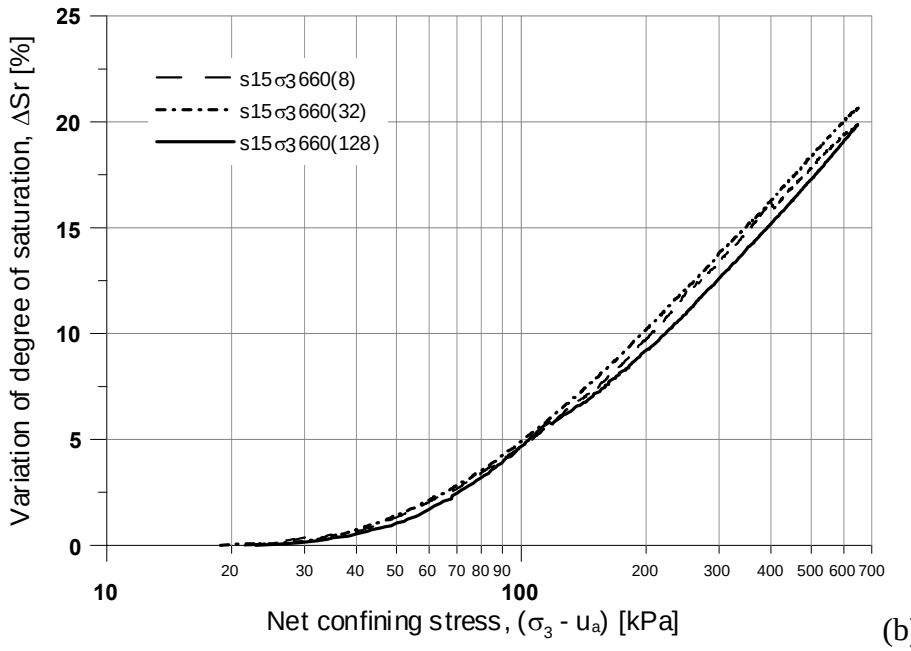

(b)

Figure 7.3. Isotropic compression tests at a constant suction of 15 kPa and at different loading rate ($\dot{\varepsilon}$ = 8, 32 and 128 kPa/h): net confining stress versus (a) specific volume variation and (b) variation of degree of saturation.

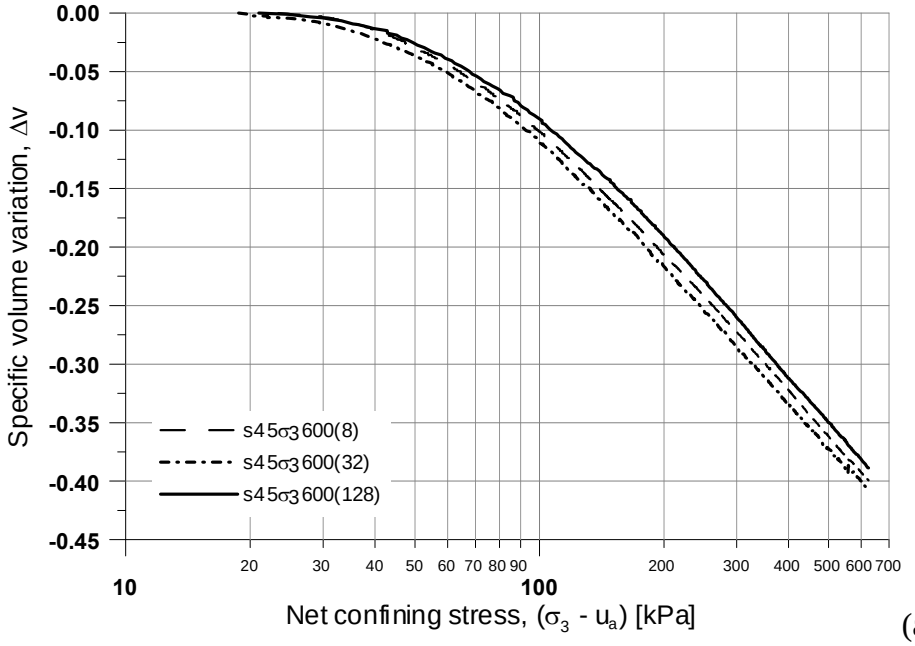

(a)

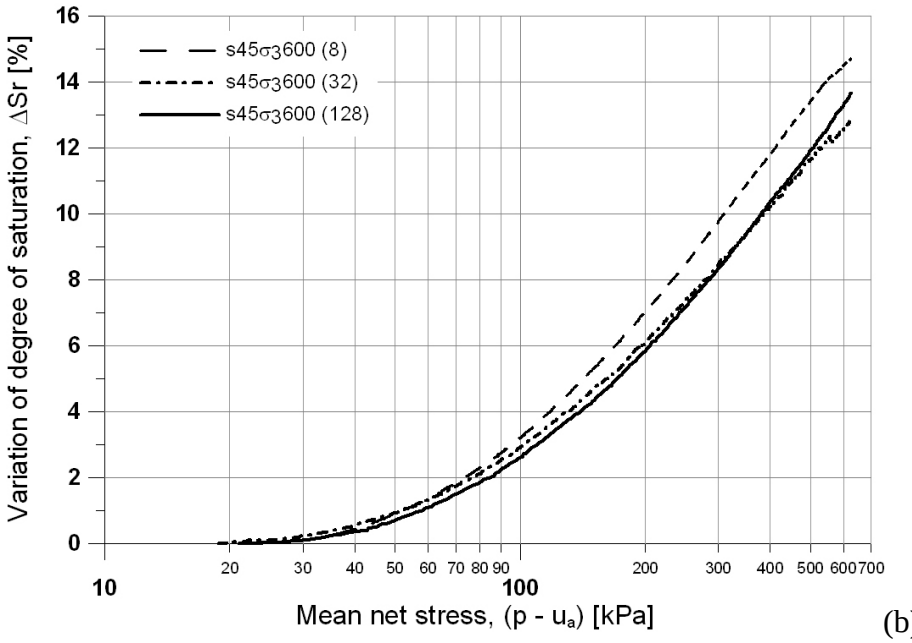

(b)

Figure 7.4. Isotropic compression tests at a constant suction of 45 kPa and at different loading rate ($\dot{\varepsilon}$ = 8, 32 and 128 kPa/h): net confining stress versus (a) specific volume variation and (b) variation of degree of saturation.

In contrast with the observations reported in Huat et al. (2006), for the loading rates 2, 8 and 32 kPa/h, the higher is the rate of loading the lower is the sample compressibility (Figure 7.5a). The observed behaviour is similar to the data reported on Crawford (1964), where different time intervals were applied during incremental loading (IL) oedometer tests performed on saturated Leda clay. The reason for such variation is that as time, *t*, is increased the amount of creep of the specimen is also increased. As a matter of fact, if the presence of a too high rate of loading is postulated, a pore water pressure increases, hence a suction decrease, should be expected during the "high" rate of loading isotropic compression tests. If this was the case, an increase of soil compressibility with rate of loading must be expected in opposition to what has been observed during the tests. Since creep deformations should have developed during all the tests duration, it is quite obvious that for the sample s300$\sigma_3$375(2) compression effects occurred during the 185 h employed to reach the final net mean stress (i.e. (σ_3 - ua) = 375 kPa). In samples s300$\sigma_3$375 (8) and s300$\sigma_3$375(32) this phenomena is less evident and the compressibility is lower since a significantly shorter time (46 h and 12 h, respectively) is required to reach the same isotropic compression stress. However, when the loading rate is increased to 128 kPa/h (i.e. test s300$\sigma_3$375(128)) the compressibility increases showing an opposite behaviour than the analyzed before for lower rates of loading. In this case, the excess pore-water pressure generated during loading process reduces the suction value, and due to the relative short time required (3 h) to reach the target net confining stress (375) the creep phenomena is negligible. Figure 7.5a also shows that it is possible to obtain four slightly different values of preconsolidation pressure dependent upon the choice of rate of loading (see Table 7.1). On the other hand, the variation on degree of saturation, represented in Figure 7.5b, is similar for samples s300$\sigma_3$375 (2) and s300$\sigma_3$375 (8), but slightly lower for samples s300$\sigma_3$375 (32) and s300$\sigma_3$375 (128).

Figure 7.6 shows the experimental data pertaining to the compression stages at a loading rate of 32 kPa/h displaying specific volume against net confining stress. As the initial suction value is 45 kPa (i.e. after compaction), the drying and wetting processes cause a specific volume reduction due to shrinkage and collapse, respectively. Similarly, the slope of the normal compression lines (i.e. compressibility λ) changes from 0.169 at s = 45 kPa to 0.153 at s = 300 kPa for drying path, and to 0.121 at s= 0 kPa for wetting path. These curves also allow the identification of a significant increase in the yield net confining stress with suction, indicating that preconsolidation pressure rises from 45 kPa at s = 0 kPa to about a25 kPa at s = 110 kPa.

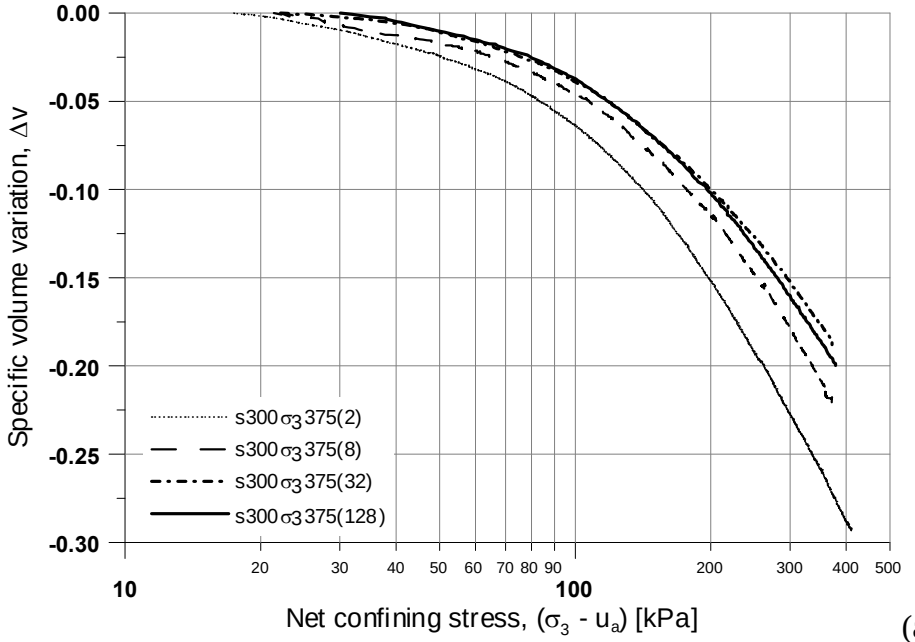

(a)

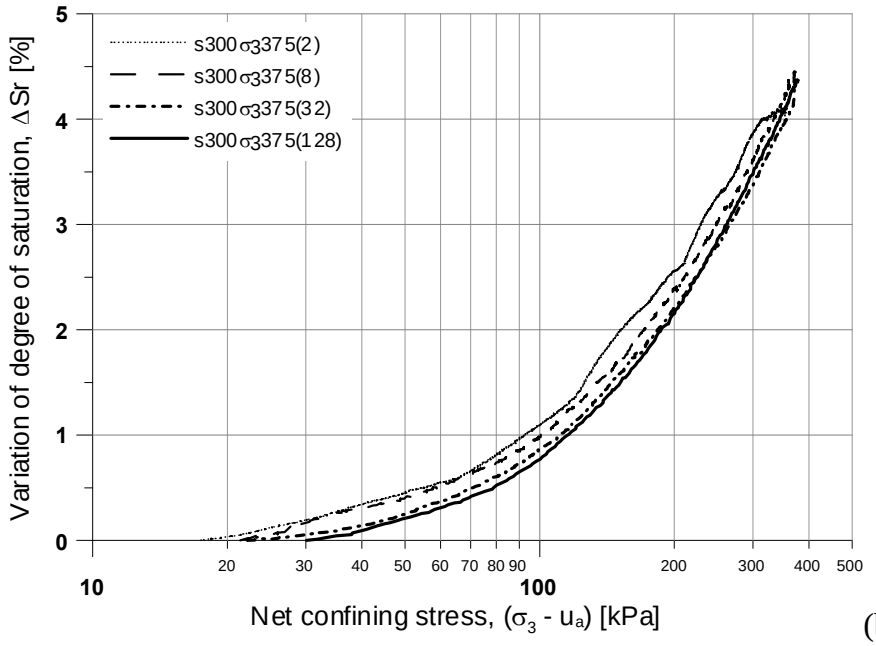

(b)

Figure 7.5. Isotropic compression tests at a constant suction of 300 kPa and at different loading rate ($\dot{\boldsymbol{\varepsilon}}$ = 2, 8, 32 and 128 kPa/h): net confining stress versus (a) specific volume variation and (b) variation of degree of saturation.

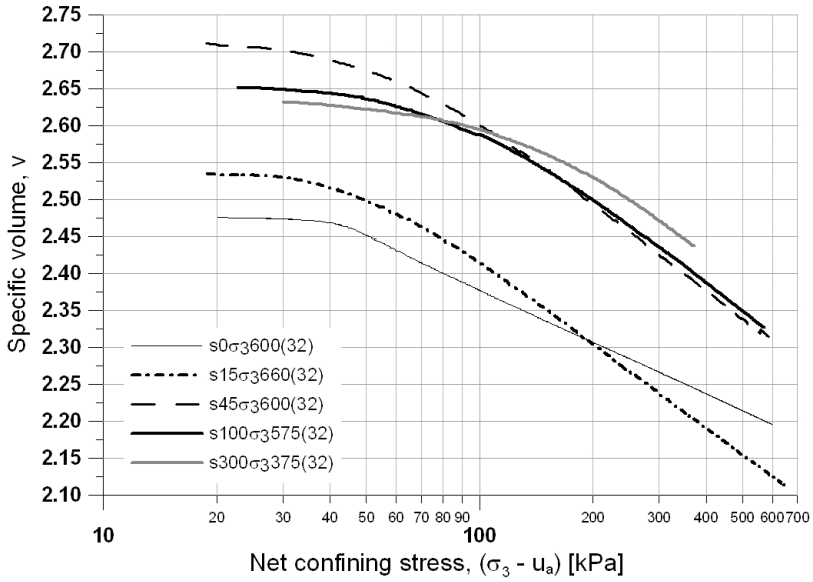

Figure 7.6. Isotropic compression tests at a loading rate of 32 kPa/h and at different suction values (s = 0, 15, 45,100 and 300 kPa): net confining stress versus specific volume.

The high compressibility of the silty sand soil is a sign of the well-graded nature of the soil. The yield stresses were estimated for the pyroclastic soil from the Cui and Delage et al. (1996) graphical method; where the yield point is determined by the intersection of the initial straight portion and the final straight section of the curve (in a net confining stress logarithmic representation). Figure 7.7 shows the yield points (i.e. preconsolidation pressures) represented against suction.

Isotropic consolidation tests on unsaturated soils give information on the variation of the compressibility with suction. For the range of applied net mean stress, suction values and loading rate, points belonging to the isotropic normal compression lines (NCL) can be identified. Plotting the compressibility λ versus suction allows the examination of the effect of loading rate and suction (Figure 7.8). For the highest loading rates (i.e. 32 and 128 kPa/h), shown in Figure 7.8, an initial increase in compressibility at low suction value is noticed, followed by a reduction. A summary of both the preconsolidation pressure and the compressibility is presented in Table 7.1.

For suction ranging from 0 to 45 kPa, the compressibility of the pyroclastic soil shows relatively little variation with loading rate. However, a significant effect in the value of λ is observed when the imposed suction is 300 kPa.

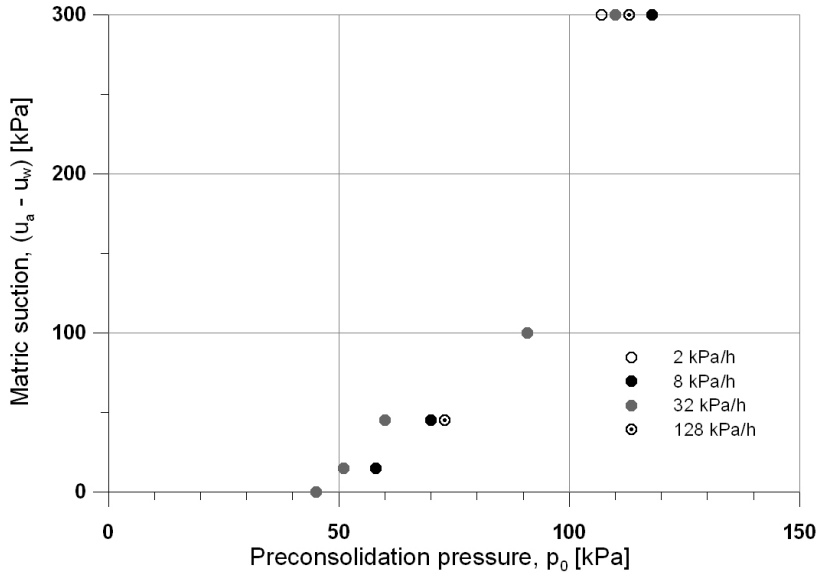

Figure 7.7. Evolution of preconsolidation pressure with loading rate.

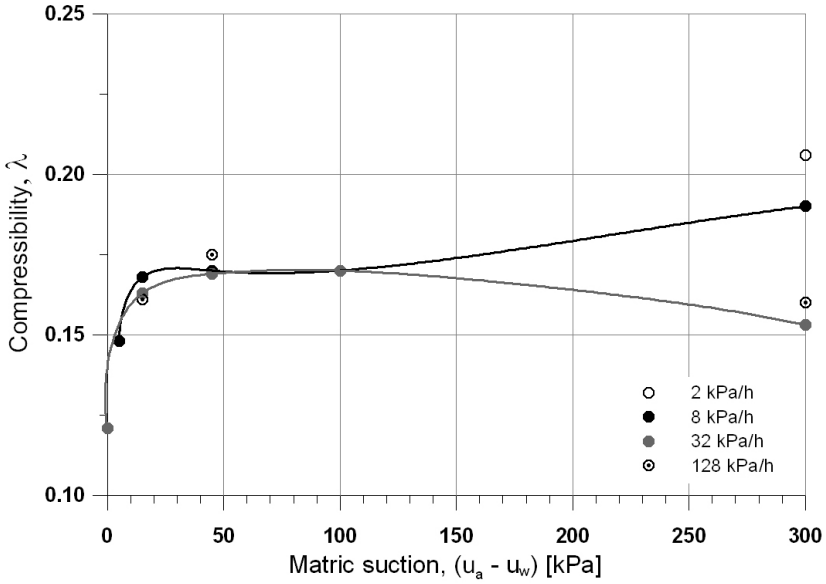

Figure 7.8. Compressibility as a function of loading rate.

7.2 TRIAXIAL COMPRESSION TESTS

Consolidated drained triaxial tests (CD), whit pore-air and pore-water drainage allowed, were carried out under three values of controlled suction: 15, 45 and 300 kPa. To obtain the strength envelope at each constant suctions, three series of CD tests were carried out under constant net confining stresses ($\sigma_3 - u_a$) of 50, 100 and 200 kPa, except for the series at s = 45 kPa in which an extra value of net confining stress ($\sigma_3 - u_a$ = 20 kPa) was applied. The strain rate used in the tests was 0.25 mm/min and additionally, to study the effect of strain rate on soil strength, some test were conducted applying a slower rate (i.e. 0.025 mm/min). The results are summarized in four graphs in each figure:

a) axial strain ε_a versus deviatoric stress q
b) axial strain ε_a versus volumetric strain ε_v
c) axial strain ε_a versus water volumetric strain ε_{vw}
d) axial strain ε_a versus variation of degree of saturation S_r

Triaxial tests under saturated conditions have also been performed, the data for which are presented only in Figure 7.21.

The results of the triaxial consolidated drained tests are shown in Figure 7.9 to Figure 7.20.

Dilatant behaviour is noticed for the tests (Figure 7.11, and Figure 7.13) at values of confining stress ($\sigma_3 - u_a$) of 20 and 50 kPa at suction values of 45 and 300 kPa, respectively. In these tests the peak deviator stress is reached at smaller axial strains (12 and 10 %, respectively) compared with another tests (more than 16 % of axial strain). Is evident that the soil behaviour changes from dilation to compression with increase of confining stress ($\sigma_3 - u_a$), which also increases the axial strain at peak, similar behaviour were observed by Rahardjo et al. 2004; Futai & Almeida 2005; Geiser et al. 2006; Cattoni et al. 2007.

Figure 7.9, Figure 7.11, and Figure 7.13 show that the stiffness of the soil specimens generally increases with increasing net confining stresses. In a similar way, Figure 7.15, Figure 7.17, and Figure 7.19 show that also stiffness increase with increasing matric suction. The exception occurred for specimens under 45 kPa.

The good agreement in stress-strain curves between the specimens during shearing could be attributed to the high quality specimens in terms of reproducibility obtained by the used compaction technique (i.e. moist tamping) and also due to the good reproducibility of suction equalization and compression stages.

Some specimens (s45$\sigma_3$20F, s300$\sigma_3$50S and s300$\sigma_3$50F), after a short dilation at the beginning of shearing, slightly compressed and then dilated again until failure, resulting in the final total volume being larger than the initial total volume.

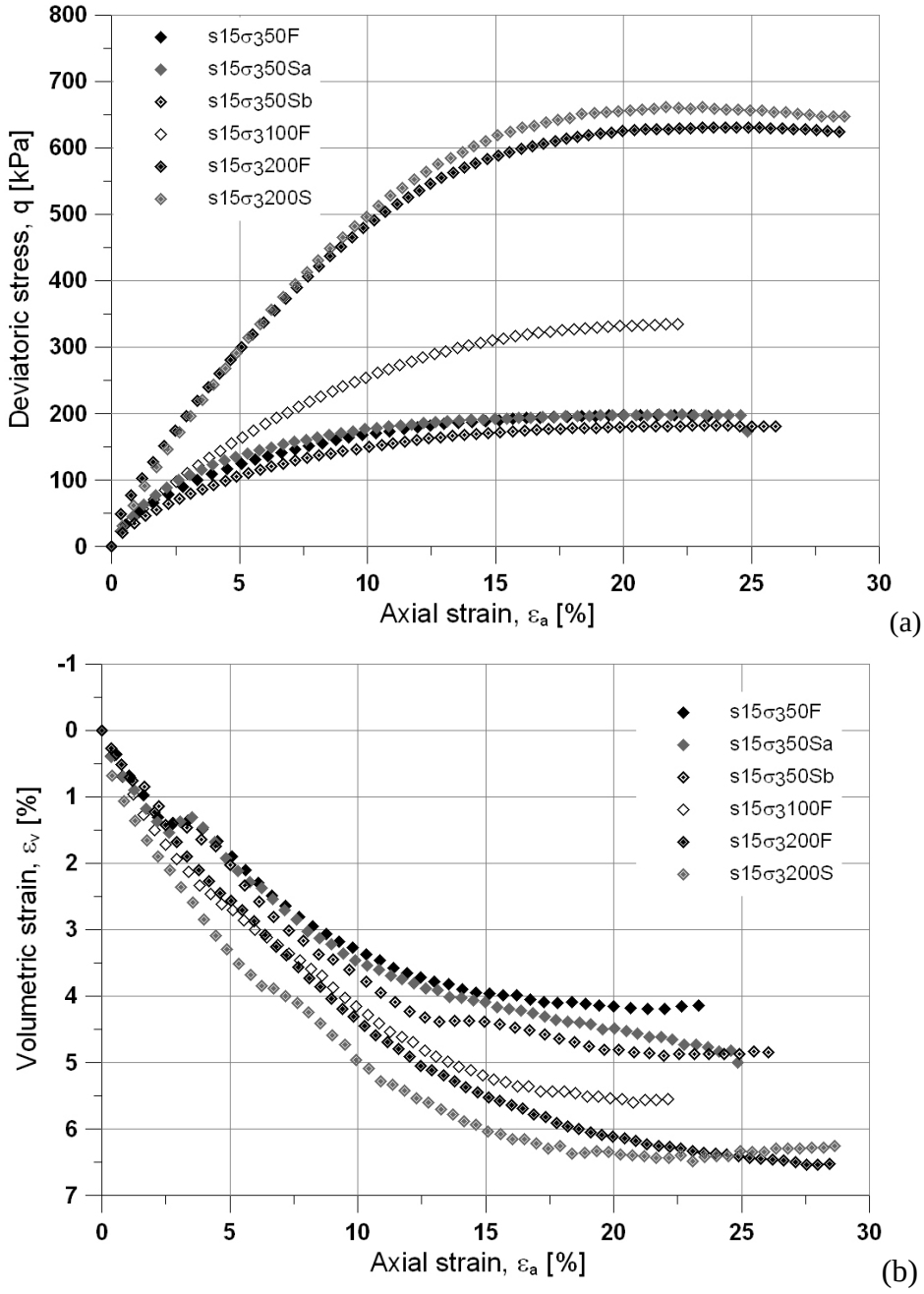

Figure 7.9. Drained shearing tests at a constant suction of 15 kPa and at different effective confining pressure (σ_3' = 50, 100 and 200 kPa): axial strain ε_a versus (a) deviatoric stress q and (b) volumetric strain ε_v.

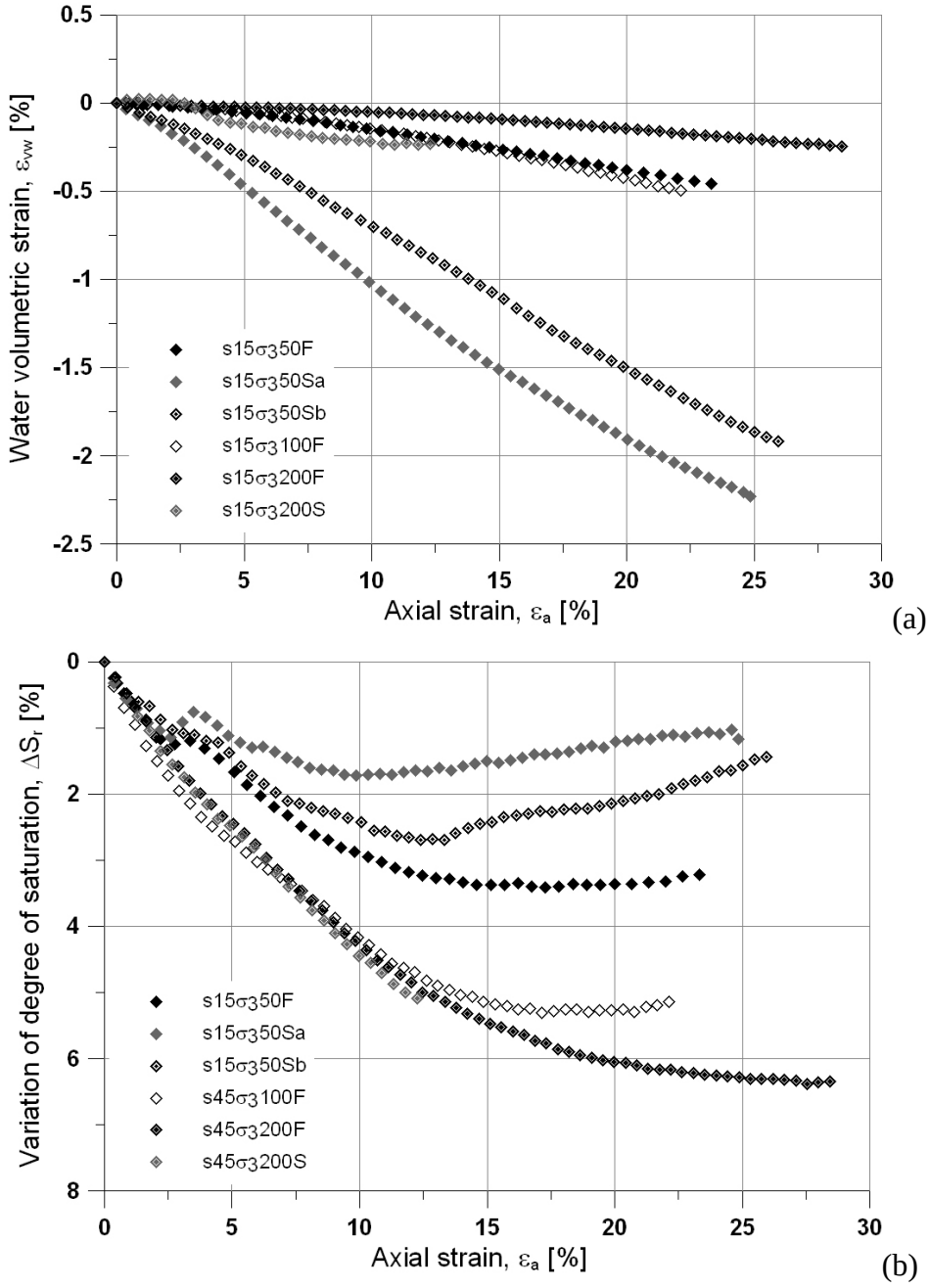

Figure 7.10. Drained shearing tests at a constant suction of 15 kPa and at different effective confining pressure (σ_3' = 50, 100 and 200 kPa): axial strain ε_a versus (a) water volumetric strain ε_{vw} and (b) variation of degree of saturation S_r.

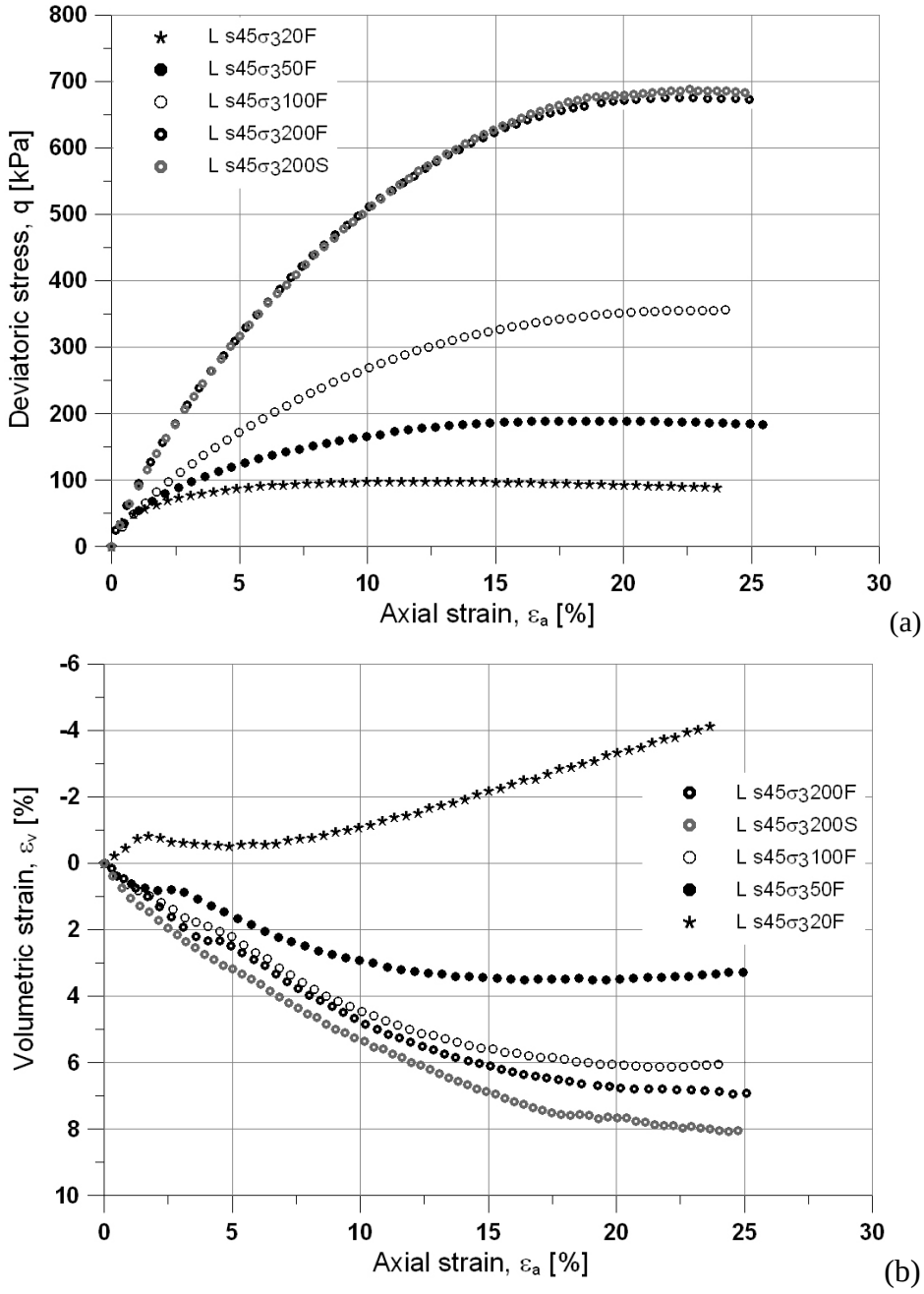

Figure 7.11. Drained shearing tests at a constant suction of 45 kPa and at different effective confining pressure (σ_3' = 20, 50, 100 and 200 kPa): axial strain ε_a versus (a) deviatoric stress q and (b) volumetric strain ε_v.

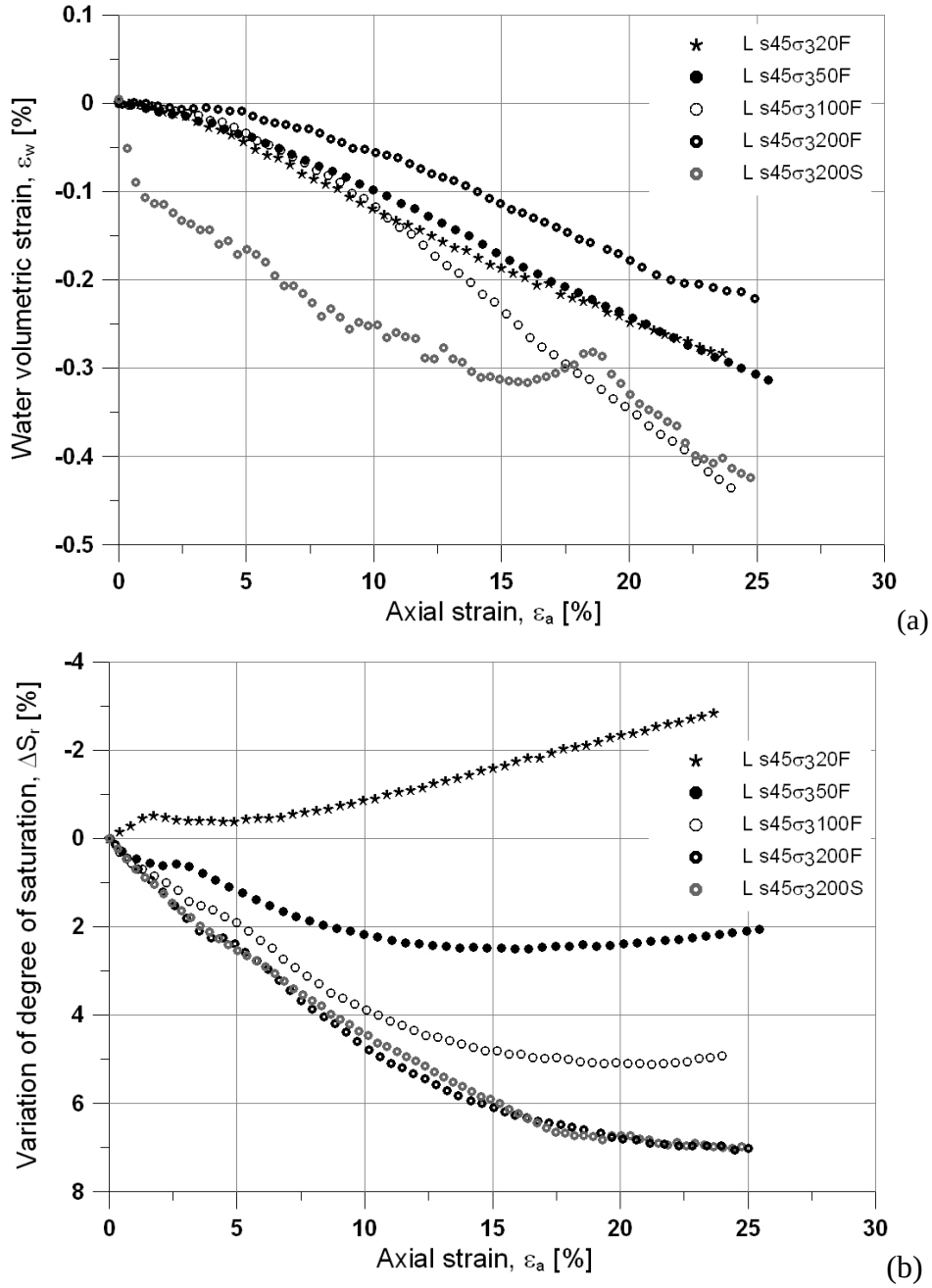

Figure 7.12. Drained shearing tests at a constant suction of 45 kPa and at different effective confining pressure (σ_3' = 20, 50, 100 and 200 kPa): axial strain ε_a versus (a) water volumetric strain ε_{vw} and (b) variation of degree of saturation S_r.

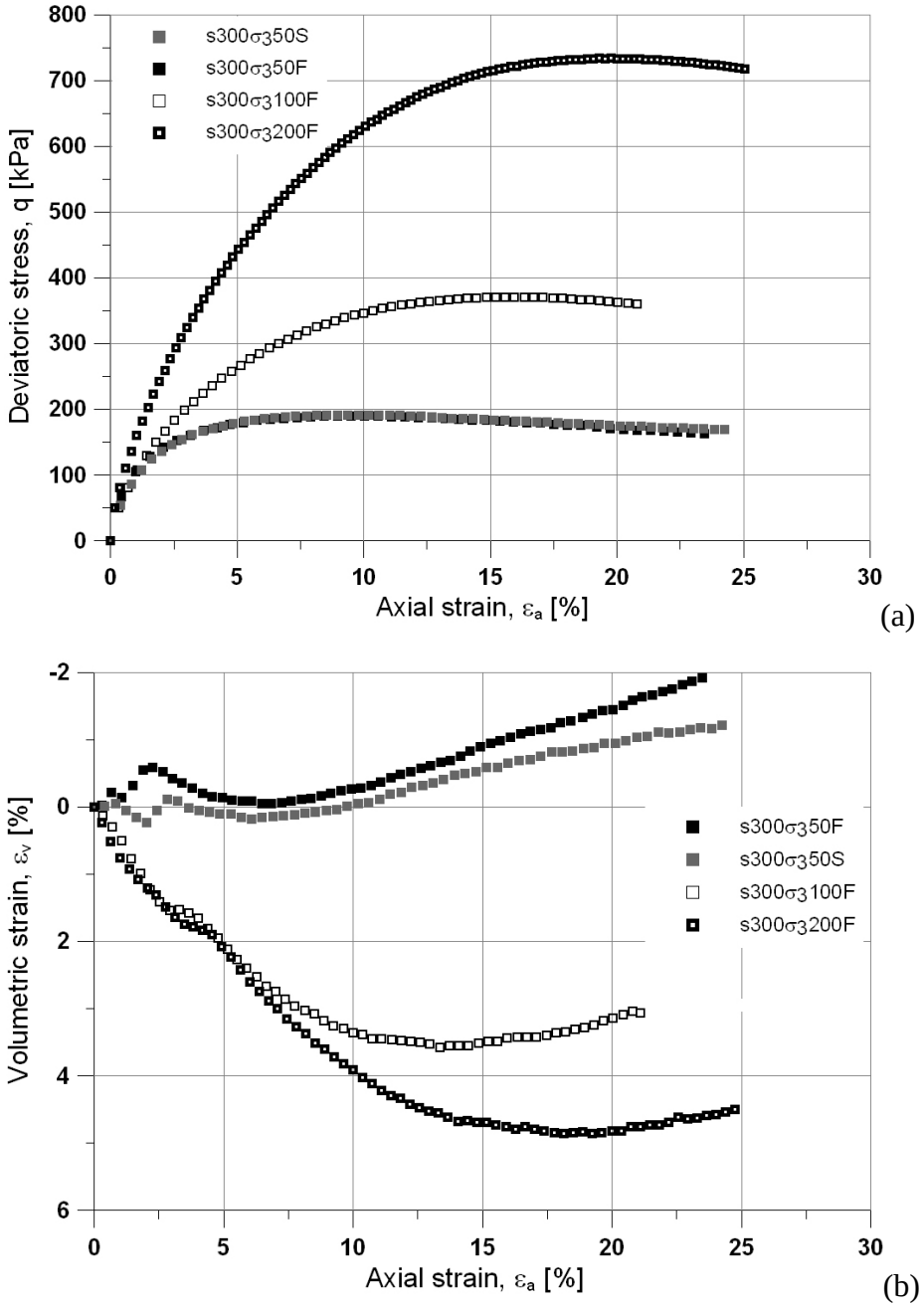

Figure 7.13. Drained shearing tests at a constant suction of 300 kPa and at different effective confining pressure (σ_3' = 50, 100 and 200 kPa): axial strain ε_a versus (a) deviatoric stress q and (b) volumetric strain ε_v.

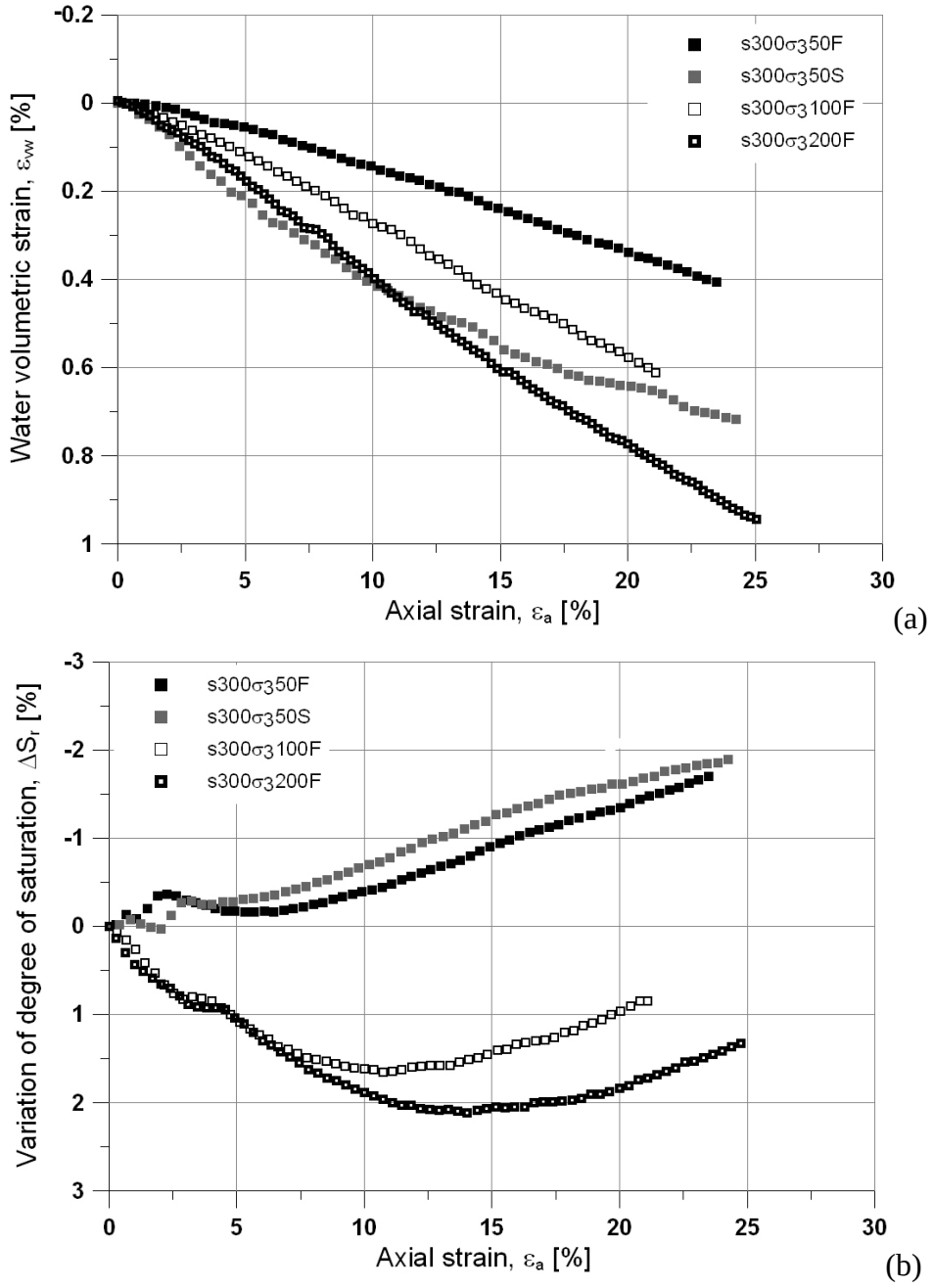

Figure 7.14. Drained shearing tests at a constant suction of 300 kPa and at different effective confining pressure (σ_3' = 50, 100 and 200 kPa): axial strain ε_a versus (a) water volumetric strain ε_{vw} and (b) variation of degree of saturation S_r.

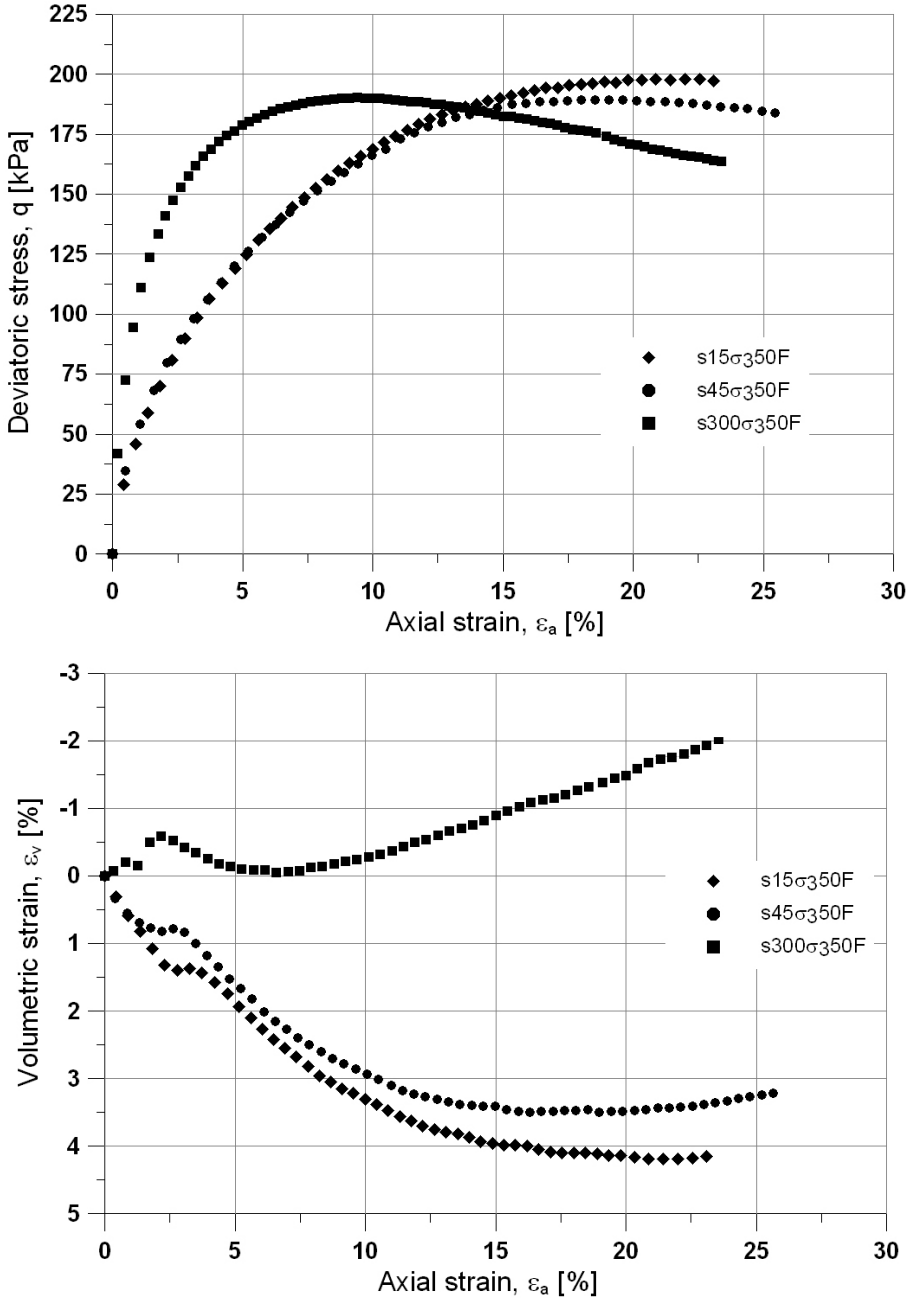

Figure 7.15. Drained shearing tests at effective confining pressure σ_3' = 50 and at different constant suction (s = 15, 45,300 kPa): axial strain ε_a versus (a) deviatoric stress q and (b) volumetric strain ε_v.

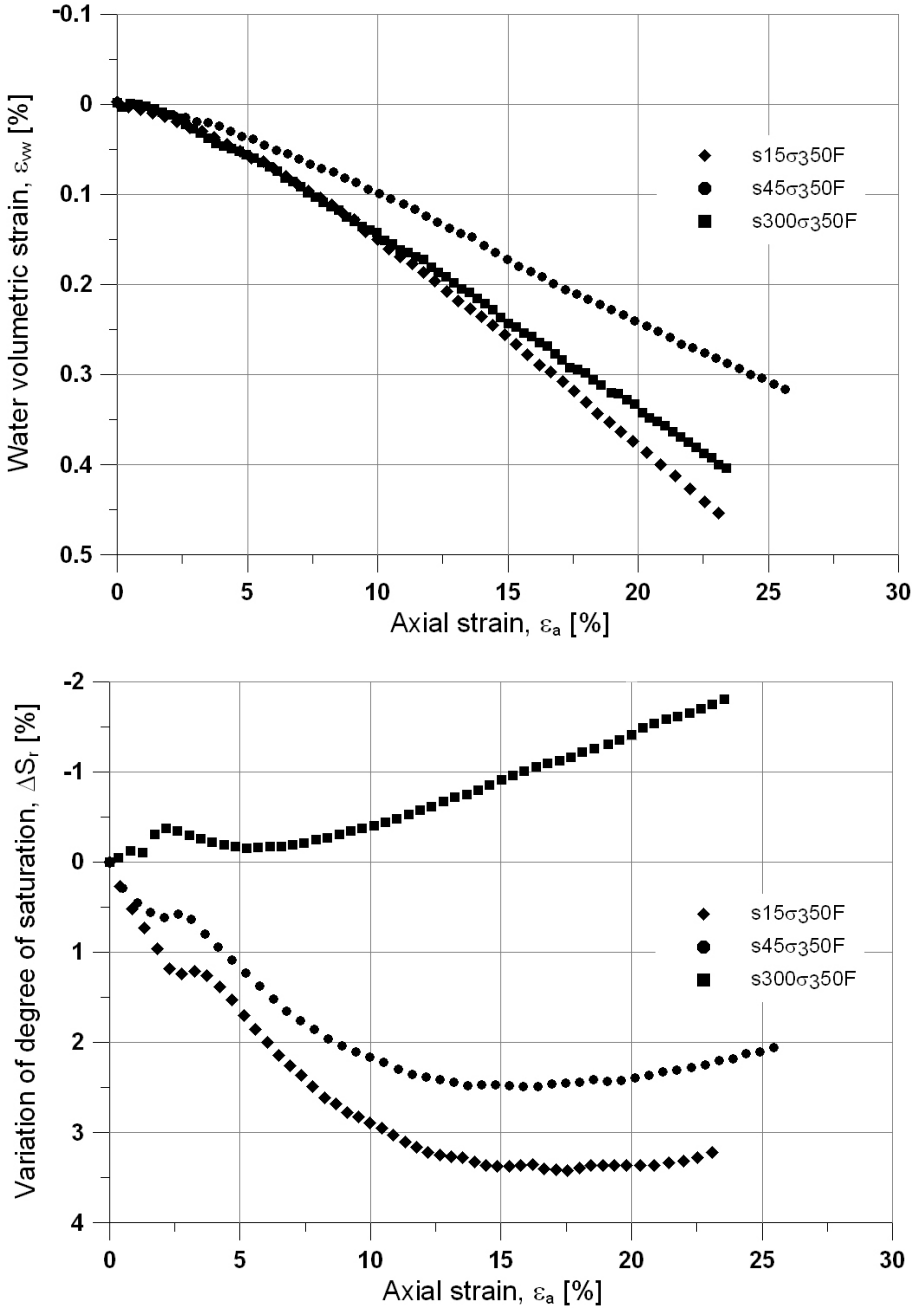

Figure 7.16. Drained shearing tests at effective confining pressure σ_3' = 50 and at different constant suction (s = 15, 45,300 kPa): axial strain ε_a versus (a) water volumetric strain ε_{vw} and (b) variation of degree of saturation S_r.

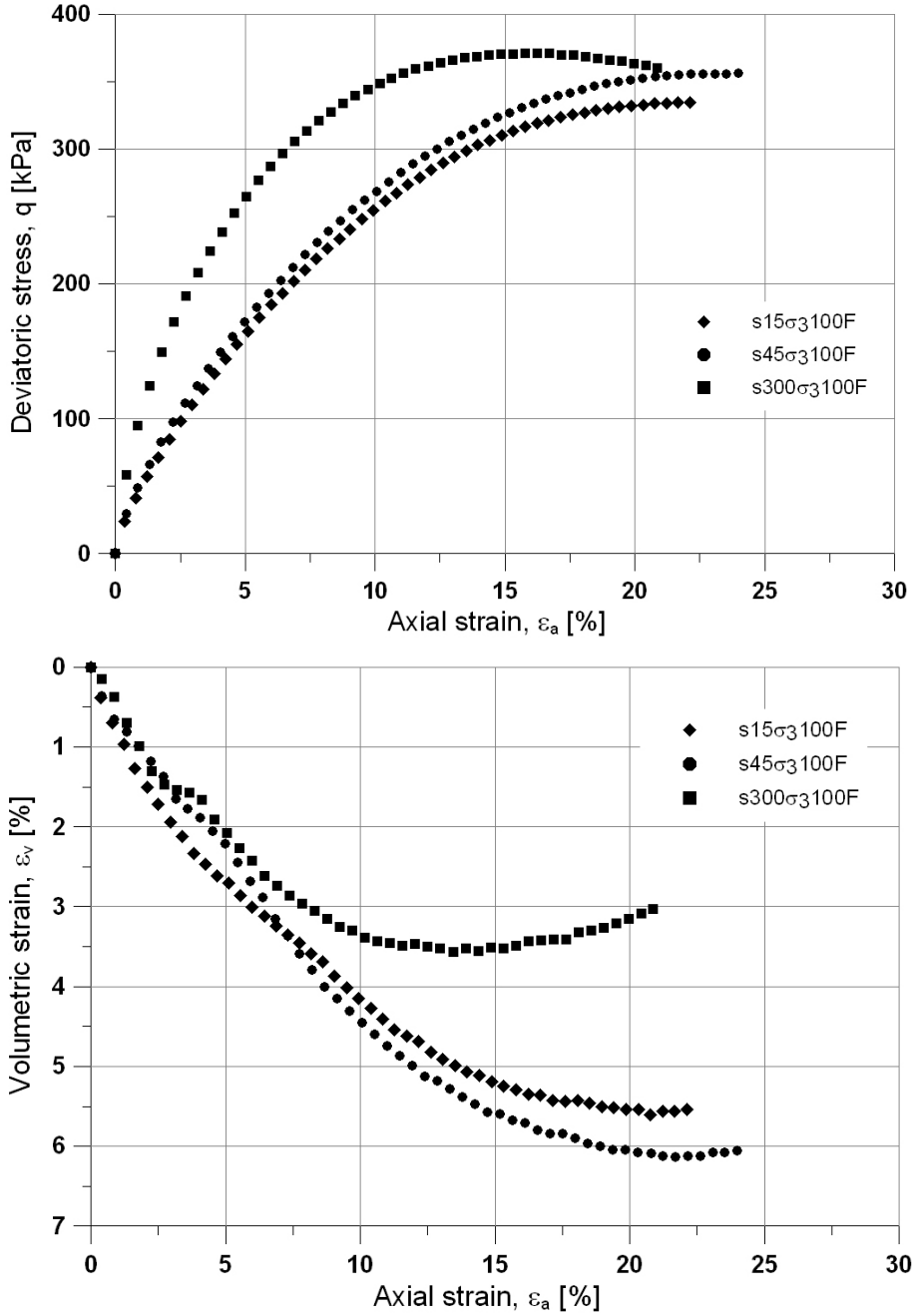

Figure 7.17. Drained shearing tests at effective confining pressure σ_3' = 100 and at different constant suction (s = 15, 45,300 kPa): axial strain ε_a versus (a) deviatoric stress q and (b) volumetric strain ε_v.

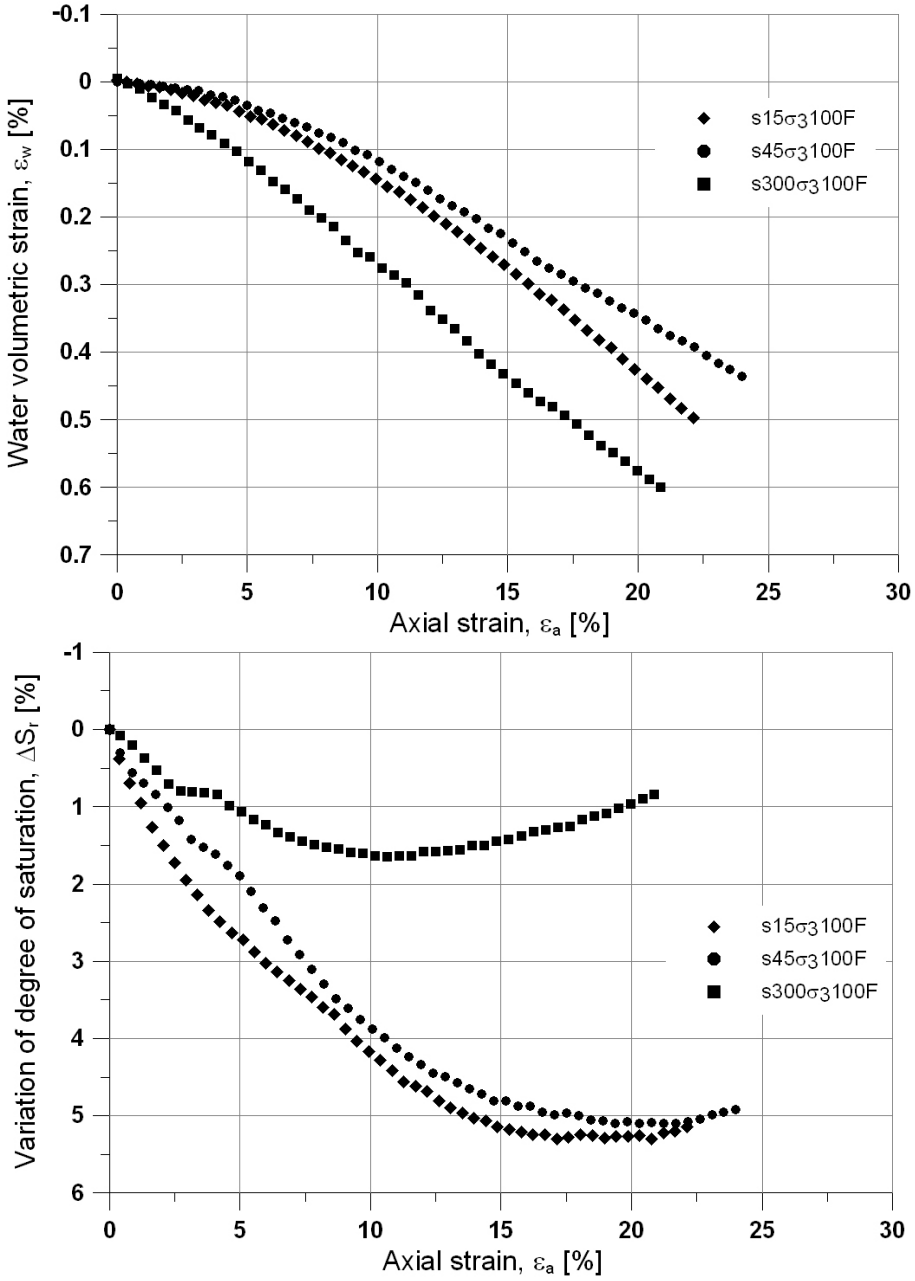

Figure 7.18. Drained shearing tests at effective confining pressure σ_3' = 100 and at different constant suction (s = 15, 45,300 kPa): axial strain ε_a versus (a) water volumetric strain ε_{vw} and (b) variation of degree of saturation S_r.

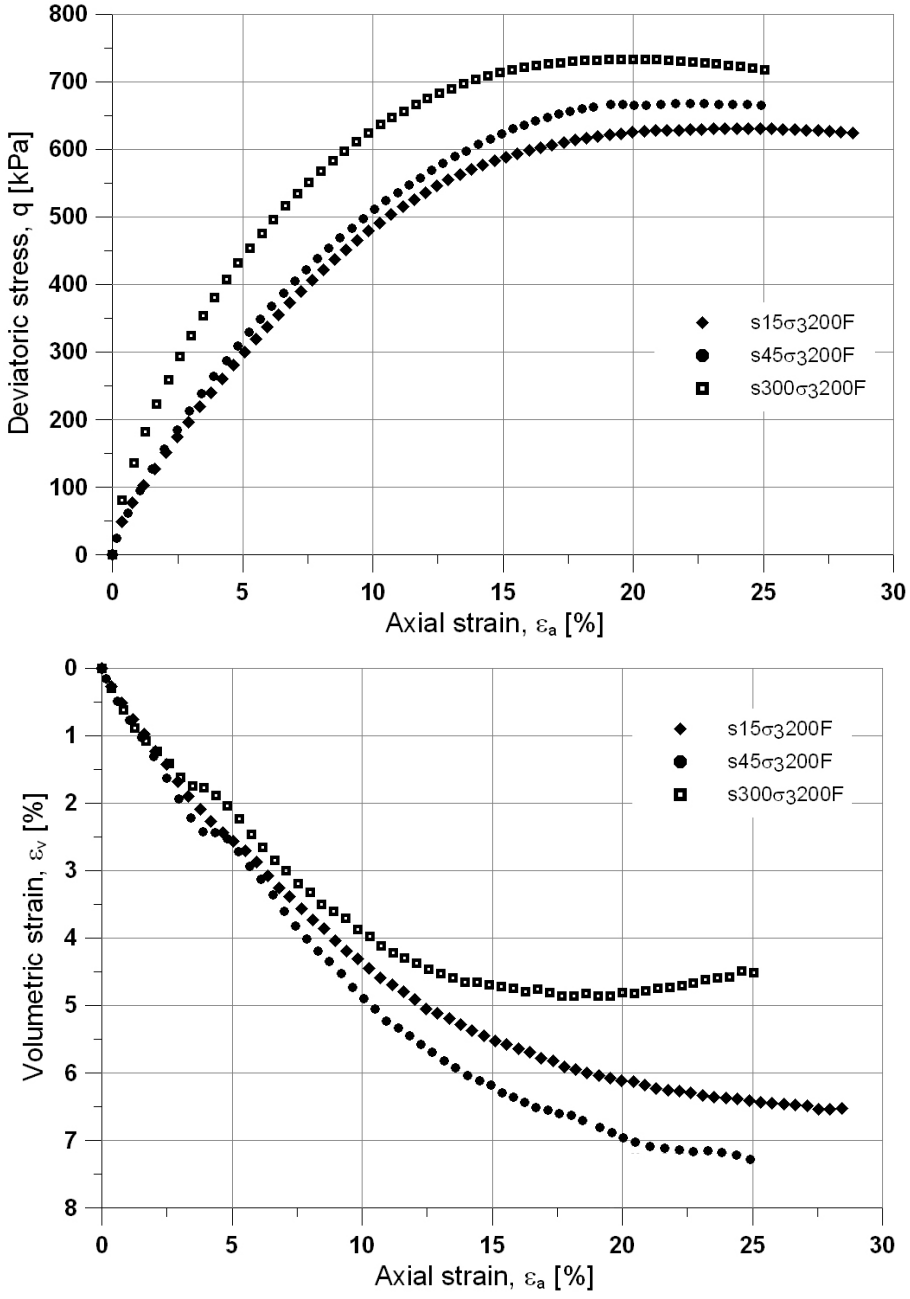

Figure 7.19. Drained shearing tests at effective confining pressure σ_3' = 200 and at different constant suction (s = 15, 45,300 kPa): axial strain ε_a versus (a) deviatoric stress q and (b) volumetric strain ε_v.

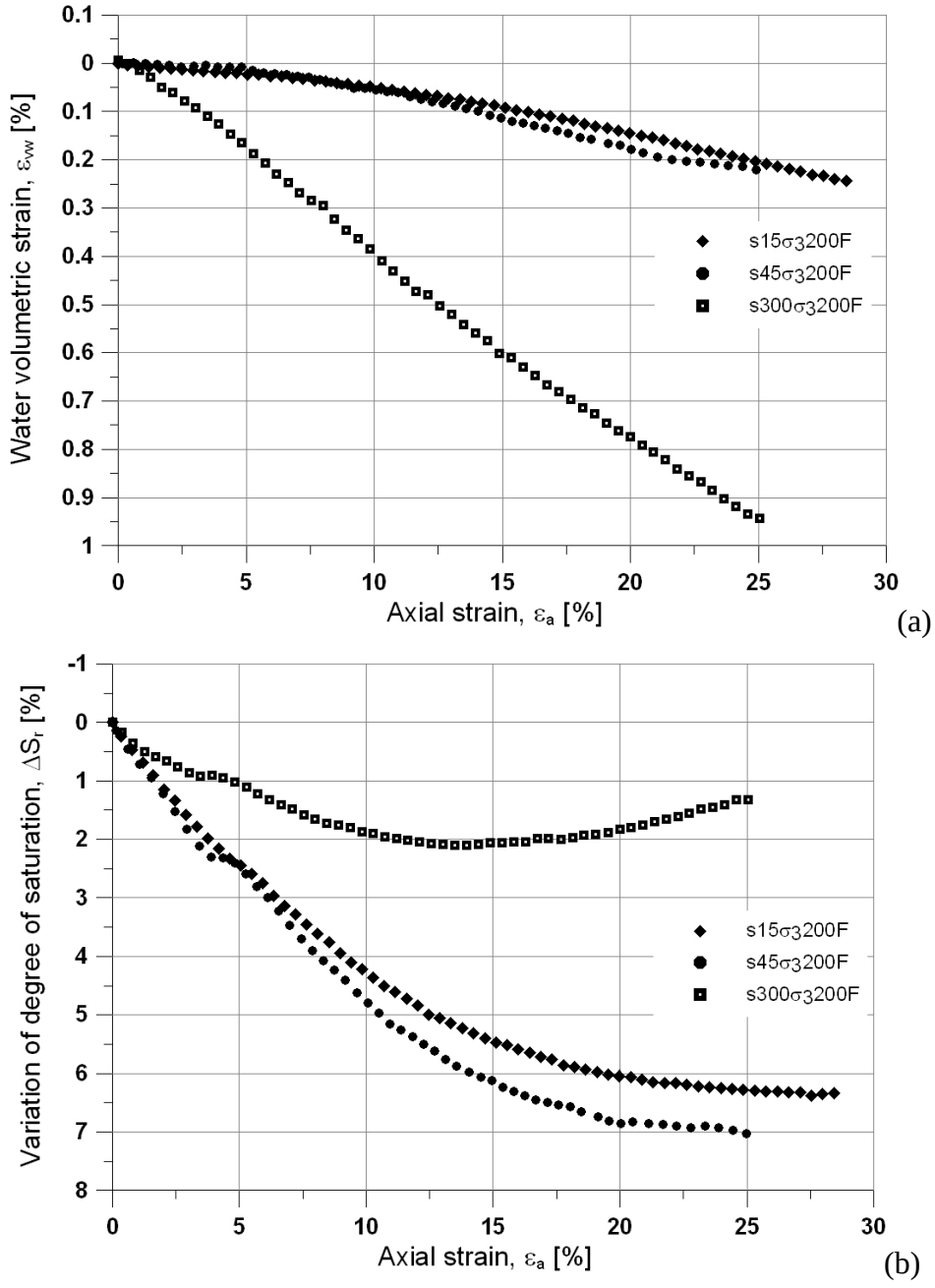

Figure 7.20. Drained shearing tests at effective confining pressure σ_3' = 200 and at different constant suction (s = 15, 45,300 kPa): axial strain ε_a versus (a) water volumetric strain ε_{vw} and (b) variation of degree of saturation S_r.

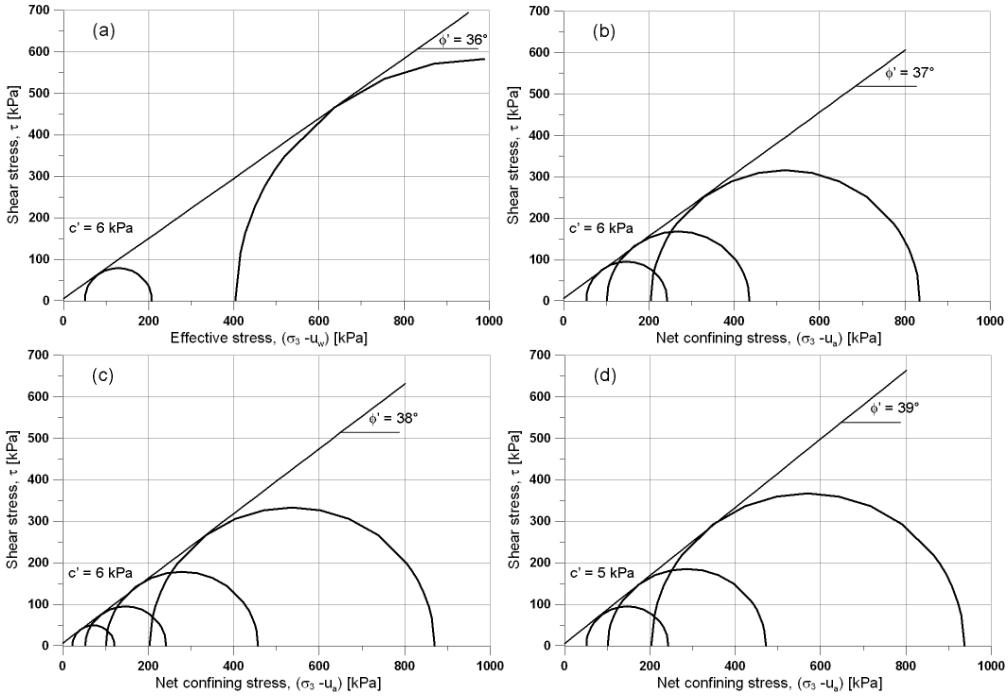

Figure 7.21. Mohr circles result of the CD triaxial tests under various matric suctions: (a) s = 0 kPa, (b) s = 15 kPa, (c) s = 45 kPa, and (d) s = 300 kPa.

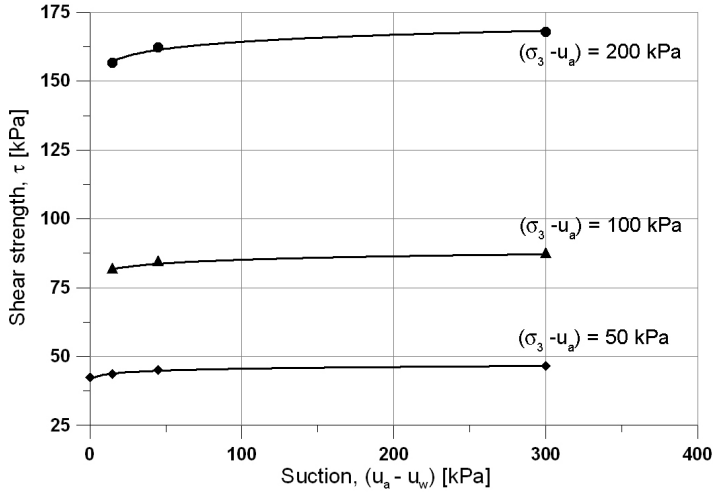

Figure 7.22. Variation of shear strength with matric suction.

Failure envelopes of the Cava dei Tirreni soil from the CD triaxial test results are presented in Figure 7.21. Each of the Mohr–Coulomb failure envelopes is plotted from CD triaxial tests at constant matric suction. The shear stresses at failure for the specimens used in the construction of the Mohr circles were determined by taking the peak values of the deviator stress in the stress–strain curves. The effective angle of internal friction, φ', increases whit suction. The cohesion intercepts of the failure envelopes on the zero net confining stress ($(\sigma_3 - u_a) = 0$) plane can be joined together to give a linear failure envelope with respect to matric suction and a φ^b value of 0°.

Shear strength τ are plotted as function of suction in Figure 7.22.

7.3 PORE-WATER PRESSURE MEASUREMENT DURING ISOTROPIC COMPRESSION TESTS ON CAVA DEI TIRRENI PYROCLASTIC SOILS

For the tests, half-size samples (38 mm in diameter and 38 mm in height) were obtained by moist tamping compaction method, as explained in Chapter 3. The samples were compacted following the technique described in Chapter 3, however, to obtain half-size samples (i.e. 38 cm in height) the soil was compacted in three layer of 12.7 mm each. Before the isotropic compression, predefined suction values were imposed. The experimental setup, the testing program, results and the conclusions obtained from suction equalization and pore-water pressure measurements are described in this section.

7.3.1 *Experimental setup*

Isotropic compression tests were conducted using the USPv2 triaxial apparatus. **Errore. L'origine riferimento non è stata trovata.** shows a scheme of the soil specimen mounted inside the inner cell. The USPv2 has a double drainage system to reduce the drainage path (h_{dr}). As explained in Chapter 4, the base platen and the top-cap incorporate a combination of two different porous disks: a peripheral annular porous stone and an internal HAEV ceramic disk (5 bar) connected to the pore-air and pore-water pressure lines, respectively.

Operating by such as suction control system, the air and water drainage occur from both top and bottom ends. This case of double drainage has symmetry about the mid-plane (point A in **Errore. L'origine riferimento non è stata trovata.**a) with all flow being upwards above this, and all flow being downwards below it. Then, the distance between point A and the ends represent the maximum drainage path (i.e., the longest path that any water particle has to travel to be expelled). The top and bottom half in **Errore. L'origine riferimento non è stata trovata.**a have identical

conditions with that of the case of single drainage represented in **Errore. L'origine riferimento non è stata trovata.**b. Hence, has been adopted the analysis for single drainage to monitoring the pore-water pressure changes at the middle height of sample (point A). The probe was used to measure pore-water pressure changes at the top of the specimen and the pore-water and pore-air pressures were controlled by the bottom, as indicated in **Errore. L'origine riferimento non è stata trovata.**b.

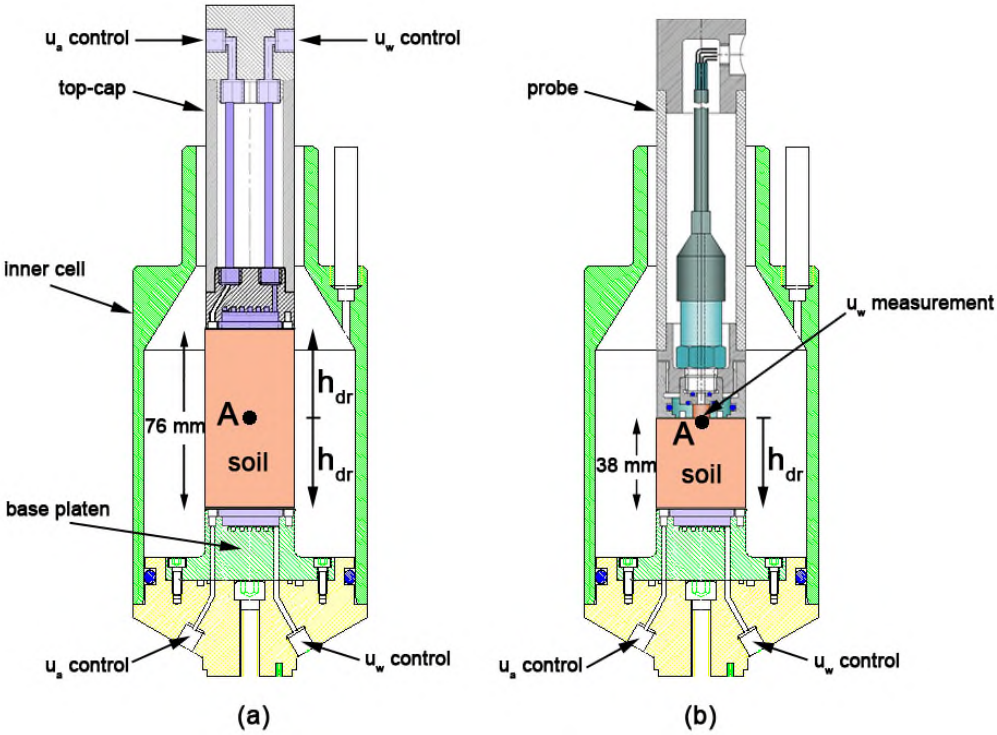

Figure 7.23. Scheme of the specimen setup: (a) original USPv2, (b) modified with the inclusion of probe.

7.3.2 *Suction equalization stage*

During set-up of triaxial device, the probe is placed in contact with the soil specimen. The contact between the ceramic disk of the probe and the specimen was improved by using a small amount of slurry. The initial pore-water pressure measured for the entire specimens are in a narrow range from -57 to -59 kPa, as shown in Figure 7.24. These results evidence the high reproducibility of the compaction method used and the precision of probe to measure negative pore-water pressure.

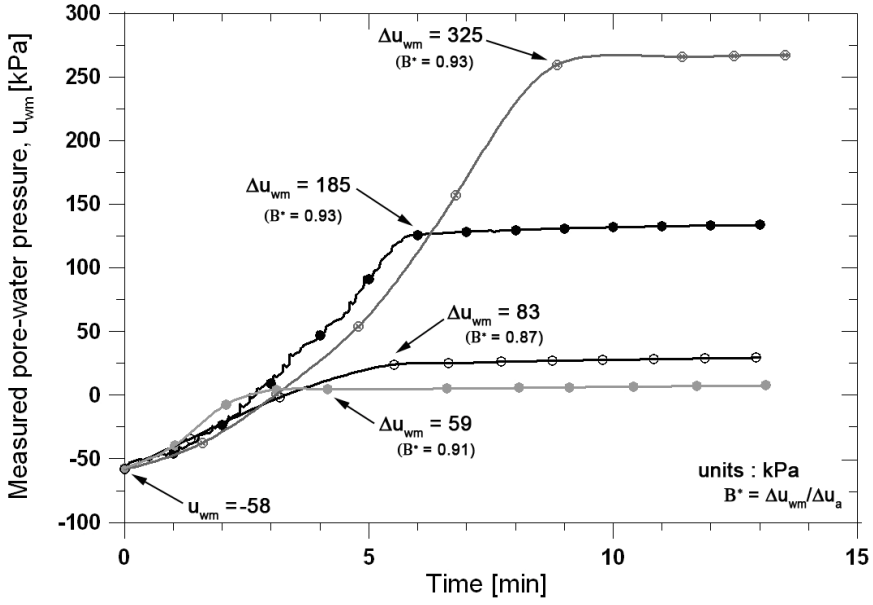

Figure 7.24. Results of pore-air pressure increment under pore-water undrained conditions.

The first stage of each test is the suction equilibration at imposed values. Axis translation technique was used to impose different suction values on similar specimens; this technique assumes that the increment of pore-water pressure (Δu_{wm}) is identical to a change in pore-air pressure (Δu_a). Figure 7.24 illustrates the response of the probe during pore-air pressure increment. The relationship between pore pressures variation is given by:

$$\Delta u_{wm} = B^* \times \Delta u_a \tag{8.1}$$

where B^* is the axis-translation pore pressure coefficient. As shown in Figure 7.24, for all the considered pore-air pressure changes (65, 95, 200 and 350 kPa), the measured B^* coefficient is around 0.93. This error is comparable to those obtained (0.94) by Guan & Fredlund (1997), Lourenço et al. (2006) and Lourenço et al. (2008).

Figure 7.25 shows the decaying curves of pore-water pressure caused by suction equilibration up to the imposed value (i.e. s= 300 kPa, where u_a = 350kPa and u_w = 50 kPa). Pore-water pressure follows the same path for most of the tests. The exception occurred for specimens s300$\sigma_3$350(128)h-b and s300$\sigma_3$350(128)h-c. These specimens exhibited a relatively delay compared with the pressure changes registered by specimens s300$\sigma_3$350(8)h, s300$\sigma_3$350(32)h and s300$\sigma_3$350(128)h-a. Generally, this phenomenon is attributed to the stiffness of the pore-water pressure measuring

system, which allows partial drainage of pore water from the sample (Whitman et al., 1961; Perlof et al., 1965). In this case, by using the same system, different response where obtained; then, the large time lag is ascribed to the bad saturation of probe. The maximum rigidity of the measuring system (i.e. probe) can be reached by pre-pressurization cycles in order to improve the saturation.

Nevertheless, as Perlof et al. (1965) observed, the influence of the stiffness of the measuring system is predominant in the early stages and its effect is negligible after some time.

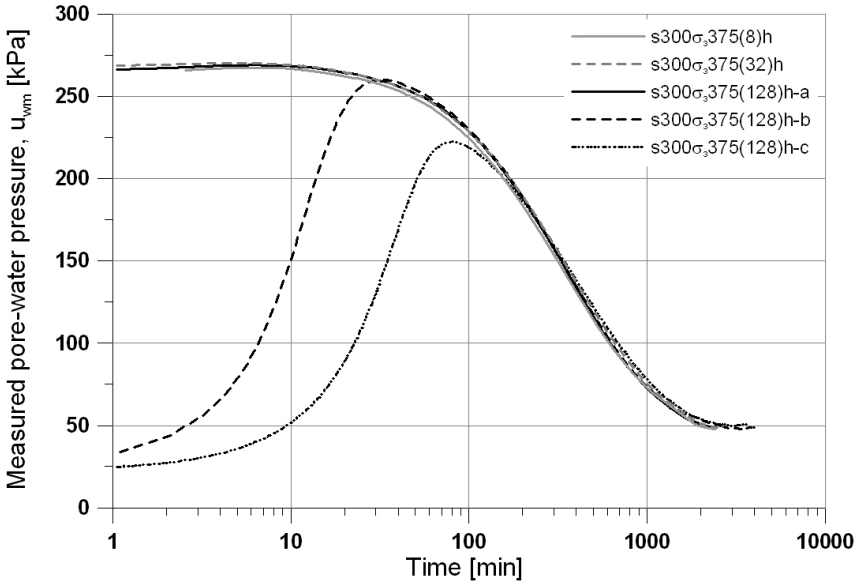

Figure 7.25. Influence of probe's stiffness on pore-water pressure monitoring.

The excess pore-water pressure dissipation is well represented by exponential decay equations. A quantity is said to be subject to exponential decay if it decreases at a rate proportional to its value. Symbolically, this can be expressed as the following differential equation, where N is the quantity and λ is a positive number called the decay constant.

$$\frac{dN}{dt} = -\lambda N \tag{8.2}$$

The solution to this equation is:

$$N(t) = N_0 e^{-\lambda t} \tag{8.3}$$

where: N(t) is the quantity at time t, and the constant of integration $N_0 = N(0)$ is the initial quantity, at time t = 0. Larger decay constants make the quantity vanish much more rapidly.

Under this form, the pore-water pressure reduction processes represented in Figure 7.26 is fitted by the following equation:

$$u_{wm} = 50 + 221 \times e^{-t/445.3} \tag{8.4}$$

Figure 7.26 and Figure 7.27 show a best-fit curve to the experimental data obtained for pore-water pressure reduction during drying process, using Eq. [8.4]. It can be seen that the exponential decay equation (i.e., Eq. [8.3]) fits experimental data very well over the entire pressure range from 271 to 50 kPa, therefore, can be considered a rigorous calibration experiment of a prove. Any deviation from the best-fit curve observed by prove will illustrate a measurement error of the tensiometer due to insufficient saturation. A comparison of the response of prove of differing degrees of saturation will illustrate the variation in the magnitude of errors associated with insufficient saturation.

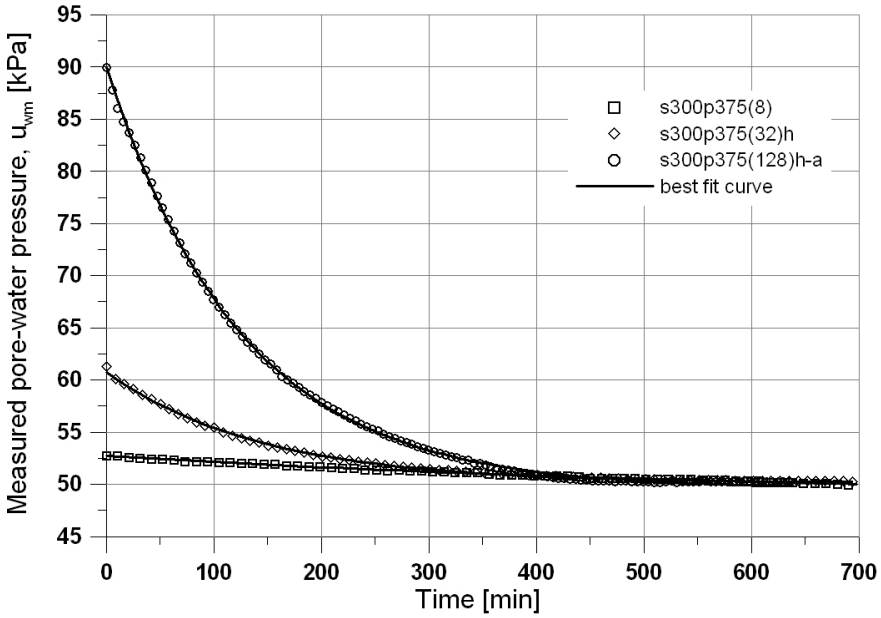

Figure 7.26. A best-fit curve to the experimental data of pore-water pressure reduction during drying.

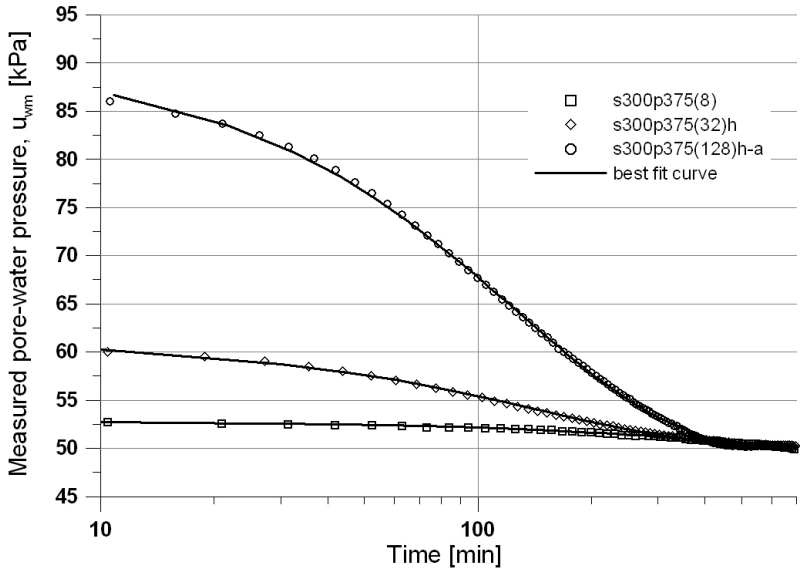

Figure 7.27. A best-fit curve to the experimental data of pore-water pressure reduction during drying.

All the equalization stages are run under a constant net confining stress ($\sigma_3 - u_a$) of 20 kPa and a deviator stress (q) of about 5 kPa. Water content changes are reported in Figure 7.28, similarly that for full-size samples, the results shows that the suction value after compaction is about 45 kPa, for suction values less than this value (i.e. 5 and 15 kPa) a flow of water towards the soil occurs (i.e. water content increase) and for suction values higher than 45 kPa (i.e. 100, 200 and 300 kPa) the water flows in the opposite direction (i.e. water content decrease). A comparison between full-size samples (black lines) and half-size samples (gray lines) during the equalization stages is presented in Figure 7.29.

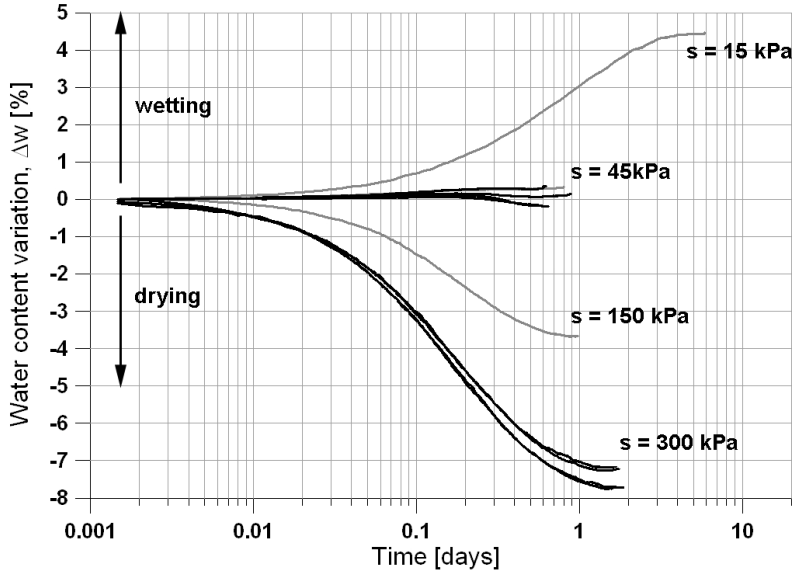

Figure 7.28. Water content changes of $1h_{dr}$ samples during the equalization stages.

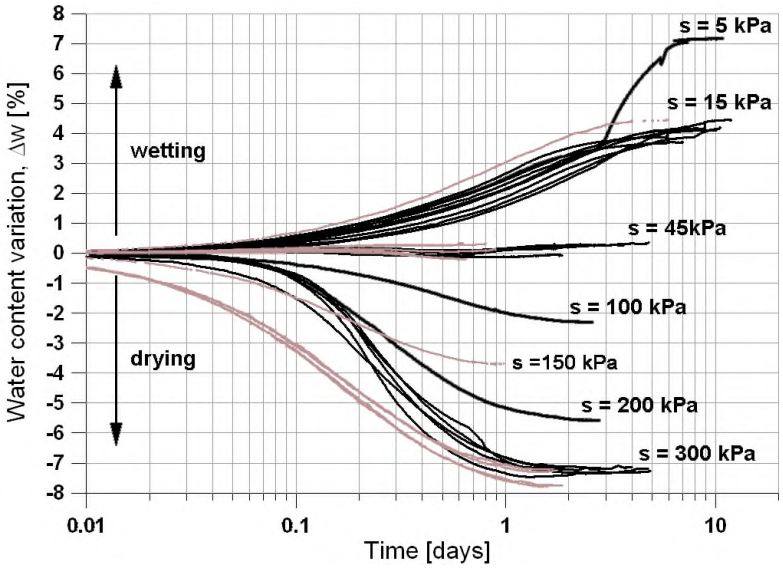

Figure 7.29. Comparison between full-size samples (black lines) and half-size samples (gray lines) during the equalization stages.

7.3.3 *Isotropic compression*

The variation of measured pore-water pressure with rate of loading (8, 32 and 128 kPa), obtained from isotropic compression test at a constant suction of 300 kPa, is presented in Figure 7.30. As can be seen, the measured pore-water pressure increases as net confining stress progressed. Is evident the relationship between the applied rate of loading and the magnitude of increase in measured pore-water pressure during compression, as indicated by differences in measured pore-water pressure between tests s300$\sigma_3$375(8)h, s300$\sigma_3$375(32)h and s300$\sigma_3$375(128)h-a.

Errore. L'origine riferimento non è stata trovata. shows that the build-up of the measured pore-water pressures decreased as the compression progressed, as seen in the continuing decrease of the gradients of the graphs. It is also noted that, except for specimen s300s375(128)h-a, the pore-water pressures started to decrease towards the end of the tests, as shown in **Errore. L'origine riferimento non è stata trovata.** for specimens s300s375(8)h and s300s375(32)h.

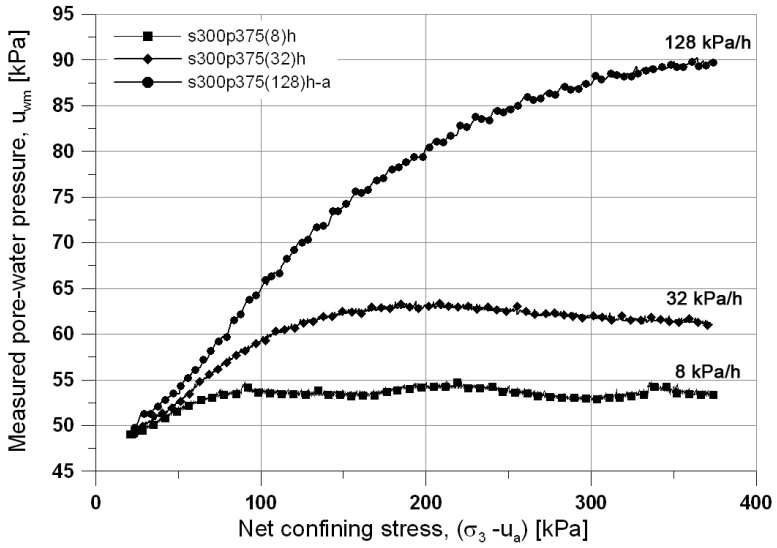

Figure 7.30. Variation of measured pore-water pressure with rate of loading (8, 32 and 128 kPa), obtained from isotropic compression test at a constant suction of 300 kPa.

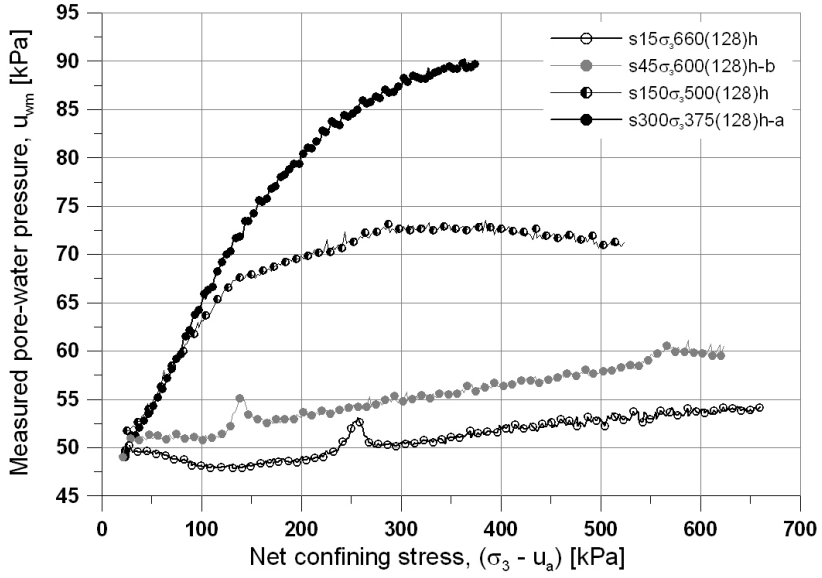

Figure 7.31. Variation of measured pore-water pressure with suction (15, 45, 150 and 300 kPa), obtained from isotropic compression test at a loading rate of 128 kPa/h.

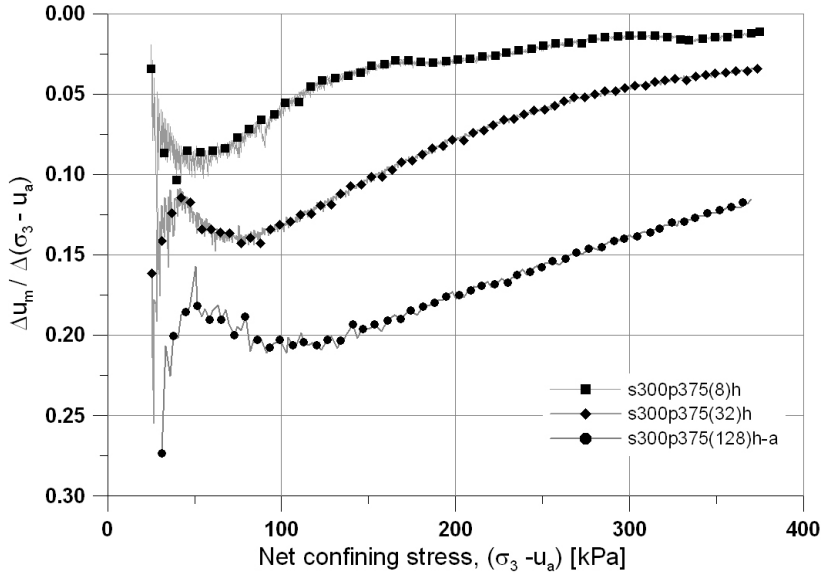

Figure 7.32. Variation of measured pore-water pressure with rate of loading (8, 32 and 128 kPa), obtained from isotropic compression test at a constant suction of 300 kPa.

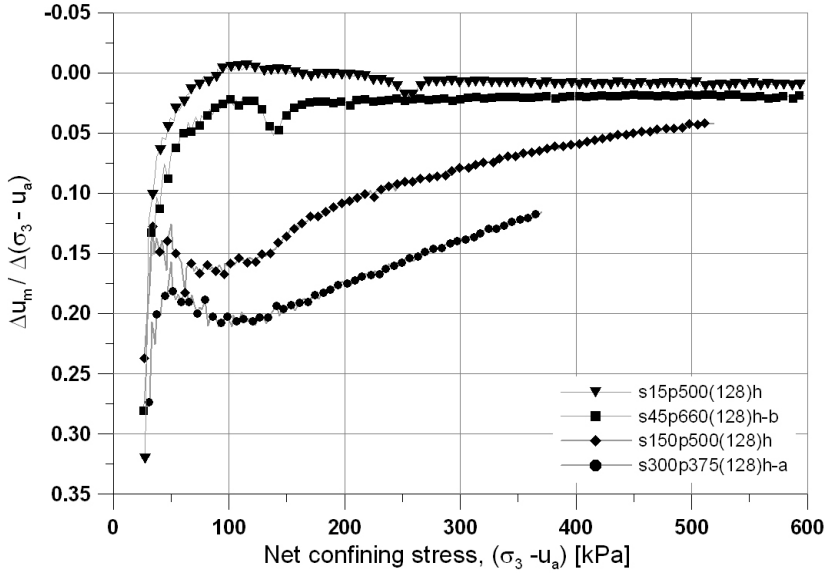

Figure 7.33. Variation of measured pore-water pressure with suction (15, 45, 150 and 300 kPa), obtained from isotropic compression test at a loading rate of 128 kPa/h.

After the end of test, to dismantle the cell, the applied pressures (i.e. pore-air, pore-water and cell pressure) were reduced to zero. The pressures were rapidly reduced under drained conditions for the pore-air phase and undrained conditions for the pore-water phase. Based on the axis translation technique, if the pore-air pressure is reduced at atmospheric value (u_a = 0 kPa) is expected that the pore-water pressure decrease in the same magnitude that pore-air pressure reduction. Such decrease of pore-water pressure was measured by the probe and compared with the change of pore-air pressure while net confining stress ($\sigma_3 - u_a$) is maintained roughly constant; the results are shown in Figure 7.34. No cavitation was observed during the entire unloading process and also the capacity of prove to sustain high negative pore-water pressures (-300 kPa) was verified. A good agreement is observed between pore-air and pore-water pressure changes.

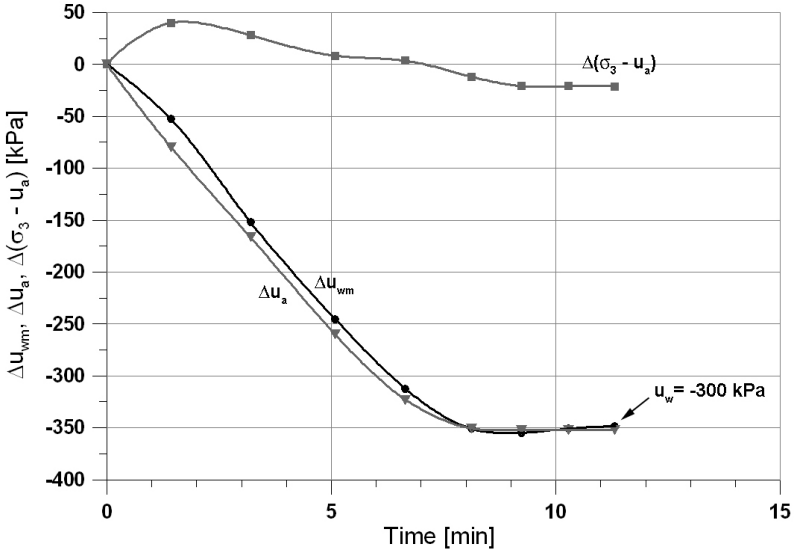

Figure 7.34. UNINA high capacity tensiometer.

REFERENCES

Airò Farulla, C. & Ferrari, A. 2005. Controlled suction oedometer tests: analysis of some experimental aspects. Proceedings of an international symposium on advanced experimental unsaturated soil mechanics EXPERUS 2005. Trento, Italy, June 27-29, 2005. pp 43-48.

Agus, S. S., Leong, E. C. & Rahardjo, H. 2000. A Triaxial Permeameter for Unsaturated Soils. Unsaturated Soils for Asia, Proceedings, The Asian Conference on Unsaturated Soils, UNSAT-ASIA, Singapore, Balkema, Rotterdam, pp. 365–370.

Agus, S.S. and Schanz, T. 2005. an investigation into hydro-mechanical behaviour of an expansive soil using axis-translation and vapor equilibrium techniques. Advanced experimental unsaturated soil mechanics –Experus 2005. Trento, Italy, June 27-29, pp 53-59.

Aversa, S. & Nicotera, M. 2002. A triaxial and oedometer apparatus for testing unsaturated soils. Géotech Testing J. 25(1):3–15.

Bishop, A.W. & Donald, I. B. 1961. The experimental study of partly saturated soils in the triaxial apparatus. Proceedings, Fifth International Conference on Soil Mechanics and Foundation Engineering, Paris, Vol.1:13–21.

De Gennaro, V., Cui, Y.J., Delage, P. & De Laure E. 2002. On the use of high air entry value porous stones for suction control and related problems. En J.F.T. Jucá, T.M.P. de Campos & F.A.M. Marinho, *Unsaturated soils*, Proceedings of the third international conference on unsaturated soils, UNSAT 2002, 10-13 marzo, Recife, Brasil, pp. 435-440. Lisse: Balkema.

Escario, V., Saez, J. 1986. The shear strength of partly saturated soils. Geotechnique 36(3):453–6.

Fredlund, D.G., Morgenstern, N.R., Widger, R.A. 1978. The shear strength of unsaturated soils. Canadian Geotechnical Journal; 15:313–21.

Fredlund, D.G., Rahardjo, H., Gan, J.K.M. 1987. Nonlinearity of strength envelope for unsaturated soils. Proc 6th Int Conf Expansive Soils, New Delhi; 1:49–54.

Klug, C., Cashman, K. & Bacon, C. 2002. Structure and physical characteristics of pumice from the climactic eruption of Mount Mazama (Crater Lake), Oregon. Bulletin of Volcanology, 64(7): 486-501.

Kung, T.C. 2007. Equipment and testing procedures for small strain triaxial tests. Journal of the Chinese Institute of Engineers, Vol. 30 (4): 579-591.

Matsushita, M., Tatsuoka, F., Koseki, J., Cazacliu B., Benedetto, H., and Yasin, S.J.M. 1999. Time effects on the pre-peak deformation properties of sands. Prefailure Deformation Characteristics of geomaterials, M. Jamiolkowski, R. Lancellotta, and D. LoPresti, eds., Balkema, Rotterdam, The Netherlands, 681–689.

Machado, S.L. and Vilar, O.M. 1998. Unsaturated shear strength: laboratory tests and predictions. Soil and Rock Journal, vol 21(2):65-78.

Nuth, M. and Laloui, L. 2008. Effective stress concept in unsaturated soils: Clarification and validation of a unified framework. Int. J. Numer. Anal. Meth. Geomech; 32:771–801.

Rampino, C., Mancuso, C. & Vinale, F. 1999. Laboratory testing on an unsaturated soil: equipment, procedures, and first experimental results. Can. Geotech. J. 36: 1–12.

Rojas, J.C., Zingariello, M.C., Mancuso, C. & Vinale, F. 2006. Un apparecchio per prove di ritenzione idrica a suzione e carico controllati. Incontro Annuale dei Ricercatori di Geotecnica 2006 - IARG 2006. Pisa, Italy: June 26-28.

Romero, E. 1999. Characterisation and thermo-hydromechanical behaviour of unsaturated Boom clay: an experimental study. Ph D thesis, Universitat Politecnica de Catalunya, Spain.

Tekinsoy, M.A., Kayadelen C., Keskin M.S., and Soylemez M. (2004). An equation for predicting shear strength envelope with respect to matric suction. Computers and Geotechnics 31: 589–593.

Vanapalli, S.K., Fredlund, D.G., Pufahi, D.E., and Clifton, A.W. 1996. Model for the prediction of shear strength with respect to soil suction. Canadian Geotechnical Journal, Vol. 3(3):379–92.

Wright, H. M.; Roberts, J.; Cashman, K. V. (2005). Pore structure of pumice: comparison between laboratory measurements and X-Ray tomographic image analysis. American Geophysical Union, Fall Meeting 2005, abstract #V42A-06.

Yin, Z. Z. 1998, Settlement and Consolidation of Soil Mass. China Electric Publication House.

Zhang, L. & Chen, Q. (2005). Predicting Bimodal Soil–Water Characteristic Curves. Journal of Geotechnical and Geoenvironmental Engineering, 131(5): 666-670.

Baldi G., and Nova R. 1984. Membrane penetration effects in triaxial testing. Journal of Geotechnical Engineering, ASCE. Vol.110(3): 403–420.

Carraro J.A. and Salgado R. 2004. Mechanical behaviour of non-textbook soils (Literature Review).

Chen HW and van Zyl DJA 1988. Shear strength and volume change behaviour of copper tailings under saturated conditions. Hydraulic fill structures. Edited by

DJA Van Zyl and SG Vick. American Society of Civil Engineers, Geotechnical Special Publication 21, pp. 430–451.

Chu J, Leong W K and Loke WL 2003. Discussion of “Defining an appropriate steady state line for Merriespruit gold tailings”. Can. Geotech. J. 40: 484–486.

Dyvik R and Hoeg K 1999. Comparison of tests on undisturbed and reconstituted silt and silty sand. Proceedings of the International Workshop on the Physics and Mechanics of Soil Liquefaction, Baltimore, September 1998.

El-Sohby M.A. and Andrawakes, K.Z. 1972. Deformation characteristics of granular material under hydrostatic compression. Can. Geotech. J. Vol. 9(9): 338-350.

Fourie A.B. and Papageorgiou G. 2001. Defining an appropriate steady state line for Merriespruit gold tailings. Can. Geotech. J. 38: 695-706.

Fourie A.B. and Papageorgiou G. 2003. Reply to the discussion by J. Chu, W.K. Leong, and W.L. Loke on “Defining an appropriate steady state line for Merriespruit gold tailings”. Can. Geotech. J. 40: 487-488.

Frost J.D., and Park J.Y. 2003. A critical assessment of the moist tamping technique. J. Geotechnical Testing. Vol. 26, No.1: 57-70.

Frydman S., Zeitlan J.G., and Alpan I. 1973. The membrane effect in triaxial testing of granular soils. Journal of Testing and Evaluation, JTEVA. Vol.1(1): 37–41.

Ishihara, K. 1993. Liquefaction and flow failure during earthquakes. Geotechnique, Vol. 43, No. 3:351-415.

Kiekbusch M., and Schuppener B. 1977. Membrane penetration and its effect on pore pressures. Journal of the Geotechnical Engineering Division, ASCE. Vol.103(11): 1267–1279.

Kuerbis R. and Vaid Y.P. 1998. Sand sample preparation – the slurry deposition method. Soils and Foundations Vol. 28, No. 4: 107-118.

Lauer C. and Engel J. 2005. Investigations on the unsaturated stress-strain behaviour and on the SWCC of Houston Sand in a double-walled triaxial cell. Advanced experimental unsaturated soil mechanics. Pp: 185-191. Tarantino, Romero and Cui (eds.). Taylor and Francis Group, London.

Nicholson P.G., Seed R.B., and Anwar H.A. 1993. Elimination of membrane compliance in undrained triaxial testing. I. Measurement and evaluation. Can. Geotech. J. Vol. 30(5):727–738.

Papadimitriou A.G., Dafalias Y.F., and Yoshine M. (2005). Plasticity modelling of the effect of sample preparation method on sand response. Soils and foundations. Vol. 45(2): 109-123.

Raju V.S., and Venkatramana K. 1980. Undrained triaxial tests to assess liquefaction potential of sands — effects of membrane penetration. In Proceedings of the International Symposium on Soils under Cyclic Transient loading, Rotterdam, Vol. 2: 483–494.

Sivathayalan S. and Vaid Y.P. (1998) Truly undrained response of granular soils with no membrane-penetration effects. Can. Geotech. J. Vol. 35:730-739.

Schomburg W. K., Rummler Z., Shao P., Wulff K. and Xie L. 2004. The design of metal strain gauges on diaphragms. Journal of micromechanics and microengineering. Vol. 14: 1101-1108.

Take and Bolton (2002). Phillips, In Guo and Popescu, (eds.) Physical Modelling in Geotechnics ICPMG 2002, 297-302, Balkema.

Timoshenko S. and Woinowsky-Krieger S. 1959. Theory of plates and Ssells 2nd edn. New York: McGraw-Hill.

Tombolato S., Tarantino A., and Mongiovi L. 2005. Investigatine water retention characteristics upon wetting paths using water-undrained compression tests. Advanced experimental unsaturated soil mechanics. Pp: 397-400. Tarantino, Romero and Cui (eds.). Taylor and Francis Group, London.

Vaid Y.P., and Negussey D. 1984. A critical assessment of membrane penetration in the triaxial test. ASTM Geotechnical Testing Journal, Vol. 7(2): 70–76.

Vaid Y.P., Sivathayalan S., and Stedman D. 1999. Influence of specimen-reconsituting ethod on the undrained response of sand. Geotechnical Tesing Journal, GTJODJ, Vol. 22, No. 3: 187-195.

Vaughan PR 1997. Panel discussion: Sedimentation of tailings. Proceedings of the14th International Conference on Soil Mechanics and Foundation Engineering, Hamburg, Germany. Vol. 4: 2561–2562.

Villar M.V., Matin P.L., and Lloret, A. 2005. Determination of water retention curves of two bentonites at high temperature. Advanced experimental unsaturated soil mechanics. Pp: 77-82. Tarantino, Romero and Cui (eds.). Taylor and Francis Group, London.

Vishay® 2005a. Design considerations for diaphragm pressure transducers – Tech Note TN-510-1. www.vishaymg.com.

Vishay® 2005b. Errors due to Wheatstone bridge nonlinearity – Tech Note TN-507-1. www.vishaymg.com.

Wang Y.H., and Siu W.K. 2006. Structure characteristics and mechanical properties of kaolinite soils. I. Surface charges and structural characterizations. Can. Geotech. J. 43: 587–600.

Zlatovic S., and Ishihara, K. 1997. Normalized behaviour of very loose non-plastic soils: effects of fabric. Soils and Foundations, Vol. 37, No. 4: 47–56.

ANNEX

CALIBRATIONS

A.1 PRESSURE CONTROL VALVES

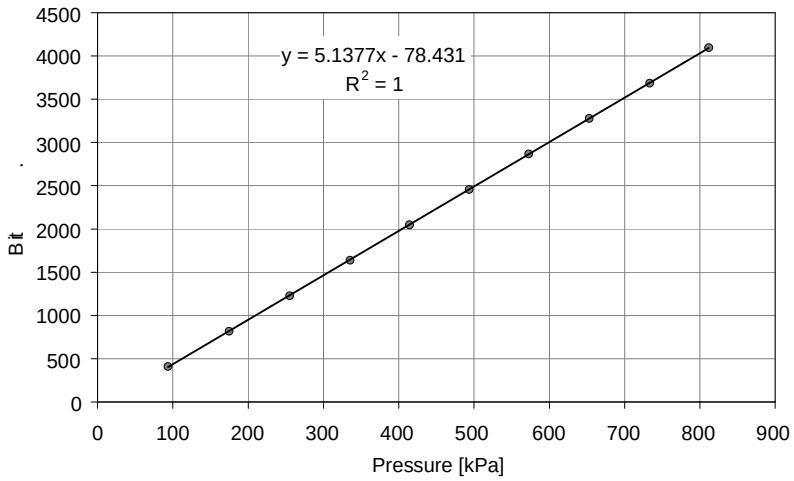

Figure A.1. Pore-water pressure, apparatus R.

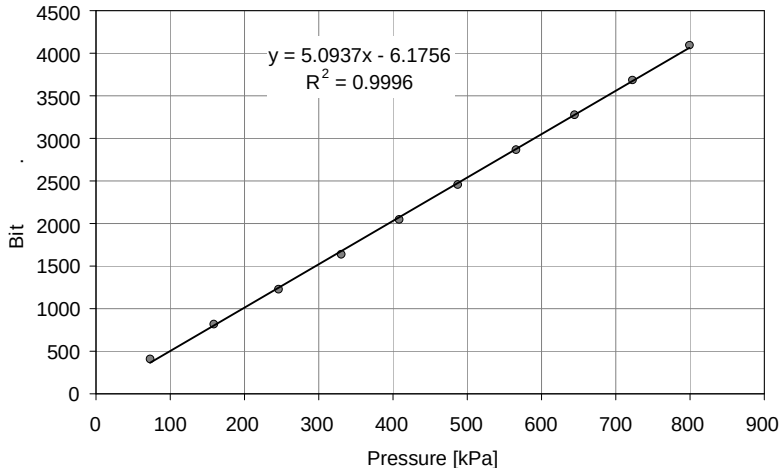

Figure A.2. Pore-water pressure, apparatus L.

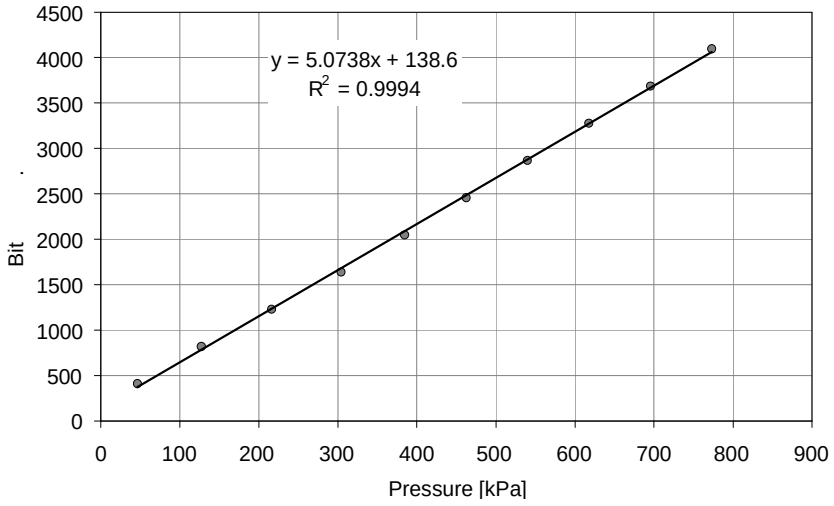

Figure A.3. Pore-air pressure, apparatus R.

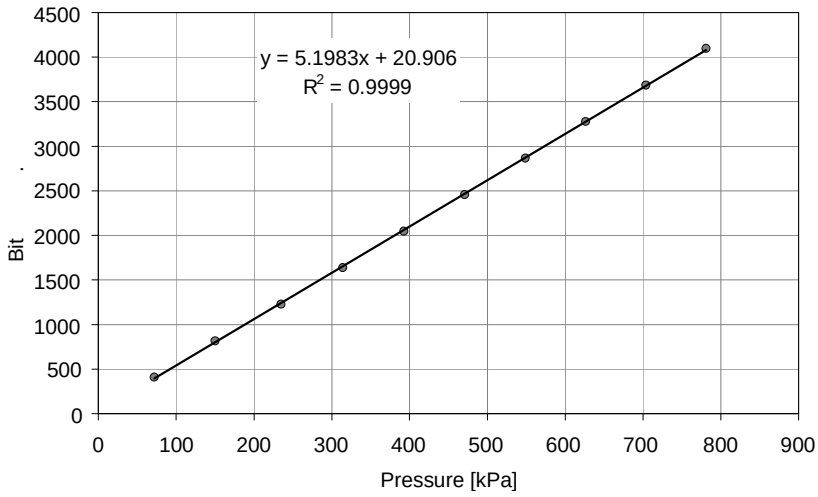

Figure A.4. Pore-air pressure, apparatus L.

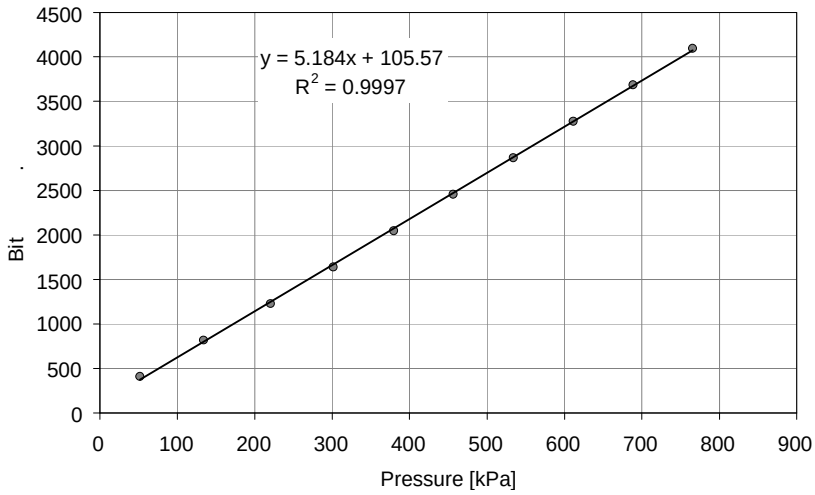

Figure A.5. Cell pressure, apparatus R.

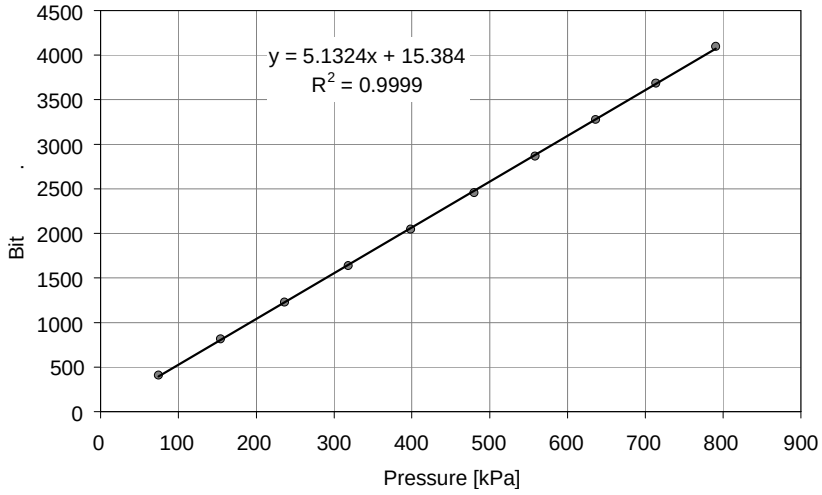

Figure A.6. Cell pressure, apparatus L.

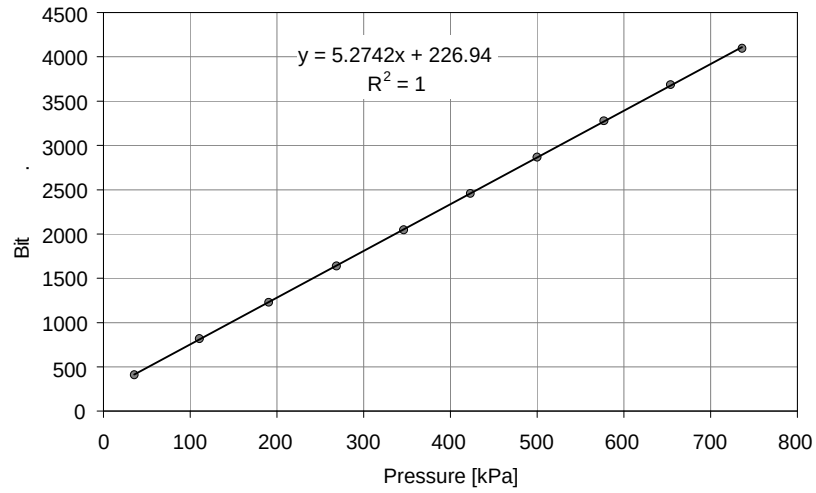

Figure A.7. RAM pressure, apparatus R.

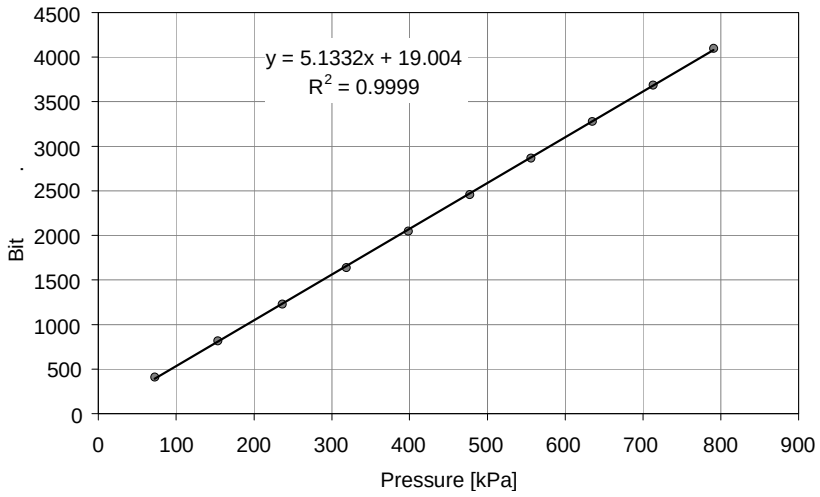

Figure A.8 . RAM pressure, apparatus L.

A.2 PRESSURE TRANSDUCERS

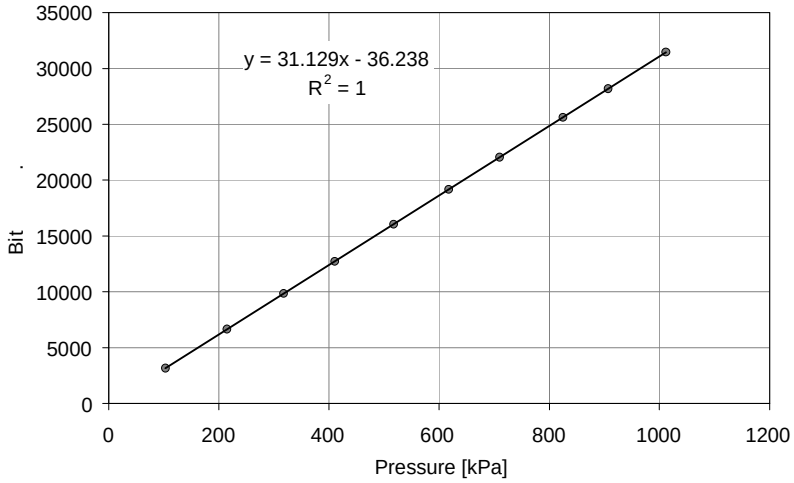

Figure A.9. Pore-water pressure, apparatus R.

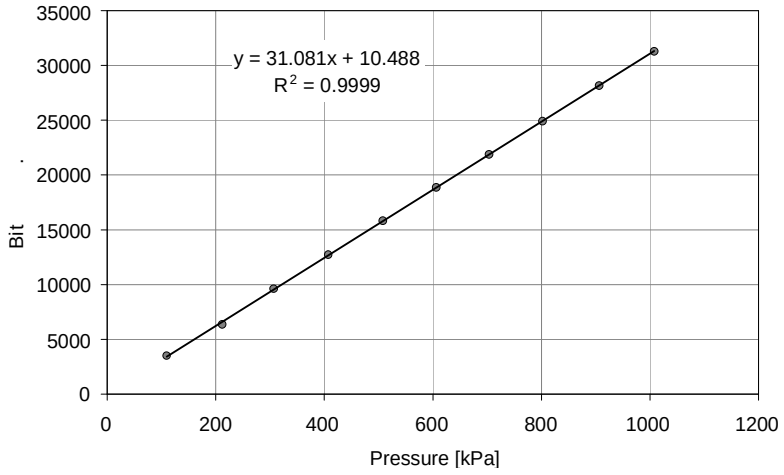

Figure A.10. Pore-water pressure, apparatus L.

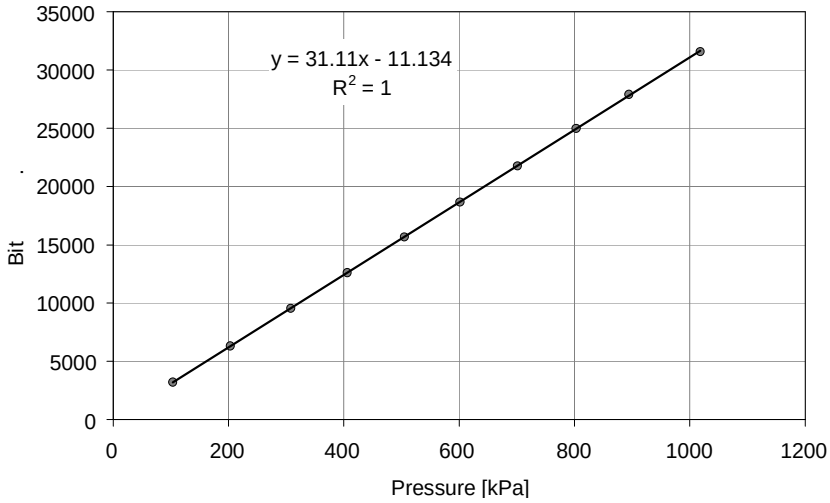

Figure A.11. Pore-air pressure, apparatus R.

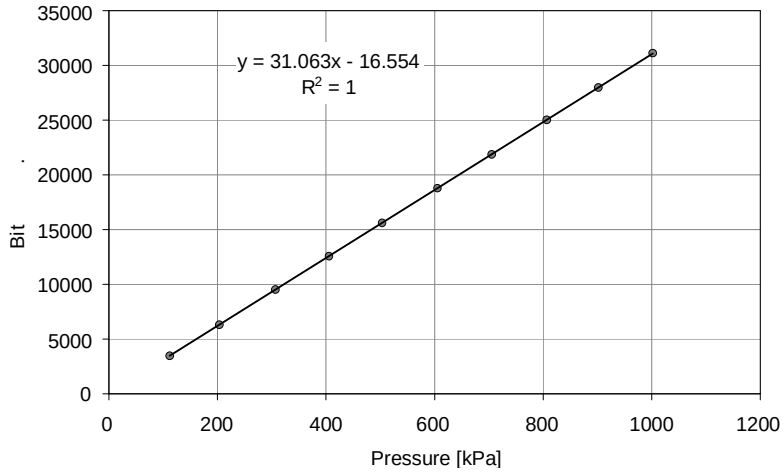

Figure A.12. Pore-air pressure, apparatus L.

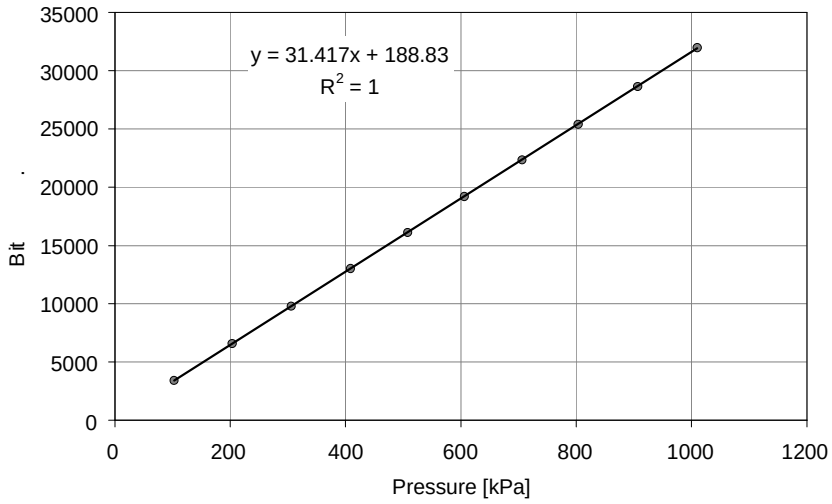

Figure A.13. Cell pressure, apparatus R.

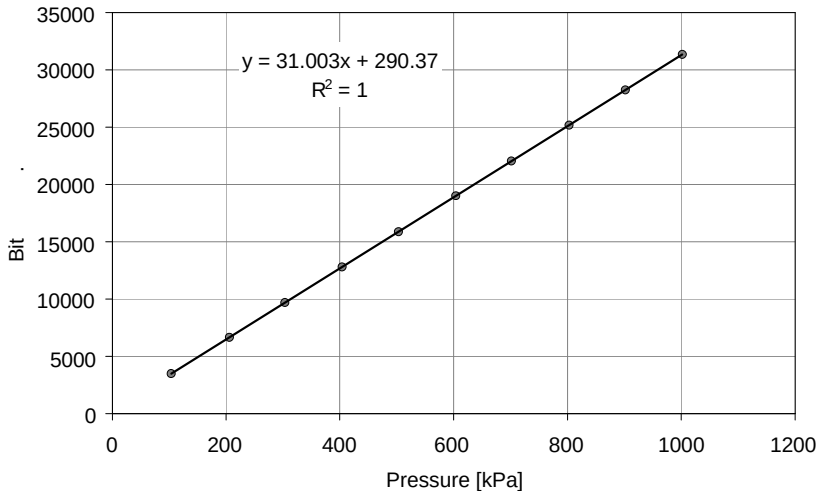

Figure A.14. Cell pressure, apparatus L.

A.3 LOAD CELLS

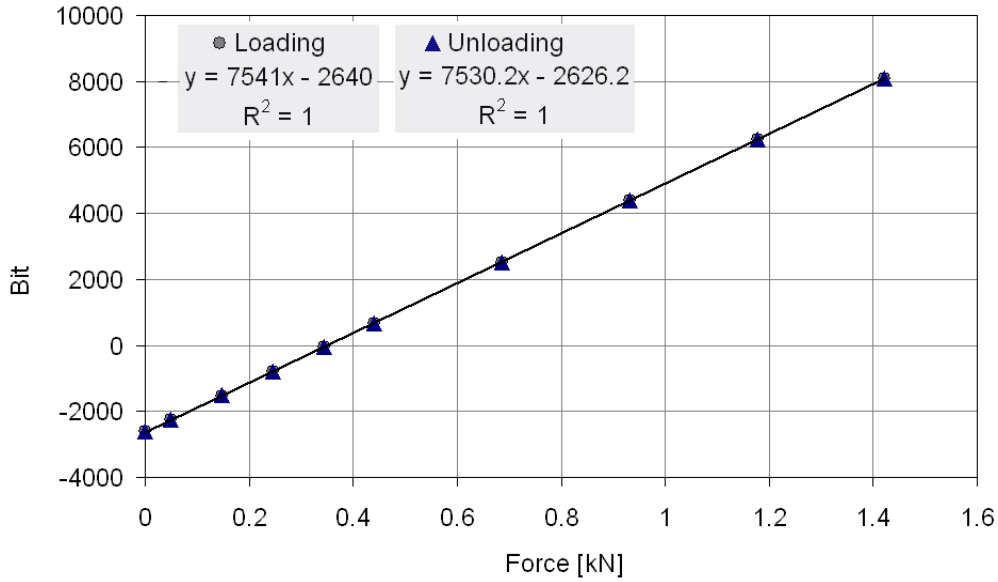

Figure A.15. Calibration of the load cell, apparatus R.

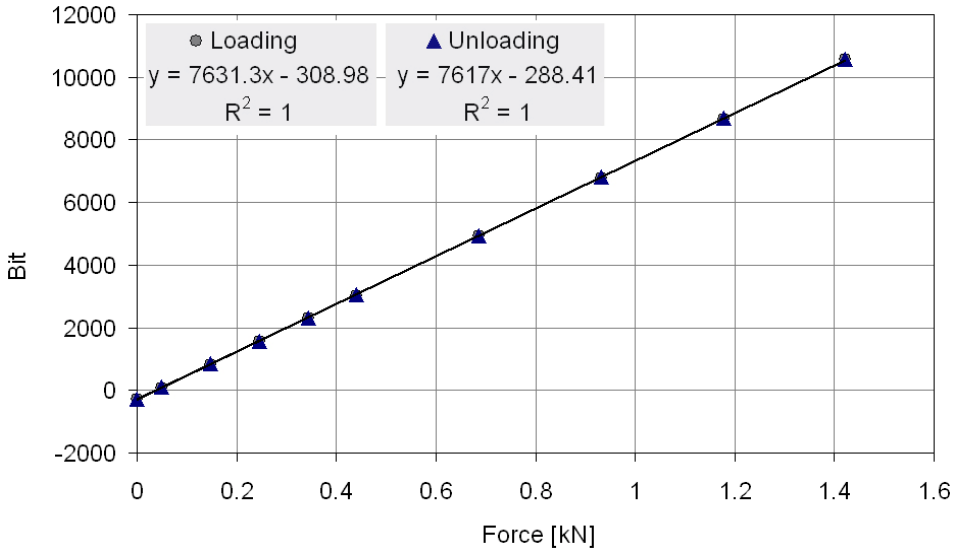

Figure A.16, Calibration of the load cell, apparatus L.

A.4 DISPLACEMENT TRANSDUCERS

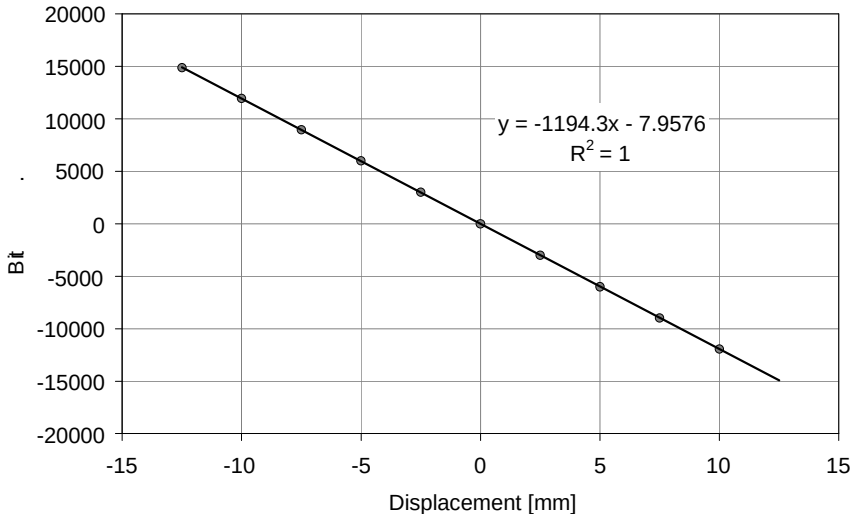

Figure A.17. Calibration of the LVDT, apparatus R.

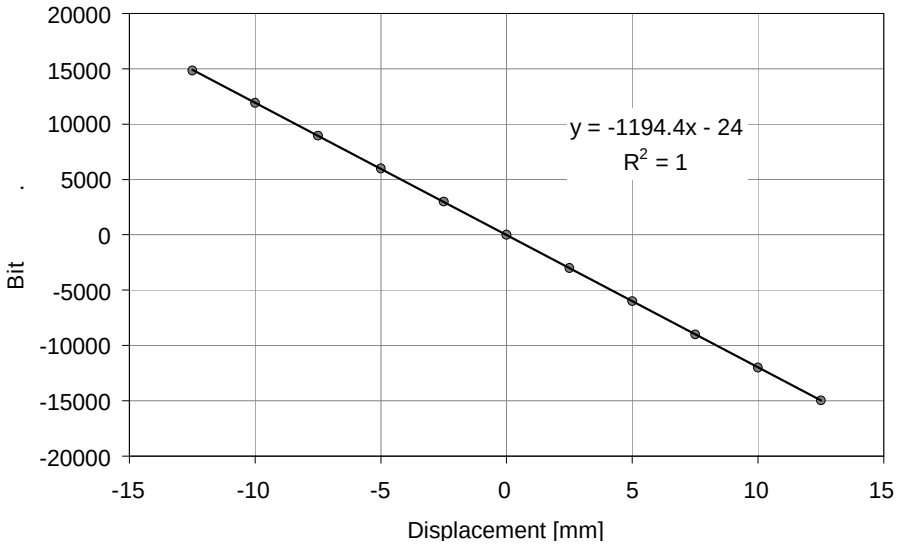

Figure A.18. Calibration of the LVDT, apparatus L.

A.5 INNER CELLS

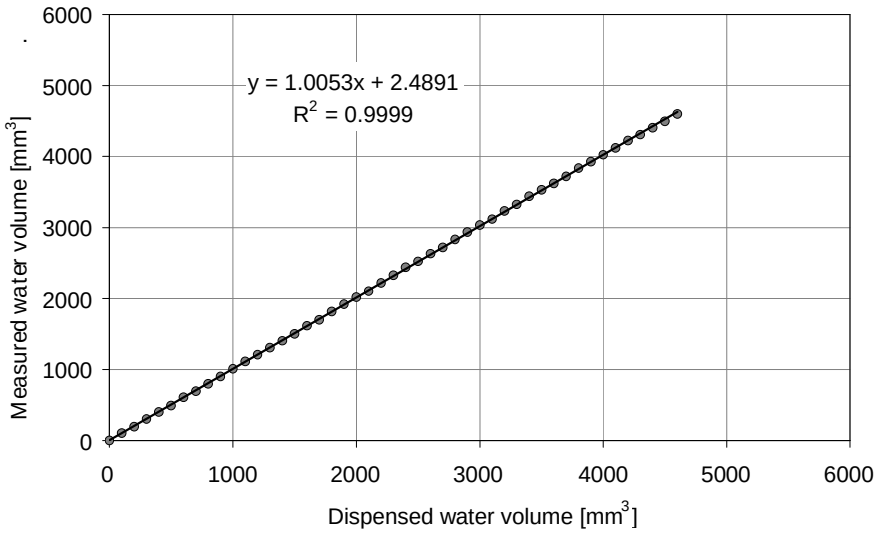

Figure A.19. Calibration of the radial strain measurement system, apparatus R.

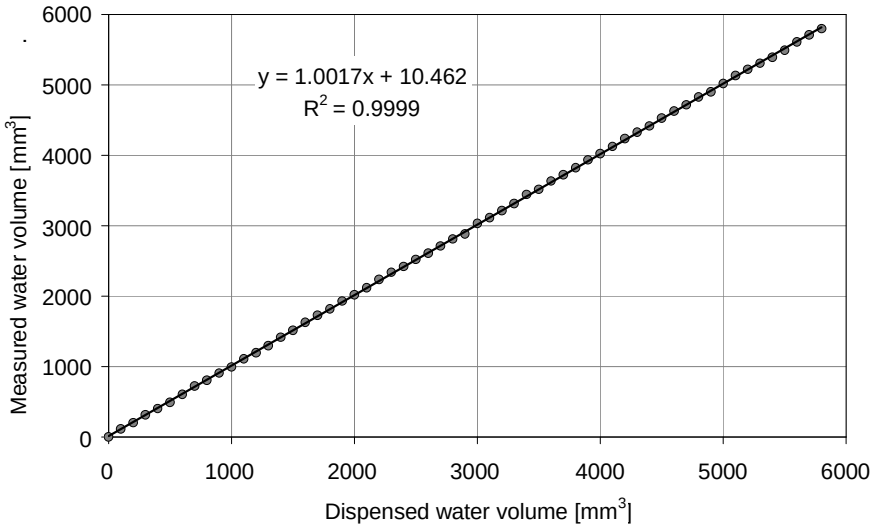

Figure A.20. Calibration of the radial strain measurement system, apparatus L.

A.6 AIRTIGHT WATER-PRESSURE PROBE

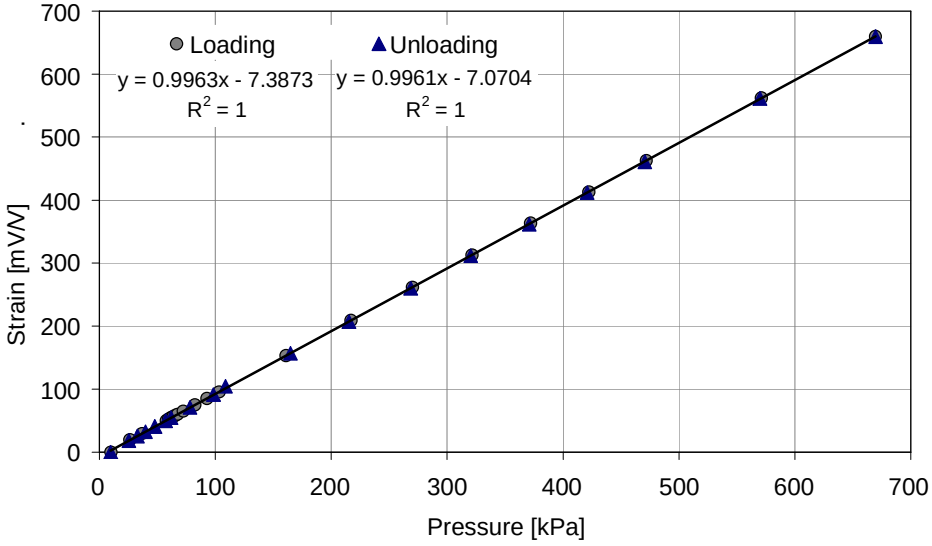

Figure A.21. Calibration of the transducer by using air pressure.

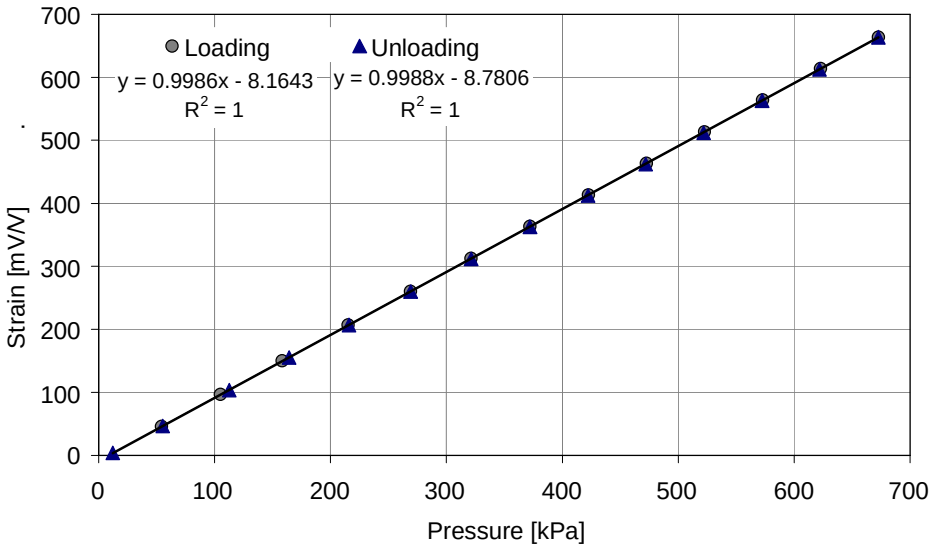

Figure A.22. Calibration of the transducer by using water pressure.